GEOPHYSICAL INVESTIGATIONS OF NEAR-SURFACE STRUCTURE ON THE EARTH AND MARS

Thesis by

Michelle Marie Selvans

In Partial Fulfillment of the Requirements for the Degree of

Doctor of Philosophy

CALIFORNIA INSTITUTE OF TECHNOLOGY

Pasadena, California

2011

(Defended May 9, 2011)

ACKNOWLEDGEMENTS

I have been blessed with a supportive and inspiring community during the course of working on this research. I would not have undertaken these particular studies without the encouragement of my research advisors, Joann Stock and Oded Aharonson. I would like to thank collaborators I have worked with closely who embody the enthusiasm, openness, and curiosity that ideally motivate the pursuit of good (and fun!) science, particularly Rob Clayton, Jeff Plaut, and the late Ali Safaenili.

I want to thank all the people who have helped me find and retain my passion for my work over the last six years, including my academic advisor Mark Simons, fellow graduate students whose interests have aligned with mine, and the students I taught at Pasadena City College.

My life would not have been as rich and fulfilling during my time at Caltech without participating in community activities, and helping make them happen. Every bellydance class and performance with the Dance Troupe, every group hike with the Y, every yoga session, every Tai Chi practice, and every group discussion related to sustainability, ethics, and the life of the mind, has given me the opportunity to share joy in living.

I would like to thank the friends who have supported me through the entire process of being who and where I am in my life today, which includes working on “that huge paper thing you’ve been writing for ages”; thank you especially to Dena for your constant love and understanding!

My family has been a source of encouragement and support in all my endeavors, scientific and otherwise. I am grateful to my parents Susan and Mike Stempel for bringing me up backpacking for family holidays, where I always experienced the deep sense of awe and respect for the natural world that led me to my desire to intimately understand the Earth and other planets. I am grateful to my brother for his example of pursuing one’s passion in work. And I am grateful to my grandparents Marilyn and Frank Rathman for always taking me to the planetarium when I visited as a kid.

I dedicate this work to my Grandpa Frank, who particularly encouraged me in my pursuit of a deep understanding of the physics of the world around me.

Finally, I would like to thank the trails I have hiked countless times in the San Gabriel Mountains, the moon as seen by the naked eye, and my garden, for continually reminding me of the life lessons that cannot be put to words. What a wonderful world!

ABSTRACT

I use remote sensing and active seismic methods to investigate near-surface structure on the Earth and Mars. These studies provide insight into styles of crustal deformation acting on continental margins in regions of extension, as well as paleoclimates that shaped the polar ice caps on Mars. I map the overall structure of the ice-rich Planum Boreum deposit at the north pole of Mars using 178 orbits of Mars Advanced Radar for Subsurface and Ionosphere Sounding data, and find no deflection of the lithosphere beneath the ice load. Bright, laterally extensive subsurface reflectors in the radargrams define the surface underlying Planum Boreum, as well as the interface between the two main units, the stratigraphically older Basal Unit and the stratigraphically younger North Polar Layered Deposits. The volumes of these units, and the overall edifice, are determined to the greatest accuracy possible to date. On Earth, I use a GPS campaign network in the state of Jalisco to investigate tectonic motion and interseismic deformation in the area. The consistent magnitude and direction of station velocities on the Jalisco Block suggest that it is moving rigidly with respect to North America. We constrain extension across the bounding fault zones of the block to values that are slow compared to relative rates of motion at nearby plate boundaries. I study another continental rift zone, in the Ross Sea, Antarctica, with refraction seismic data collected during research cruise NBP0701. I construct velocity models from 71 sonobuoys that detect deep structure in the oceanic crust of the Adare Basin and the crust of the Northern Basin, which lies to the south on the continental shelf. We demonstrate the importance of using multi-channel seismic data to correct for ocean currents and changes in ship navigation, the finite-difference modeling techniques necessary for accurately determining 1D velocity profiles for each sonobuoy, and for tying true velocities to the multi-channel seismic images of subsurface structure. We construct 2D velocity profiles using widely spaced sonobuoys in the Adare Basin, and using overlapping sonobuoys along some lines in both basins, and across the shelf break, to investigate crustal structure in the region. Detection of the Moho at 5.5 km below the seafloor by one sonobuoy suggests relatively thin oceanic crust in the Adare Basin, and flat velocity contours across the margin suggest continuity in crustal structure between the two basins.

TABLE OF CONTENTS

LIST OF FIGURES AND TABLES

Number *Page*

Chapter 1

INTRODUCTION: USING NEAR-SURFACE GEOPHYSICS TO EXPLORE THE PLANETARY NEIGHBORHOOD

Scientists, naturalists, and the generally curious are inspired to better understand the Earth and other planetary bodies. On Earth, every subdiscipline of science undertakes the study of detailed open questions, and of occasional paradigm-changing investigations into the basic processes that act on the Earth. Earth systems are unique within the Solar System in many respects, two of the most obvious being the support of complex life and the sculpting of the surface via plate tectonics. The latter is the paradigm for understanding structure and deformation on and within the bulk of the solid Earth, and only came into use relatively recently in the history of scientific inquiry (i.e., in the 1960s, in its present form).

The surface of the Earth, being for the most part readily accessible, is the most intimately studied portion of the planet. In the early days of science (1700s), structure within the interior of the Earth was only just beginning to be understood, based on rocks revealed in outcrops and mine shafts, and on inference between these observations. In order to investigate near-surface and deep-Earth structure directly, new instruments of observation had to be developed. In the following chapters, I present investigations of the near-surface structure on the Earth and Mars, using multiple observational techniques available today.

Remote-sensing instruments are essential for observing several Earth systems that are global in scale (weather, climate, the magnetic field, gravity, plate motion). Instruments in orbit around the Earth also provide repeat passes over areas of interest, allowing for longitudinal studies. As we (humans) become ever more effective at altering our environment, we will come to depend increasingly on remote monitoring of the Earth systems we depend on and impact. I will

demonstrate uses of ground-penetrating radar and Global Positioning System (GPS) measurements in case studies of near-surface structure on the Earth and Mars.

On Mars, a handful of rovers have provided ground truth for our current understanding of rock types, weather patterns, and soil composition, but the majority of our observations of Mars systems and subsurface structure are obtained from orbit. Two radar instruments capable of imaging subsurface structure are currently orbiting Mars, the longer-wavelength Mars Advanced Radar for Subsurface and Ionosphere Sounding (MARSIS) on Mars Express, and the shorter-wavelength Shallow Radar sounder (SHARAD) on the Mars Reconnaissance Orbiter. MARSIS is uniquely capable of penetrating the full thickness of the polar ice caps on Mars to the rock interface below.

In chapter 2, I use MARSIS data to determine the volume and overall structure of Planum Boreum at the north pole. This study provides the most accurate estimate of Planum Boreum volume to date, one of the largest known reservoirs of water ice on Mars. It also confirms the overall shape of the upper layer of Planum Boreum ice (the North Polar Layer Deposits, or NPLD) as also mapped by SHARAD, and reveals the overall shape of the lower ice unit (the Basal Unit, or BU). In particular, the shape of the upper surface of the BU may hold clues to the processes of deposition and erosion operating in the prior climate regime during which it was emplaced.

Instruments orbiting the Earth can be less expensive to deploy and more easily replaced than those sent to other planetary bodies, and so unique observation capabilities exist. One example is the GPS network of satellites, which allow us to record relative motion between locations on the surface of the Earth to high precision. This technique is useful for studying deformation processes over a wide range of timescales, from an earthquake to long-term plate motion, and can be used to determine the style of deformation taking place at depth.

In chapter 3, I use GPS data to constrain the direction and magnitude of motion within rift zones in the western Mexican state of Jalisco. The Jalisco Block is a portion of continental crust with high elevation relative to its surroundings, located just inland from the small oceanic Rivera Plate,

which is obliquely subducting beneath Jalisco. Geologic evidence suggests that it responds as a coherent block to forces generated through plate motion and the earthquake cycle. I show that over the four years of our study, motion at GPS sites on and around the Jalisco Block is consistent with it moving rigidly relative to neighboring continental crust (the North American plate). I constrain Jalisco Block motion relative to North America to values that are small relative to those at nearby plate boundaries, suggesting that coherent motion of the Jalisco Block is not linked to reorganization of plate boundaries in the region.

I shift gears after these remote-sensing studies, and present a study of near-surface structure based on active seismic data, in a rift zone in the Ross Sea, Antarctica. This technique can reveal structure 10s of kilometers into the crust. The West Antarctic Rift System is the area of extension between East and West Antarctica that formed during the breakup of Gondwanaland, which was the last group of continents to temporarily remain together after the most recent supercontinent of Pangea began to separate. Relative motion between East and West Antarctica is the least well-constrained link in the global plate circuit, which defines the motions of all the plates on Earth back to ~200 Ma.

At one end of the West Antarctic Rift System is a dead mid-ocean spreading ridge, the Adare Trough, lying within the deep-water Adare Basin, at the northwesternmost edge of the Ross Sea. The Adare Trough was a site of localized extension within oceanic crust, and terminates close to the continental shelf. In Chapter 4, I explain the processing techniques we developed to analyze sonobuoy (refraction seismic) data collected during a research cruise onboard the *Nathaniel B. Palmer* in 2007. This dataset is unique in that many sonobuoys were deployed in relatively close proximity to one another, with half of them actually overlapping, allowing us to construct 2D velocity models for the deeper crust in Adare Basin and neighboring Northern Basin (on the continental shelf).

In Chapter 5, I show the 2D velocity models obtained from the sonobuoy data and interpret the subsurface structure in the context of regional tectonics. Our results, as well as other lines of

evidence, suggest continuity of crustal structure between the Adare and Northern Basins, indicating that extension within the Adare Trough may have also been localized within the continental crust to its south, forming the Northern Basin as a result. Observations of localized extension in our study, and in similar tectonic settings around the world, suggest that despite their longevity in the plate tectonic system, continents are susceptible to rifting along their margins.

By looking under the skin of the Earth and Mars, we can better understand the processes of deposition, erosion, and deformation that form the structure we observe. Whether investigating an ice reservoir to a few kilometers' depth or rocky crust to several kilometers' depth, details of the past climate or plate tectonic system, respectively, are revealed. Understanding the past gives us clues as to the future of these systems, and comparing tectonics and climate between two worlds gives us further insight into the realm of possibility for the behavior of global-scale terrestrial systems.

C h a p t e r 2

INTERNAL STRUCTURE OF PLANUM BOREUM, FROM MARS ADVANCED RADAR FOR SUBSURFACE AND IONOSPHERIC SOUNDING DATA[1]

An investigation of the internal structure of the ice-rich Planum Boreum (PB) deposit at the north pole of Mars is presented, using 178 orbits of Mars Advanced Radar for Subsurface and Ionospheric Sounding data. For each radargram, bright, laterally extensive surface and subsurface reflectors are identified, and the time delay between them is converted to unit thicknesses using a real dielectric constant of 3. Results include maps of unit thickness, for PB and its two constituent units, the stratigraphically older Basal Unit (BU) and the stratigraphically younger North Polar Layered Deposits (NPLD). Maps of the individual units' surface elevation are also provided. Estimates of water ice volume in each unit are $(1.3\pm0.2) \times 10^6$ km^3 in PB, $(7.8\pm1.2) \times 10^5$ km^3 in the NPLD, and $(4.5\pm1.0) \times 10^5$ km^3 in the BU. No lithospheric deflection is apparent under PB, in agreement with previous findings for only the Gemina Lingula lobe, which suggests that a thick elastic lithosphere has existed at the north pole of Mars since before the emplacement of the BU. The extent of BU material in the Olympia Planum lobe of PB is directly detected, providing a more accurate map of BU extent than previously available from imagery and topography. A problematic area for mapping the BU extent and thickness is in the distal portion of the 290 – 300° E region, where MARSIS data show no subsurface reflectors, even though the BU is inferred to be present from other lines of evidence.

---

[1] This chapter is published in its entirety under the same title by authors M. M. Selvans, J. J. Plaut, O. Aharsonson, and A. Safaeinili (2010), in *Journal of Geophysical Research* 115, E09003, doi:10.1029/2009JE003537.

[2] This chapter is published in its entirety under the same title by authors M. M. Selvans, J. M. Stock, C. DeMets, O. Sanchez, and B. Marquez-Azua (2010), in *Pure and Applied Geophysics*, doi: 10.1007/s00024-010-0201-2.

Introduction

Icy deposits on Mars are repositories of information potentially useful for understanding the history of the planet's climate. The north and south polar deposits are the largest reservoirs of water known on Mars, and likely contain a detailed record of current and past climate [*Thomas et al.*, 1992]. Detailed analysis of the internal structure of icy deposits is now possible with radar data, providing a more complete picture of the history of formation of polar deposits.

Several units make up Planum Boreum, the domed edifice composed mostly of water ice that rises above the northern plains [e.g., *Cutts*, 1973], with two units in particular making up the bulk of the volume. This study focuses on the two thickest units at the north pole, the stratigraphically older Basal Unit (BU) and the stratigraphically younger North Polar Layered Deposits (NPLD), since their large volumes likely contain the greatest wealth of information about regional and global climate history. The NPLD are superimposed on the BU (which is subdivided into the Rupes Tenuis unit and Planum Boreum cavi unit by Tanaka et al. [2008]) for most of the extent of Planum Boreum [*Byrne and Murray*, 2002; *Fishbaugh and Head*, 2005], making the relationship of younger NPLD and older BU clear, but each exists independent of the other for some portion of the domed deposits as well.

The Mars Advanced Radar for Subsurface and Ionospheric Sounding (MARSIS) dataset provides a unique opportunity to characterize and fully map the BU for the first time. This is because MARSIS is the first instrument capable of directly detecting the interface between Planum Boreum and the underlying material of the Vastitas Borealis Formation (VBF, called the Vastitas Borealis interior unit in Tanaka et al. [2008]) [*Picardi et al.*, 2005].

This study refines the volume estimate for Planum Boreum, independently determines volumes of the separate BU and NPLD units, determines the topography at the interface between the BU and

VBF, directly measures the lateral extent of the BU, and provides an independent confirmation of results for the volume and extent of the NPLD obtained from the Shallow Radar (SHARAD) dataset [*Putzig et al.*, 2009].

Background: Composition and climate history of polar ice on Mars

The polar deposits of Mars are composed primarily of water ice, with a few to perhaps 15% dust by volume in the South Polar Layered Deposits (SPLD) [*Plaut et al.*, 2007a; *Zuber et al.*, 2007], no more than 2% impurities in the NPLD [*Picardi et al.*, 2005], and a relatively dark and "sand-rich" BU underlying the NPLD [*Byrne and Murray*, 2002; *Fishbaugh and Head*, 2005]. Based on recent imagery, Herkenhoff et al. [2007] further show that the BU is largely made up of bright layers that are likely volatile-rich, with interleaved layers of concentrated impurities.

It was previously suggested that the dome-shaped Planum Boreum continues under Olympia Planum (see Figure 1), based on the gentle slope of the surface dunefield away from the main deposits in the 180°-longitude direction [*Zuber et al.*, 1998]. The NPLD and BU are distinct in imagery, the NPLD being brighter than the BU, layered more finely, and smoother where layers are exposed at the surface [*Byrne and Murray*, 2002; *Herkenhoff et al.*, 2007]. The BU is the better candidate for the ice deposit beneath Olympia Planum, based on the extent of both the BU and NPLD in surface imagery [*Byrne and Murray*, 2002; *Fishbaugh and Head*, 2005].

In the south polar region, MARSIS detects laterally continuous interfaces within the SPLD, as well as the interface at the base of the ice, at depths of up to 3.7 km [*Plaut et al.*, 2007a]. By mapping out the basal surface beneath the ice using 60 MARSIS orbits, Plaut et al. [2007a] show there is no significant deflection of the lithosphere due to loading of the ice, indicating a thick elastic lithosphere at the south pole of Mars. MARSIS additionally reveals a likely ice-rich layer up to 1 km thick surrounding and possibly extending beneath the SPLD, in areas correlated with the Dorsa

Argentea Formation [*Plaut et al.*, 2007b]. The volume of water ice in the SPLD is most accurately estimated by mapping the subsurface SPLD structure, particularly the basal interface; the SPLD contain (1.6±0.2) × 10^6 km^3 of nearly pure water ice, the largest known reservoir of volatiles on Mars [*Plaut et al.*, 2007a]. Planum Boreum is the next largest reservoir, with a volume of (1.2 – 1.7)×10^6 km^3, as previously estimated from surface elevation and various assumptions about the basement topography [*Zuber et al.*, 1998]. A fraction of this estimate, 2.7×10^5 km^3, was attributed to the BU [*Byrne and Murray*, 2002].

While the appearance of the NPLD and SPLD is similar, with respect to layering and albedo, their surfaces are of different ages. Based on crater statistics, the surface age of the SPLD is 10 – 100 Ma [*Herkenhoff and Plaut*, 2000; *Koutnik et al.*, 2002], while for the NPLD it is ~100 ka [*Banks et al.*, 2009; *Herkenhoff and Plaut*, 2000]. A small number of craters on the surface of the BU with ≥5 km diameter indicate that the BU surface age may be ~100 Ma to ~2 Ga [*Pathare et al.*, 2005; *Tanaka et al.*, 2008]. Based on recent imagery, Tanaka et al. [2008] distinguish between an older (1 – 3 Ga) portion of the BU (their Rupes Tenuis unit, underlying much of the NPLD) and a younger (<1 Ga) portion of the BU (their Planum Boreum cavi unit, which likely makes up the bulk of Olympia Planum). The range of ages for the SPLD, NPLD, and BU indicates different histories of ice deposition and erosion at the two poles of Mars.

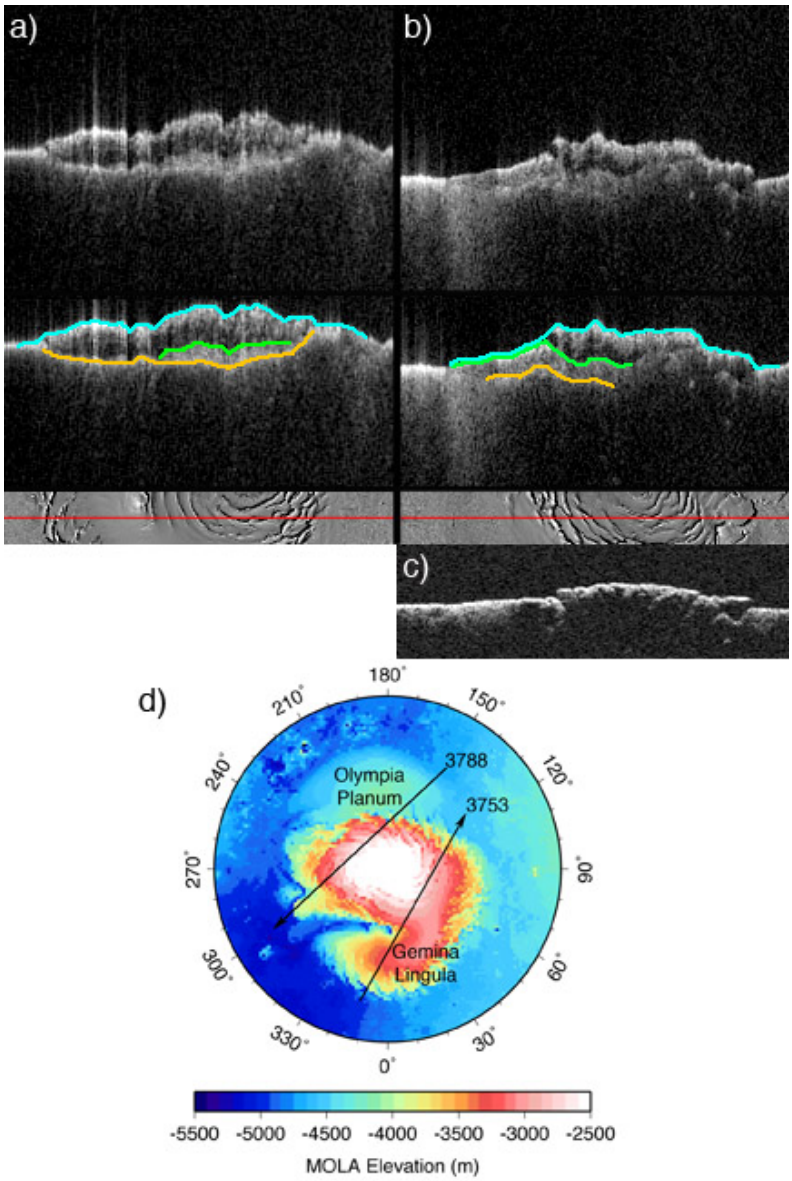

Figure 2.1. (a) MARSIS radargram of orbit 3753, crossing Gemina Lingula and the main lobe of Planum Boreum, as indicated on the shaded-relief Mars Orbiter Laser Altimeter (MOLA) topography. Reflectors selected at the surface, the top of the Basal Unit (BU), and the basal interface are shown in cyan, green, and yellow. (b) Radargram of orbit 3788, crossing Olympia Planum and the portion of Planum Boreum where MARSIS rarely detects the basal interface (270° – 300° E). (c) Surface clutter simulation for orbit 3788, based on MOLA topography. (d) Orbits 3753 and 3788 are typical of the portions of Planum Boreum they cross, with ground tracks corresponding to the two radargrams indicated by the black arrows (arrowheads show the direction of data collection); MOLA data is in polar stereographic projection and cover 75° N – 90° N.

With the sparse craters available to date the BU, superposition relationships are useful for understanding its emplacement and persistence. The Vastitas Borealis Formation (VBF) makes up most of the flat, low-lying northern plains and lies just underneath the ice deposits, putting a maximum age limit of ~3 Ga on the BU [*Tanaka*, 2005; *Tanaka et al.*, 2008]. The NPLD are generally thought to have persisted only as long as the average summer insolation in the northern hemisphere has been similar to that of today, which is dependent on the obliquity of Mars [*Laskar et al.*, 2002]; prior to 4.2 Ma, the high obliquity could have caused any exposed north polar ice to be redistributed to lower latitudes [*Levrard et al.*, 2007]. While this is a possible minimum age limit for the BU, which is largely covered by the NPLD, the question remains as to why the BU would persist during times of high obliquity. High-Resolution Imaging Science Experiment (HiRISE) images implicate mass wasting as the main form of BU erosion, implying a lag protecting the BU from insolation-based erosion until blocks detach and expose more surface area to the process of ablation [*Herkenhoff et al.*, 2007].

Since the top surface of the BU is mostly hidden by the NPLD and the Olympia Planum dunefield, mapping its extent and thickness with imagery is challenging. Soderblom et al. [1973] first identified the boundaries of Planum Boreum using Mariner 9 images, which well described the limits of the NPLD but not the BU; Mars Orbiter Laser Altimeter (MOLA) data suggested that the gently sloping Olympia Planum dunefield covers additional ice-rich material [*Zuber et al.*, 1998]. The lateral extent and thickness of the BU was estimated using MOLA data and identification of BU material in Mars Orbiter Camera (MOC) and more recent imagery [*Byrne and Murray*, 2002; *Fishbaugh and Head*, 2005; *Tanaka*, 2005; *Tanaka et al.*, 2008]. With the arrival of MARSIS and SHARAD instruments at Mars [*Seu et al.*, 2007], it is now possible to directly detect the BU-NPLD boundary [*Putzig et al.*, 2009] and, in the case of MARSIS, the extent of the BU under Olympia Planum, and its overall thickness.

Layering within the NPLD and BU is attributed to differential inclusion of contaminants in the ice. In the case of the NPLD, alternating bright and dark layers may be dependent on the amount of

dust [*Cutts*, 1973]; HiRISE images show that apparent brightness is more directly related to topography, texture, and surficial frost distribution [*Herkenhoff et al.*, 2007], although these attributes are likely influenced by the relative content of impurities in the layers of ice. With SHARAD, larger-scale layering is observed in the NPLD, perhaps corresponding to packets of visible layers [*Plaut et al.*, 2009], as is the case in at least one lobe of the SPLD [*Milkovich et al.*, 2009]. Layers in the NPLD are observed to intersect the surface at steep scarps in both imagery [*Malin and Edgett*, 2001] and subsurface radar data [*Putzig et al.*, 2009], suggesting a correspondence in interface detection with these two methods. Individual layers, particularly within the NPLD, may be the result of changing insolation due to orbital forcing [e.g., *Phillips et al.*, 2008; *Putzig et al.*, 2009; *Squyres*, 1979].

The BU is often described as sandy with varying amounts of volatiles, rather than volatile-rich with a few percent impurities by volume (like the NPLD) [*Byrne and Murray*, 2002; *Herkenhoff et al.*, 2007]. The association of the BU with sand is due to proximity of exposed portions of the BU with the apparent source areas of dark, circumpolar sand dunes [*Byrne and Murray*, 2002]. The BU contains many erosion-resistant layers with debris piles (due to mass wasting) at their base [*Fishbaugh and Head*, 2005; *Herkenhoff et al.*, 2007]. The very different appearance of the BU from the NPLD (in color, layering style and thickness, texture, and association with dunes), leads to the suggestion that the BU was formed under different climatic conditions than those present during NPLD formation [*Byrne and Murray*, 2002; *Fishbaugh and Head*, 2005].

Methods: Using radar data to determine gross structure of the ice cap

MARSIS is a nadir-looking, low-frequency, synthetic aperature radar instrument on the Mars Express orbiter [*Picardi et al.*, 2004]. For subsurface sounding of dielectric discontinuities, MARSIS operates in 1 MHz bands centered at 1.8, 3, 4, and 5 MHz; vertical resolution (as

determined by the bandwidth) is 150 m in free space (~100 m in water ice), and spatial resolution is 5 – 10 km along-track and 15 – 30 km in the cross-track direction.

Two major MARSIS campaigns have targeted Planum Boreum to date; 178 orbits provide radargrams with bright, continuous subsurface reflectors. MARSIS regularly penetrates the BU and detects the interface between ice and underlying material, and so complements the higher-resolution SHARAD data set, which due to its higher frequency is typically limited to probing the interior and lower boundary of the NPLD [*Phillips et al.*, 2008; *Putzig et al.*, 2009].

Initial data processing is performed onboard, combining ~100 time-domain echoes into one frame (~1 s) of frequency-domain data; hundreds of frames are displayed sequentially in the time domain to transect Planum Boreum in radargram format [*Picardi et al.*, 2005]. Corrections for ionospheric distortion are applied to radargrams before interpretation [*Safaeinili et al.*, 2003].

Subsurface reflectors in MARSIS radargrams were picked manually, from the one of two simultaneously operating bands with sharper subsurface reflections, selecting the time-delay center of vertically well-constrained and laterally continuous reflectors, every 5 – 10 frames along the reflector (Figure 1). The criterion for selection of a reflector is that it is both continuous for at least 10 frames (~50 km along-track) and separated from other reflectors in the frame by at least 3 pixels (~300 m vertically). Simulations of clutter from off-nadir surface returns (see Figure 1c) are used to avoid interpreting surface clutter as a subsurface reflector.

The NPLD typically appear in MARSIS radargrams as a radar-dark zone following the brighter near-surface returns, whereas the BU appears instead as a diffuse and brighter zone (see Figure 1). Their distinct appearances in the MARSIS data allow for easy identification of the location of each of the two units in the subsurface. Where the NPLD lie on top of the BU, the intermediate interface is most often identified by the transition from dark to bright radar return, rather than by a bright reflection along the interface.

Layer thicknesses are calculated for each frame by subtracting the radargram pixel position at the top of the layer (p_1) from that at the bottom (p_2), and converting to distance using a real dielectric constant (ε_r) of 3.0 and a vertical resolution in a vacuum of 102 m/pixel (i.e. $c \times dt$, where c is the speed of light and dt is 0.68 μs/pixel): $d = [(^1/_2)\,(p_2 - p_1)\,(102)]/\sqrt{\varepsilon_r}$. The full thickness of Planum Boreum and thicknesses for the BU and NPLD are calculated separately. Other reasonable values for the real dielectric constant, such as 3.15 used in SHARAD analysis [e.g., *Putzig et al.*, 2009], produce only a minor difference in measured thickness, smaller than the vertical resolution of the MARSIS data.

Planum Boreum thickness values are subtracted from MOLA surface elevation to obtain elevation values at the basal interface. Elevation values at the top of the BU are compiled from both surface elevation where the BU is at the surface (e.g., Olympia Planum), and NPLD thickness values subtracted from surface elevation where the NPLD lies on top of the BU.

After determining thickness values and elevation values in each frame with useful data, that data is binned to 15×15 km cells for each layer thickness or interface elevation (see Figure 2a for Planum Boreum values). A cubic spline interpolation fills in cells that contain no useful MARSIS data (see Figure 2b). The largest areas filled by interpolated values are the region poleward of 87° N (~300 km diameter), where there are no data due to the Mars Express orbital inclination of 86.3°, and the region between 270° E and 300° E (of similar area to the circle at the north pole), where no basal reflections are observed in MARSIS data. In the latter area, the distal boundary of Planum Boreum (see Figure 2a) is determined by the MOLA-based estimated thickness (Figure 2d), whereas elsewhere the locations of zero-thickness cells that define the boundary are determined by the maximum extent from the north pole of basal reflections in MARSIS data, within 5° on either side of a given longitude. Other than in the two sizable areas mentioned above, MARSIS data provide nearly complete coverage of Planum Boreum.

Results: Planum Boreum structure and volume

Maps are provided in Figures 3 and 4 of the Planum Boreum deposit thicknesses (including the BU and NPLD separately), and of the elevation of internal interfaces within Planum Boreum. MARSIS uniquely reveals the extent and shape of the older BU deposit, since it is the only instrument to directly detect the interface between the ice-rich BU and the underlying material of the VBF. Additionally, volume estimates are calculated for Planum Boreum as a whole, as well as for the BU and NPLD separately.

Since MARSIS operates at a much lower spatial resolution than the available altimetry data, relatively narrow features such as troughs usually are not evident in the radargrams (e.g., Figures 1a and 1b). Two radargrams illustrate the typical appearance of useful MARSIS data (Figure 1), where they are of sufficient quality to resolve reflectors to within 1-2 pixels. The surface reflection is most often the brightest radar return within a single orbit, the next brightest typically being the basal reflector. In contrast, the interface between the NPLD and BU is not characterized by a bright lineation, but instead by the contrast in character of the radar return, from radar-dark in the lower NPLD to the diffuse return of the BU (the same change is observed at this interface in SHARAD data, e.g.. Putzig et al. [2009]). Olympia Planum has a unique “smeared” appearance in radargrams (Figure 1b), with the signal gradually fading for 10s of pixels after the surface reflector is detected, likely the result of either off-nadir scattering from the surface dunefield or internal scattering within the dunes.

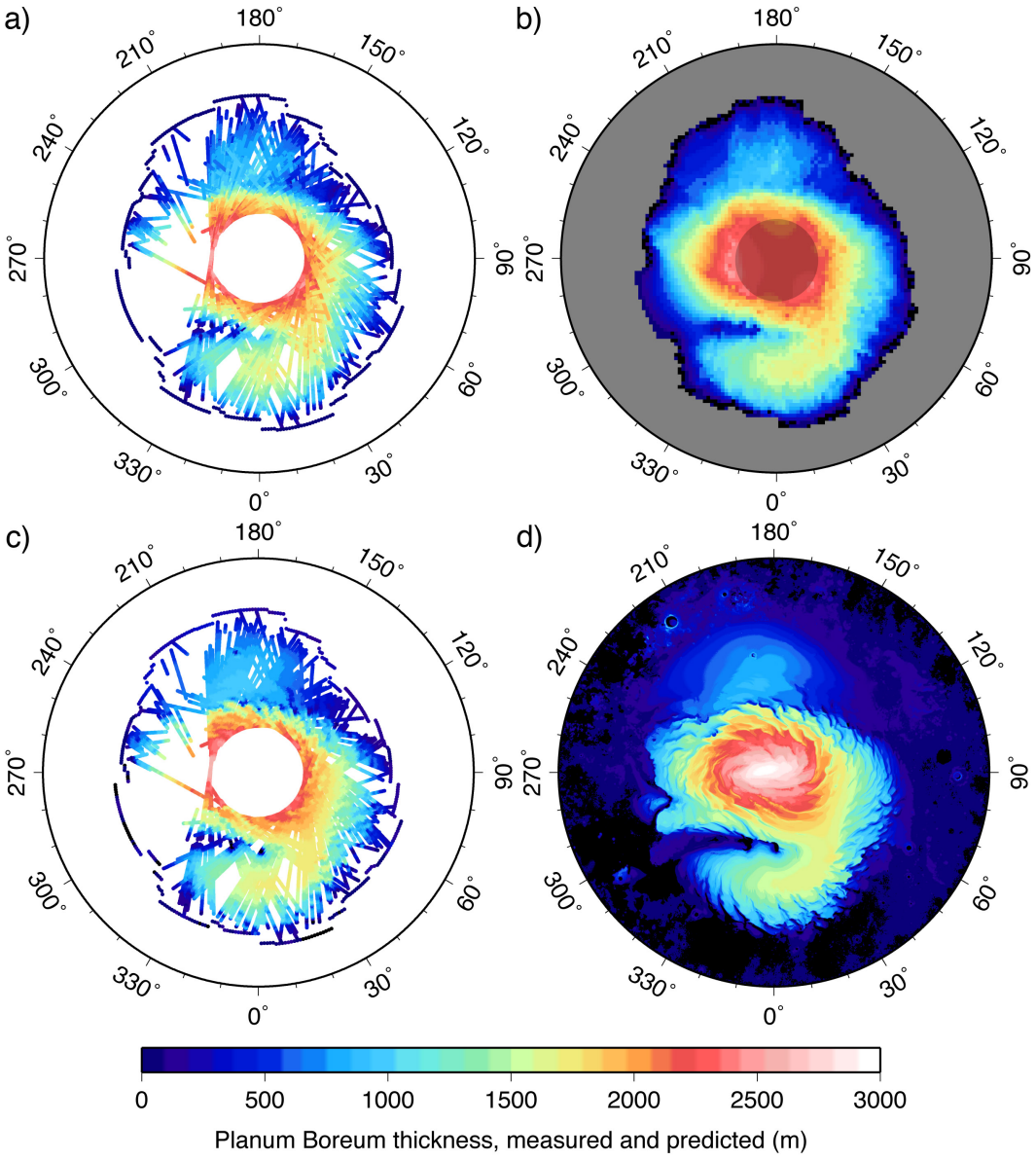

Figure 2.2. A comparison of measured and estimated (from topography) thickness maps of Planum Boreum. (a) Individual thickness measurements from MARSIS data are used to (b) interpolated thickness within the outline of Planum Boreum (gray circle indicates lack of MARSIS coverage). (c) Estimated thickness, determined by subtracting an interpolated regional slope of the underlying interface (based on MOLA data within 75° – 70° N) from surface elevation (MOLA), is displayed at the locations with measured thickness values, and (d) for the entire Planum Boreum region. Measured and estimated thicknesses for Planum Boreum generally agree within the ±200 m vertical measurement error; differences of <500 m occur in locations with >1000 m of relief in surface elevation. Maps are in polar stereographic projection for 75° N – 90° N.

The bulk structure of Planum Boreum is apparent when all 178 useful MARSIS orbits that cross the region are interpreted together (Figure 2). For comparison, an estimate of the thickness of Planum Boreum is determined by subtracting an assumed basal topography from surface elevation (MOLA); basal topography is interpolated from an annulus of MOLA data exterior to Planum Boreum (75° – 70° N). Measured and estimated Planum Boreum thicknesses generally agree within the ±200 m vertical measurement error; the clear exceptions occur at locations with >1000 m of relief in surface topography (see Figure 1d), where discrepancies of up to 500 m in measured and estimated thicknesses are common (compare Figures 2b and 2d).

The extension of the BU under the dunefield of Olympia Planum is confirmed (see Figure 1b), as predicted on the basis of topography and imagery [*Byrne and Murray*, 2002; *Fishbaugh and Head*, 2005]. The lack of deflection under all of Planum Boreum is also confirmed, based on a comparison of thickness measurements for the deposits and estimated thickness for the case of no deflection (Figure 2). This was previously observed only for the Gemina Lingula lobe of the deposits, using SHARAD data [*Phillips et al.*, 2008; *Putzig et al.*, 2009].

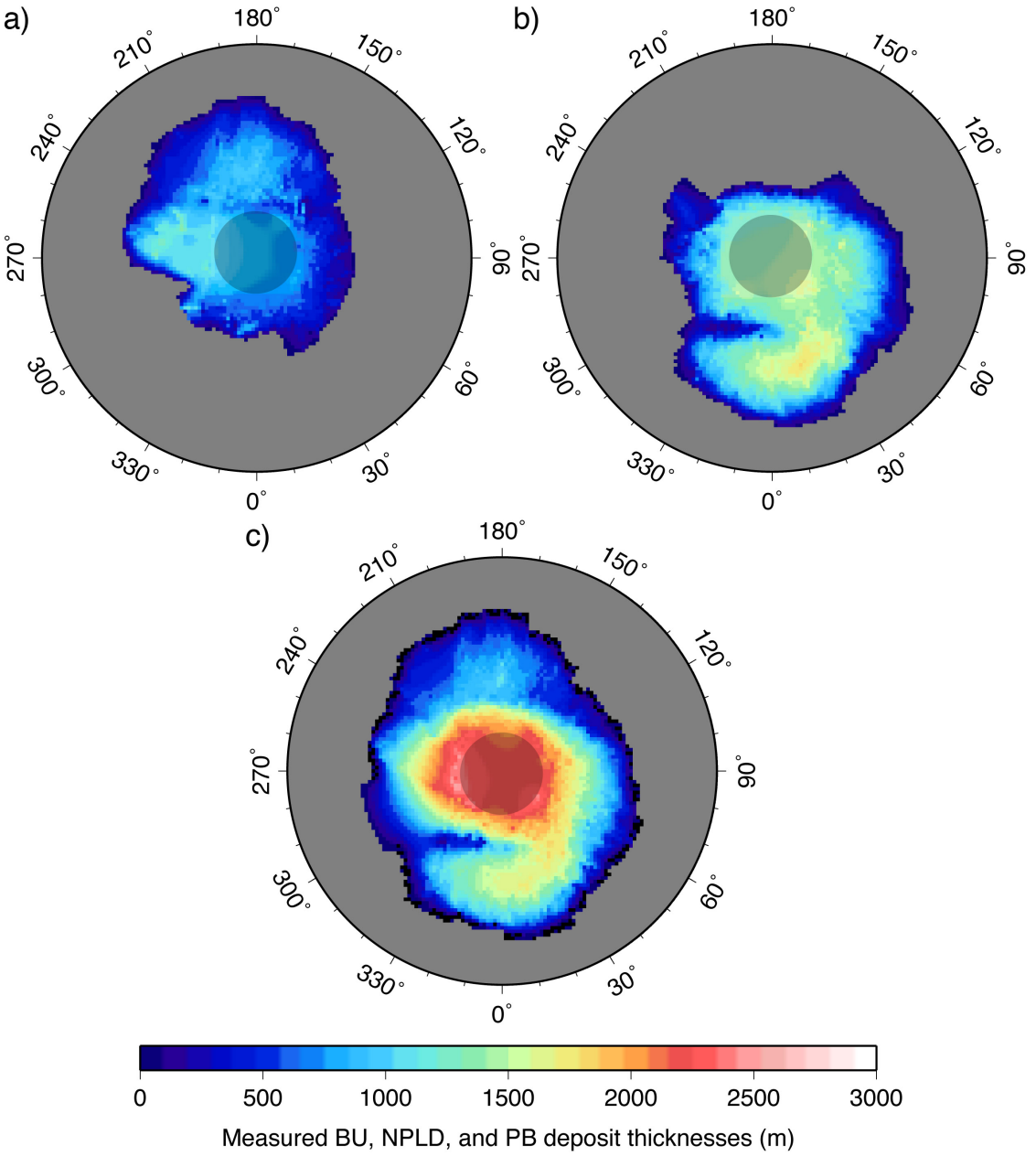

Figure 2.3. Interpolated thicknesses of (a) the Basal Unit (BU), (b) the North Polar Layered Deposits (NPLD), and (c) the deposits as a whole reveal the overall structure of Planum Boreum (PB). The BU and NPLD are both offset from the north pole, in different directions. Gray circles indicate lack of MARSIS coverage. Maps are in polar stereographic projection for 75° N – 90° N.

The BU and NPLD are both offset from the north pole, with the thickest part of the BU in the 260° E direction and the thickest part of the NPLD in the 30° E direction (Figure 3), complementing each other such that Planum Boreum has an overall domed shape centered on the north pole [see also *Putzig et al.*, 2009]. The Olympia Planum and Gemina Lingula regions have just one of the two units present, the BU and NPLD respectively. The position of the BU may have determined the subsequent placement of the NPLD, but the depositional and/or erosional environment that originally caused the BU to be offset from the north pole is unknown. Maximum measured thicknesses are 1100 m for the BU, 1800 m for the NPLD (in Gemina Lingula), and ~2600 m for the full Planum Boreum deposit (at 87° N); our measured maximum full thickness agrees with the estimated ~2700 m at 87° N (see Figure 2).

Since this study directly detects the BU, it provides the most accurate delineation of its extent to date (see Figure 3a). While portions of the BU outline have been delineated based on imagery [*Fishbaugh and Head*, 2005] and SHARAD data [*Putzig et al.*, 2009], this study particularly improves the understanding of the BU's extent in Olympia Planum. The one portion of the BU boundary that is still best characterized by imagery and SHARAD is the peninsula-shaped plateau within 290° – 300° E, with up to 1200 m of relief at its edges, since no basal reflections are observed in this area. In this area, the distal boundary of Planum Boreum is approximated from topography-based estimated thickness (e.g., Figure 2d), but otherwise the BU outline is explicitly detected in MARSIS data (see Figures 3a and 4b).

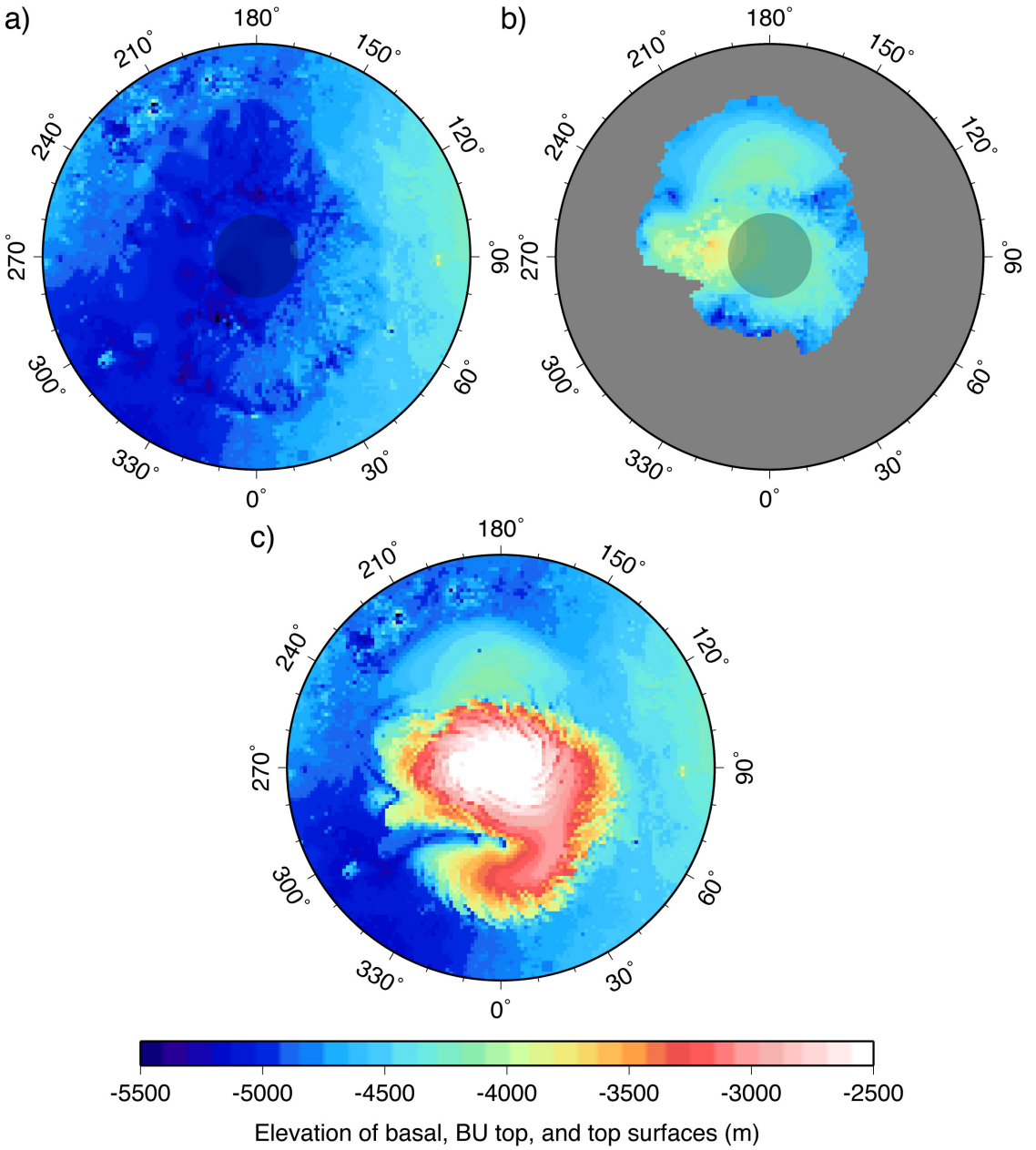

Figure 2.4. Surface elevation maps are provided for (a) the basal interface, which reveals no significant deflection of the elastic lithosphere under Planum Boreum, (b) the top of the Basal Unit (BU), and (c) the surface of the deposits (from MOLA data). Gray circles indicate lack of MARSIS coverage. Maps are in polar stereographic projection for 75° N – 90° N.

Elevation of the basal interface (Figure 4a) is interpolated after subtracting full thickness measurements (Figure 2a) from the surface elevation (MOLA); surface elevation values surrounding Planum Boreum are also included in the interpolation. Elevation at the top of the BU (Figure 4b) is determined by subtracting the NPLD thickness measurements (Figure 3b) from surface elevation (where the NPLD lies on top of the BU), using surface elevation values in the Olympia Planum region (where the NPLD is not present), and interpolating the interface from the combined elevation values.

The VBF surface underlying Planum Boreum is relatively featureless in its topography like the rest of the northern plains (Figure 4a). The elevation of the basal interface very closely follows contours of the basal topography estimated using MOLA data within 75° – 70° N (compare Figures 2b and 2d). The two regions with little to no useful MARSIS data (see Figure 2a) may have topography that differs from the interpolated surface, but there is no indication of such on the periphery of these regions.

Volumes are determined for Planum Boreum and for the BU and NPLD separately, in each case by summing the averaged and interpolated thickness values for each 15×15 km cell (see Methods). We estimate uncertainties in the volumes by propogating errors in the interface positions, dielectric constant, and area for each unit. The average standard deviation in pixel difference between two interfaces is 0.81 pixels, whereas the average pixel difference is 11.4 for Planum Boreum, 7.0 for the NPLD, and 4.0 for the BU; relative error from picked interface positions is 7.1%, 11.6%, and 20.2% respectively). Relative error from the real dielectric constant $\boldsymbol{\varepsilon_r} = 3.0 \pm 0.5$ (multiplied by ½ because unit thickness scales with the square root of $\boldsymbol{\varepsilon_r}$) is 8.3%. Area is known to width of one cell (15 km), whereas the average radial dimension is 586 km for Planum Boreum, 519 km for the NPLD, and 483 km for the BU; relative error from area (multiplied by 2 because area scales with radius squared) is 5.1%, 5.8%, and 6.2% respectively. The sum of squares of these uncertainty contributions is the square of the overall uncertainty in volume estimates; an unquantified uncertainty results from map interpolation. Planum Boreum as a whole contains $(1.3 \pm 0.2) \times 10^6$

km^3 of material, whereas the NPLD has a volume of $(7.8\pm1.2) \times 10^5$ km^3 and the BU has a volume of $(4.5\pm1.0) \times 10^5$ km^3. Some additional uncertainty in the these volume estimates is due to the following geometric effects, which likely cause the volume of the ice deposits to be underestimated.

Due to the lack of MARSIS coverage poleward of 87° N, no detection of the basal interface beneath a portion of the BU (270° – 300° E), and the systematic underestimate of the extent of the deposits (since ~300 m of ice thickness is necessary to distinguish upper and lower surfaces of a layer), our volume results are necessarily underestimates. The interpolated thickness of Planum Boreum north of 87° latitude is ~2200 m, which generally agrees with topography-based estimated thicknesses along the circle of 87° N, but does not agree with the MOLA-based maximum estimated thickness at the north pole of ~3000 m (see Figure 2). The circle of ~300 km diameter (i.e., 3° of latitude in radius) around the north pole contains an additional $\sim1.9\times10^4$ km^3 of deposits (assuming a cone with a height of ~800 m). In the 290° – 300° E region, where we observe no basal reflections in MARSIS data, the interpolated thickness drops off gradually while the MOLA-based estimated thickness remains constant and thick to the edge of the deposits (see Figure 2b and 2d, respectively); the 5×5 pixel (75×75 km) area of greatest discrepancy between measured and estimated thickness (a difference of ~1000 m) likely has an additional volume of $\sim5.6\times10^3$ km^3.

The volume of the thin margins (<300 m thick) of the deposits is an additional source of uncertainty in our volume estimates, and is most relevant for the gradually tapered margins of Planum Boreum, such as in the Olympia Planum region and around the Gemina Lingula lobe. Using Planum Boreum thickness maps from SHARAD data [*Putzig et al.*, 2009], which have a vertical resolution of 10 m, an average slope of 0.40° is estimated for the margins of the Gemina Lingula lobe with thickness <300 m. Assuming the same slope for the Olympia Planum lobe of Planum Boreum, and a total length of 2840 km for both regions with gently sloped margins, an estimated 1.8×10^4 km^3 of material is undetected by MARSIS along the edges of the deposits.

Together, the three underestimated portions of Planum Boreum represent approximately 4.3×10^4 km^3 of material, or 3% of the Planum Boreum volume (1.3×10^6 km^3). This represents a significantly smaller uncertainty in our volume estimate than the error in the volume calculation itself (due to resolution of the radargrams, error in picking reflectors, error in the area of the unit, error in interpolation, and uncertainty in the value of the real dielectric constant). Therefore the most likely volume for Planum Boreum is robustly determined to be $(1.3\pm0.2) \times 10^6$ km^3.

Implications for formation and preservation of Planum Boreum

Since MARSIS uniquely detects the interface between Planum Boreum and the underlying VBF material, various hypotheses can be addressed concerning the extent and structure of the constituent units of Planum Boreum. The lack of lithospheric deflection under the deposits is confirmed (within the error of ±200 m) (Figure 4a). Using SHARAD data for the Gemina Lingula lobe, Phillips et al. [2008] estimated an elastic lithospheric thickness of ~300 km in the vicinity of the north pole; the lack of detection of lithospheric deflection under the BU as well shows that a thick lithosphere must have existed not only before the NPLD was emplaced, but before the older BU was emplaced. This line of evidence extends the period of time during which a thick lithosphere has existed in the northern polar region to ~1 Ga, potentially as long ago as the ~3 Ga age of the VBF [*Tanaka*, 2005; *Tanaka et al.*, 2008], which is an upper bound for the age of the BU.

Using both SHARAD [*Putzig et al.*, 2009] and MARSIS data at 87.0° N to measure NPLD thickness provides good agreement between the two data sets, with values of up to ~1800 m and ~1700 m respectively (both measurements taken from the ~45° E longitude direction). However, SHARAD data are interpolated to obtain a maximum NPLD thickness of ~2000 m at the north pole [*Putzig et al.*, 2009], whereas with interpolated MARSIS data the NPLD thickness is ~1400 m at the same location (Figure 3b); this discrepancy can be attributed to a difference in coverage, with

SHARAD data going up to 87.4° N, whereas MARSIS data only extends to 87.0° N. If the estimated Planum Boreum thickness of ~3000 m at the north pole is correct (using topography, see Figure 2d), and ~2000 m of that is NPLD, the expectation is for the BU to be ~1000 m thick at the north pole; the interpolated BU thickness of ~800 m at the north pole agrees with this expectation (within error).

Our volume estimates also agree with previous studies; the NPLD volume of $(7.8\pm1.2) \times 10^5$ km^3 encompasses the SHARAD result of 8.2×10^5 km^3 [*Putzig et al.*, 2009], and the Planum Boreum volume of $(1.3\pm0.2) \times 10^6$ km^3 agrees with the lower bound of $(1.2\pm0.2) \times 10^6$ km^3 from Zuber et al. [1998], their case in which no deflection of the lithosphere has occurred. Our estimate for the volume of Planum Boreum is similar to the estimate of $(1.6\pm0.2) \times 10^6$ km^3 for the SPLD [*Plaut et al.*, 2007a]. Our estimate of the BU volume of $(4.5\pm1.0) \times 10^5$ km^3 significantly revises the previous rough estimate of 2.7×10^5 km^3 [*Byrne and Murray*, 2002]; we directly measure approximately twice as much material in the BU than was initially estimated using a simple spherical cap geometry to represent the then-unknown shape of the BU.

The two radar instruments at Mars directly detect the boundary between the BU and NPLD within the interior of Planum Boreum, but only MARSIS measures BU thickness, and the lateral extent of the BU in the Olympia Planum area. For the portions of the BU top surface that SHARAD is able to detect (where the NPLD lies on top of the BU), elevation contours at the top of the BU agree within error for MARSIS (Figure 4b) and SHARAD data [e.g., Figure 10 in *Putzig et al.*, 2009]. The most accurate and complete map to date of BU extent is provided in Figure 3a. An exception to the increased accuracy of our mapped BU extent is in the 270° – 300° E range, in which BU material is identified in imagery [*Fishbaugh and Head*, 2005; *Herkenhoff et al.*, 2007] but no radar returns are detected from the base of the BU.

This portion of the BU appears to have physical characteristics unlike the rest of the BU, which prevent MARSIS signals either from penetrating the BU or from coherently returning from the

basal interface, or both. Putzig et al. [2009] show that topography at the BU-NPLD interface has more relief (>1000 m) in this region than anywhere else in Planum Boreum, although why that should prevent MARSIS from detecting the base of the BU is not clear. Other hypotheses for the lack of basal reflection in this region exist, although MARSIS data cannot be used to distinguish between them. The structure of the BU may be different in this region from the rest of the BU, perhaps causing the radar energy to scatter incoherently. A paleo-dunefield, erosional lag or other rough paleo-surface may exist at either the BU-NPLD or BU-VBF boundaries that scatter incoming radar energy. The latter hypothesis would suggest that Planum Boreum not only differs structurally from the SPLD by having two distinct icy units (NPLD and BU), but that the BU itself may be composed of more than one unit of paleo-polar material. Not only is there no evidence of a BU-like unit at the south pole of Mars, with the characteristic diffuse scattering in radar return, there is additionally no evidence for an accumulation of distinct paleo-polar deposits in the south as there is in the north.

Based on the strength of the radar return from the base of the rest of the BU (e.g., Figure 1a), indicating little attenuation of the signal, it is likely that the BU contains only a few percent contaminants mixed with water ice. This makeup of the BU implies a similar bulk composition to the NPLD [*Picardi et al.*, 2005] and SPLD [*Plaut et al.*, 2007a]. The basal reflector is generally sharper and stronger in intensity in MARSIS data of the SPLD [*Plaut et al.*, 2007a] compared with that beneath Planum Boreum. However, as in Planum Boreum, there are portions of the SPLD where the basal reflector is weak or absent in MARSIS data. Several characteristics of the BU indicate that it is appreciably different in composition from the PLD. The BU is older, optically darker, less finely layered, and further offset from the pole than the NPLD; it returns a diffuse radar signal that is unique to icy deposits on Mars, and its base is typically detected by MARSIS but not SHARAD. These differences from other polar deposits on Mars may indicate that the regional climate in which the BU formed was different from that of the Martian poles today, and of the climate during which the NPLD and SPLD formed.

Unlike the icy deposits at the south pole of Mars, which are composed of only SPLD material, the structure and composition of Planum Boreum suggest different overall climate conditions during the periods of BU and NPLD formation. The different visual and radar appearances of the BU and NPLD, and the offset location of the BU from the north pole, indicate at least two distinct regimes of depositional and/or erosional conditions during the construction of Planum Boreum. While the age of the SPLD potentially allows seeing 100s of Ma into the climate history of southern Mars, Planum Boreum is likely a much older repository of climate data, which allows for investigation further back into the past environmental conditions of northern Mars.

Acknowledgments

This paper is dedicated to the late Ali Safaeinili, whose passion, skill, and support were both inspiring and essential for the completion of this study. Part of the research described in this publication was carried out at the Jet Propulsion Laboratory, California Institute of Technology, under a contract with NASA. Support from the NASA-Mars Express project is gratefully acknowledged.

References

Banks, M. E., K. Galla, S. Bryne, A. S. McEwen, V. J. Bray, K. E. Fishbaugh, K. E. Herkenhoff, B. C. Murray, and the HiRISE Science Team (2009), Crater population and resurfacing of the Martian north polar layered deposits, *Geol. Soc. Am. Abstr. Programs, 41*, 363.

Byrne, S., and B. C. Murray (2002), North polar stratigraphy and the paleo-erg of Mars, *Journal of Geophysical Research*, *107*(E6), 5044, doi:10.1029/2001JE001615.

Cutts, J. (1973), Nature and origin of layered deposits of the Martian polar regions, *Journal of Geophysical Research*, *78*(20), 4231-4249.

Fishbaugh, K. E., and J. W. Head III (2005), Origin and characteristics of the Mars north polar basal unit and implications for polar geologic history, *Icarus*, *174*(2), 444-474.

Herkenhoff, K. E., and J. J. Plaut (2000), Surface ages and resurfacing rates of the polar layered deposits on Mars, *Icarus*, *144*(2), 243-253.

Herkenhoff, K. E., S. Byrne, P. S. Russell, K. E. Fishbaugh, and A. S. McEwen (2007), Meter-scale morphology of the north polar region of Mars, *Science*, *317*, 1711-1715.

Koutnik, M., S. Byrne, and B. Murray (2002), South polar layered deposits of Mars: The cratering record, *Journal of Geophysical Research*, *107*(E11), 5100.

Laskar, J., B. Levrard, and J. Mustard (2002), Orbital forcing of the Martian polar layered deposits, *Nature*, *419*, 375-377.

Levrard, B., F. Forget, F. Montmessin, and J. Laskar (2007), Recent formation and evolution of northern Martian polar layered deposits as inferred from a global climate model, *Journal of Geophysical Research*, *112*(E06012), doi:10.1029/2006JE002772.

Malin, M., and K. Edgett (2001), Mars Global Surveyor Mars Orbiter Camera- Interplanetary cruise through primary mission, *Journal of Geophysical Research*, *106*(E10), 23,429-23,570.

Milkovich, S. M., J. J. Plaut, A. Safaeinili, G. Picardi, R. Seu, and R. J. Phillips (2009), Stratigraphy of Promethei Lingula, south polar layered deposits, Mars, in radar and imaging data sets, *Journal of Geophysical Research*, *114*(E03002), doi:10.1029/2008JE003162.

Pathare, A., D. Paige, and E. Turtle (2005), Viscous relaxation of craters within the martian south polar layered deposits, *Icarus*, *174*(2), 396-418.

Phillips, R. J., et al. (2008), Mars north polar deposits: Stratigraphy, age, and geodynamical response, *Science*, *320*(5880), 1182-1185.

Picardi, G., et al. (2004), Performance and surface scattering models for the Mars Advanced Radar for Subsurface and Ionosphere Sounding (MARSIS), *Planetary and Space Science*, *52*, 149-156.

Picardi, G., et al. (2005), Radar soundings of the subsurface of Mars, *Science*, *310*, 1925-1928.

Plaut, J. J., G. Picardi, A. Safaeinili, A. Ivanov, S. M. Milkovich, A. Cicchetti, W. Kofman, J. Mouginot, W. Farrell, and R. Phillips (2007a), Subsurface radar sounding of the south polar layered deposits of Mars, *Sciencexpress*, doi:10.1126/science.1139672.

Plaut, J. J., A. Ivanov, A. Safaeinili, S. M. Milkovich, G. Picardi, R. Seu, and R. Phillips (2007b), Radar sounding of subsurface layers in the south polar plains of Mars: Correlation with the Dorsa Argentea Formation, *Lunar Planet. Sci. XXXVIII*, Abstract 2144.

Plaut, J. J., K. E. Fishbaugh, J. W. Holt, K. E. Herkenhoff, S. M. Milkovich, S. Byrne, and N. E. Putzig (2009), What causes radar reflections inside Martian polar deposits?, *Geol. Soc. Am. Abstr. Programs, 41*, 68.

Putzig, N., R. J. Phillips, B. A. Campbell, J. Holt, J. Plaut, L. Carter, A. Egan, F. Bernardini, A. Safaeinili, and R. Seu (2009), Subsurface structure of Planum Boreum from Mars Reconnaissance Orbiter Shallow Radar soundings, *Icarus*, *204*(2), 443-457, doi:10.1016/j.icarus.2009.07.034.

Safaeinili, A., W. Kofman, J.-F. Nouvel, A. Herique, and R. L. Jordan (2003), Impact of Mars ionosphere on orbital radar sounder operation and data processing, *Planetary and Space Science*, *51*, 505-515.

Seu, R., et al. (2007), SHARAD sounding radar on the Mars Reconnaissance Orbiter, *Journal of Geophysical Research*, *112*(E05S05), doi:10.1029/2006JE002745.

Soderblom, L. A., M. C. Malin, J. A. Cutts, and B. C. Murray (1973), Mariner 9 observations of the surface of Mars in the north polar region, *Journal of Geophysical Research*, *78*(20), 4197-4210.

Squyres, S. W. (1979), The evolution of dust deposits in the Martian north polar region, *Icarus*, *40*(2), 244-261.

Tanaka, K. L. (2005), Geology and insolation-driven climatic history of Amazonian north polar materials on Mars, *Nature*, *437*(13), 991-994.

Tanaka, K. L., J. A. P. Rodriguez, J. A. Skinner Jr., M. C. Bourke, C. M. Fortezzo, K. E. Herkenhoff, E. J. Kolb, and C. H. Okubo (2008), North polar region of Mars: Advances in stratigraphy, structure, and erosional modification, *Icarus*, *196*(2), 318-358.

Thomas, P., S. Squyres, K. Herkenhoff, A. Howard, and B. Murray (1992), Polar deposits of Mars, in *Mars*, edited by H. Kieffer, B. M. Jakosky, C. W. Snyder and M. S. Matthews, pp. 767-795, University of Arizona Press, Tuscon.

Zuber, M. T., et al. (1998), Observations of the north polar region of Mars from the Mars Orbiter Laser Altimeter, *Science*, *282*, 2053-2060.

Zuber, M. T., R. J. Phillips, J. C. Andrews-Hanna, S. W. Asmar, A. S. Konopliv, F. G. Lemoine, J. J. Plaut, D. E. Smith, and S. E. Smrekar (2007), Density of Mars' south polar layered deposits, *Science*, *317*, 1718-1719.

Chapter 3

CONSTRAINTS ON JALISCO BLOCK MOTION AND TECTONICS OF THE GUADALAJARA TRIPLE JUNCTION FROM 1998 – 2001 CAMPAIGN GPS DATA[2]

A GPS campaign network in the state of Jalisco was occupied for ~36 hours per station most years between 1995 and 2005; we use data from 1998 – 2001 to investigate tectonic motion and interseismic deformation in the Jalisco area with respect to the North America plate. The twelve stations used in this analysis provide coverage of the Jalisco Block and adjacent North America plate, and show a pattern of motion that implies some contribution to Jalisco Block boundary deformation from both tectonic motion and interseismic deformation due to the offshore 1995 earthquake. The consistent direction and magnitude of station motion on the Jalisco Block with respect to the North America reference frame, ~2 mm/yr to the southwest (95% confidence level), perhaps can be attributed to tectonic motion. However, some station velocities within and across the boundaries of the Jalisco Block are also non-zero (95% confidence level), and the overall pattern of station velocities indicates both viscoelastic response to the 1995 earthquake and partial coupling of the subduction interface (together termed "interseismic deformation"). Our results show motion across the northern Colima rift, the eastern boundary of the Jalisco Block, which is likely to be sinistral oblique extension rather than pure extension. We constrain extension across both the Colima rift and the northeastern boundary of the Jalisco Block, the Tepic-Zacoalco rift, to ≤8 mm/yr (95% confidence level), slow compared to relative rates of motion at nearby plate boundaries.

---

[2] This chapter is published in its entirety under the same title by authors M. M. Selvans, J. M. Stock, C. DeMets, O. Sanchez, and B. Marquez-Azua (2010), in *Pure and Applied Geophysics*, doi: 10.1007/s00024-010-0201-2.

Introduction

Jalisco is an interesting region for geodetic study for two main reasons. First, geologic evidence points to concentrations of tectonic deformation in two bounding rifts inland from the Rivera plate, the Tepic-Zacoalco and Colima rifts (see Figure 1). Second, following the Oct. 9, 1995 (M_w = 8.0) Colima-Jalisco earthquake, the hinge of deformation (between subsidence and uplift) quickly moved onshore [*Melbourne et al., 2002*], providing better Global Positioning System (GPS) coverage of overall deformation than exists for most subduction megathrusts. Neither the deformation due to the earthquake cycle nor the local tectonics is fully understood.

This study seeks to constrain the tectonic motion of the Jalisco Block with respect to North America. We use average velocities during 1998 – 2001 for a network of twelve GPS stations to investigate rifting rates across the Tepic-Zacoalco and Colima rifts, as well as motion across the Chapala rift. We also investigate the contribution to station motion from earthquake cycle effects. The 1995 M_w = 8.0 event offshore from Jalisco may contribute significantly to the velocities of the network stations, so careful consideration of both tectonic and earthquake cycle signatures in the GPS data is necessary.

Constraining the current rate of tectonic motion in the Jalisco area will narrow down the likely scenarios for ongoing deformation in a region of active plate rearrangement [e.g., *Luhr et al., 1985; Johnson and Harrison, 1990; Allan et al., 1991; Ferrari, 1995; Rosas-Elguera et al., 1996; DeMets and Traylen, 2000*]. The Jalisco Block lies onshore from the northernmost section of the Middle America Trench, above the subducting Rivera plate, just south of rifting in the Gulf of California, and has often been cited as an example of continental rifting [*e.g., Luhr et al., 1985*].

Characterizing the pattern and magnitude of earthquake cycle effects in the dataset is essential to its reliable interpretation. GPS analysis and modeling of the coseismic and postseismic (transient) effects of the 1995 earthquake [*Hutton et al., 2001*; *Masterlark et al., 2001; Marquez-Azua et al.,*

2002], indicate that some signature of the earthquake cycle is expected during our study period, likely due to viscoelastic deformation of the mantle beneath our study area and partial to full coupling of the subduction interface (together termed "interseismic deformation").

We assess our network velocities with respect to forward-modeling predictions of earthquake cycle phenomena and predictions of multiple hypotheses for tectonic motion of the Jalisco Block. These phenomena predict different station velocity patterns: (1) stations on the Jalisco Block move together to the west or southwest relative to North America, due to rifting of the Jalisco Block from North America, (2) all stations move toward the 1995 rupture zone, due to viscoelastic response of North America to the earthquake, and (3) all stations move away from the 1995 rupture zone, due to partial coupling of the subduction interface. The first prediction has three variants (detailed below), based on alternative hypotheses for the formation and motion of the Jalisco Block and its bounding rifts. We also examine the smaller region around the "Guadalajara triple junction" (where three rifts–the Tepic-Zacoalco, Chapala, and Colima rifts–meet each other). For this region, we assume local tectonic rates dominate over any viscoelastic gradients, permitting us to place constraints on the velocity triangle that includes North America and the Jalisco and Michoacan Blocks, which surround this triple junction (e.g., *Johnson and Harrison, 1990*).

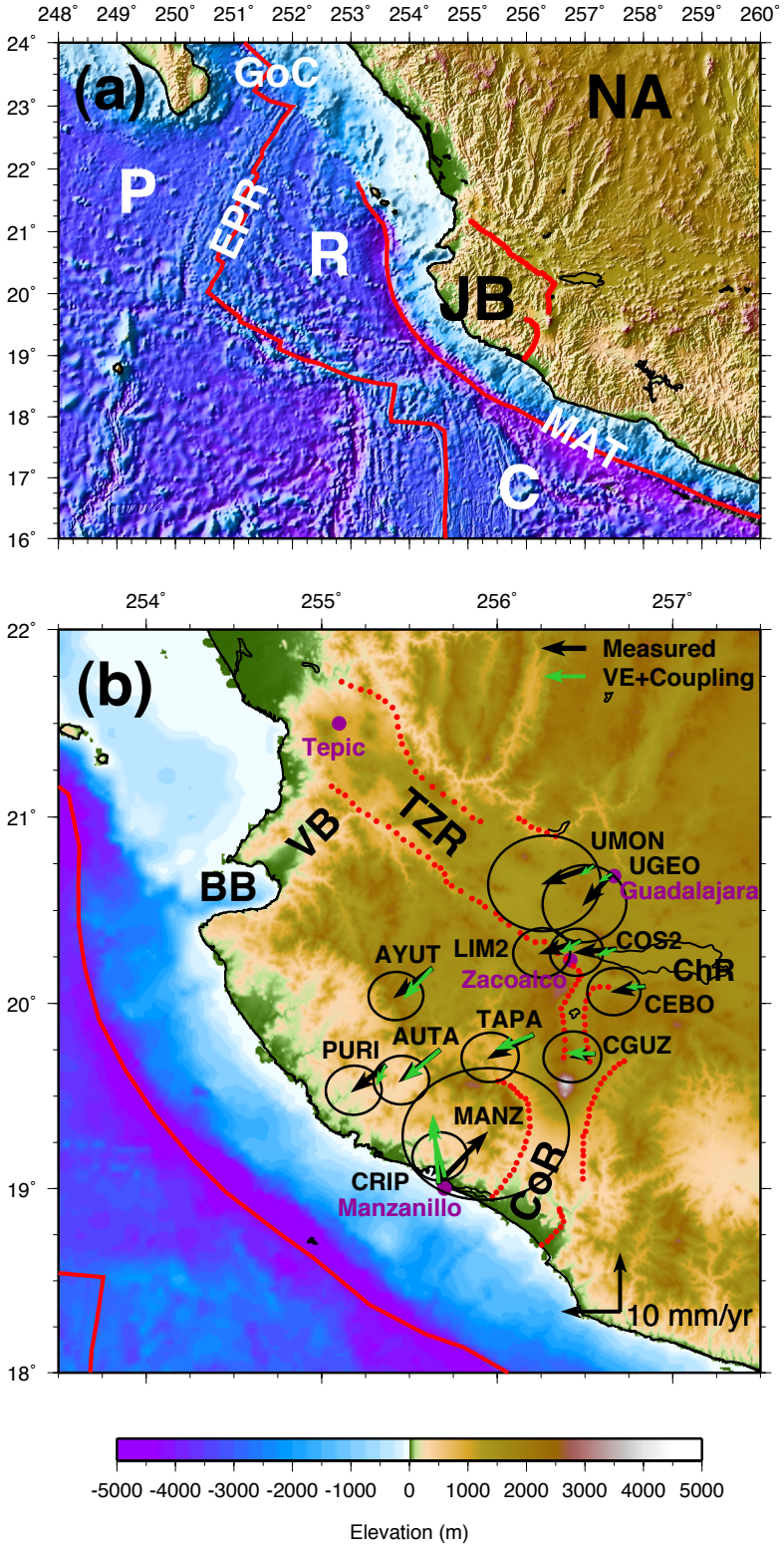
(a)
GoC
NA
P
EPR
R
JB
MAT
C
(b)
Measured
VE+Coupling
Tepic
VB
TZR
BB
UMON
UGEO
Guadalajara
COS2
LIM2
Zacoalco
ChR
AYUT
CEBO
TAPA
AUTA
CGUZ
PURI
MANZ
CRIP
Manzanillo
CoR
10 mm/yr
248° 249° 250° 251° 252° 253° 254° 255° 256° 257° 258° 259° 260°
24° 23° 22° 21° 20° 19° 18° 17° 16°
254° 255° 256° 257°
22° 21° 20° 19° 18°
-5000 -4000 -3000 -2000 -1000 0 1000 2000 3000 4000 5000
Elevation (m)

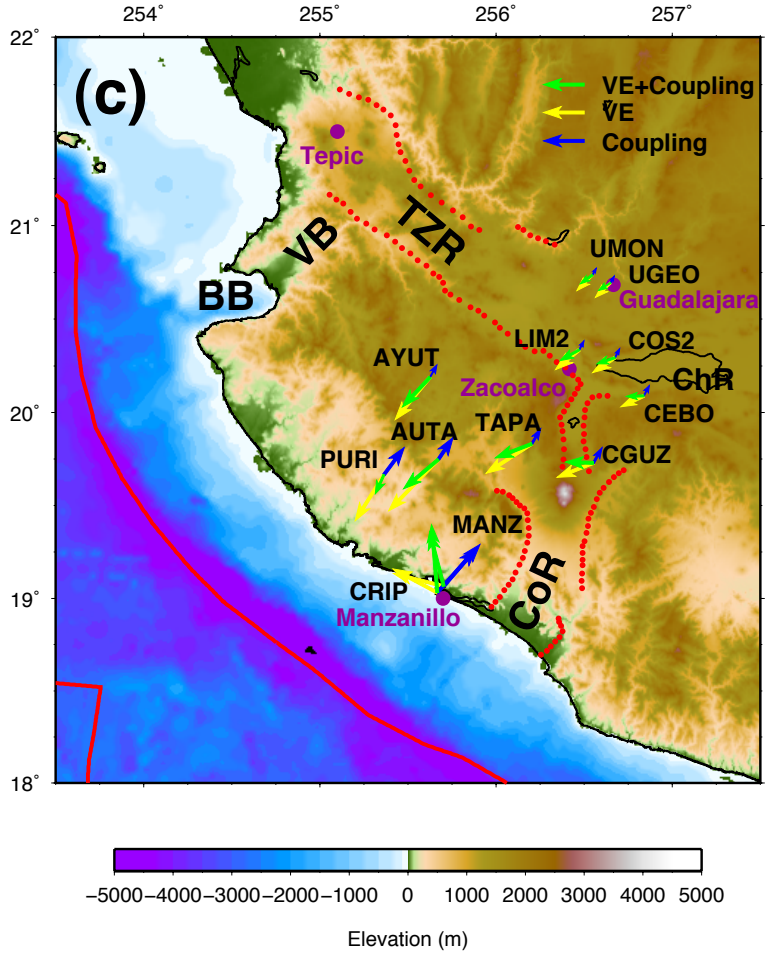

Figure 3.1. (a) Topography and bathymetry of western Mexico shows the plate tectonic context for the Jalisco Block (JB), with plate boundaries and Jalisco Block boundaries in red. The Jalisco Block is just southeast of the Gulf of California (GoC), and may move rigidly with respect to North America (NA). The Pacific (P) and Rivera (R) plates diverge at the East Pacific Rise (EPR). The Rivera and Cocos (C) subduct along the Middle America Trench (MAT). **(b)** Twelve GPS sites used in this study lie on the Jalisco Block and surround the rift-rift-rift triple junction, where the Tepic-Zacoalco, Colima, and Chapala rifts meet (TZR, CoR, and ChR, respectively; bounding faults for the Tepic-Zacoalco and Colima rifts are shown in red, after Allan et al. [*1986*] and Ferrari et al. [*1994*]). Bahía de Banderas (BB) and the Valle de Banderas (VB) are the proposed northwest boundary of the Jalisco Block [*e.g. Johnson and Harrison, 1990*]. Rivera plate boundaries are after DeMets and Wilson [*1997*]. Station velocities with respect to North America are plotted in black (see Appendix II, Table 1), with north and east errors displayed as 2D 95% confidence intervals. For comparison, modeled interseismic velocity vectors are shown in green. **(c)** Modeled vectors include partial coupling along the subduction interface (50% coupling shown in blue) and viscoelastic (VE) deformation of the overriding plate (yellow) [*Masterlark et al., 2001; Marquez-Azua et al., 2002*]. All measured and predicted station velocities are scaled to the reference vectors in the lower right. Shuttle Radar Topography Mission data and estimated seafloor topography are ~1 km resolution [*Becker and Sandwell, 2006*].

Tectonic Setting

Regional Tectonics

Jalisco is a coastal state of western mainland Mexico, located southeast of the Gulf of California (Figure 1a). The surrounding region is shaped by a series of recent tectonic events, including subduction along the west coast of North America, an eastward jump of the East Pacific Rise to produce rifting in the Gulf of California, and separation of the Rivera and Cocos plates, resulting in the current differential subduction beneath Jalisco and the rest of western Mexico to the southeast. Convergence is slower between the Rivera and North America plates than between the Cocos and North America plates, and is increasingly oblique from south to north along the Rivera-North America trench [e.g., *Kostoglodov and Bandy, 1995*; *DeMets and Traylen, 2000*].

Boundaries of the Jalisco Block

The Tepic-Zacoalco rift consists of several tectonic depressions bounding the northeastern extent of a topographically high portion of the state of Jalisco (Figure 1b). Structural mapping of the Tepic-Zacoalco rift indicates some extension and right-lateral motion occurred ~12 – 8.5 Ma, with extension continuing to the present day, probably related to opening of the Gulf of California [*Ferrari, 1995; Frey et al., 2007*]. Recent rates of motion are small, with average minimum deformation rates that decrease from 0.75 mm/yr in the Late Miocene to 0.1 mm/yr in the Quaternary [*Ferrari and Rosas-Elguera, 2000*]. Beginning at 4.7 Ma, alkaline and calc-alkaline volcanic lavas were concentrated within the Tepic-Zacoalco rift, some with compositions commonly found in ocean islands and intraplate rifts [*e.g., Allan et al., 1991*]. Furthermore, rhyolitic ignimbrites were emplaced in this rift in an order of magnitude greater volume during the interval of 5 – 3 Ma than is documented for the volcanism of the last ~1 Ma, indicating significant lithospheric extension occurred during that time [*Frey et al., 2007*]. Seismicity to a depth of ~35 km within the Tepic-Zacoalco rift also indicates deep crustal faulting between the Jalisco Block

and North America [*Nuñez-Cornú et al., 2002*]. Additionally, a tomographic study of the crust and upper mantle in Jalisco and adjacent states reveals distinct low velocity lineaments beneath both the Tepic-Zacoalco and Colima rifts [*Wang et al., 2008*]; in the upper mantle, these features are associated with tearing of the subducted slab [*Yang et al., 2009*].

The Colima rift bounds the eastern edge of the Jalisco highlands (Figure 1b). Except for the massive deposition of rhyolitic ignimbrites *[Frey et al., 2007*], volcanism within this Jalisco Block boundary is similar in composition and duration to that of the Tepic-Zacoalco rift [*e.g., Allan et al., 1991*]. Since ~5 Ma, rocks of the southern Colima rift have been faulted, both onshore [e.g., *Garduño-Monroy et al., 1998*] and offshore [*Bourgois et al., 1988; Khutorskoy et al., 1994; Bandy et al., 2005*], and the northern Colima rift has subsided 0.07 – 0.7 mm/yr [*Rosas-Elguera et al., 1996*]. Other crustal faults, such as the Tamazula fault to the west of the southern Colima rift, may now form the southeastern boundary of the Jalisco Block [*Garduño-Monroy et al., 1998*]. These faults have had recent seismic activity [*Garduño-Monroy et al., 1998*; *Pacheco et al., 2003*; *Andrews et al*., 2010]. Farther north, the eastern edge of the Jalisco block is roughly aligned with a sharp change in slab dip just east of the Colima rift [*Pardo and Suarez, 1995*], visible in seismic tomography [*Grand et al., 2007; Yang et al., 2009*].

The Zacoalco half-graben lies at the continental rift-rift-rift triple junction (termed the Guadalajara triple junction) where the Tepic-Zacoalco, Colima, and Chapala rifts come together. A sequence of magnitude 1.5 – 3.5 earthquakes in 1997 on shallow normal faults [*Pacheco et al., 1999*] confirms formation of the half-graben as tilt blocks overlying listric faults [*Rosas-Elguera et al., 1997*]; additionally, the composite focal mechanism indicates possible right-lateral slip along a northwest-southeast oriented nodal plane within the Zacoalco graben near the triple junction [*Pacheco et al., 1999*]. Historical records indicate the potential for much larger earthquakes at this triple junction, such as the >7.0 magnitude earthquake of December 27, 1568 [*Suarez et al., 1994*].

Receiver functions reveal Moho depths of 25 – 45 km in the continental interior of the Jalisco Block [*Suhardja et al., 2007*]. To fully delineate the inland boundaries of the Jalisco Block, its

northwestern corner must be defined. Seismicity and structural mapping suggest Valle de Banderas, trending northeast from Bahía de Banderas to the Tepic-Zacoalco rift, has been the northwestern limit of the Jalisco Block since ~5 Ma [*e.g., Johnson and Harrison, 1990*; *Nuñez-Cornú et al., 2002*]; these lines of evidence are corroborated by gravity and magnetics data [*Arzate et al., 2006*]. An alternative interpretation of the geologic and magnetic data is that the northwest boundary of the Jalisco Block follows this same trend, but is located just to the northwest of Valle de Banderas [*Urrutia-Fucugauchi and Gonzalez-Moran, 2006*]. While deformation is possible within and along all boundaries of the Jalisco Block, this study focuses on characterizing motion across the two most prominent boundaries between the Jalisco Block and neighboring continental material, the Tepic-Zacoalco and Colima rifts.

Predictions of Current Deformation

Hypotheses for Block Motion

Three hypothetical scenarios for the formation and motion of the Jalisco Block could explain the current morphologies of the Tepic-Zacoalco and Colima rifts. An early hypothesis for Jalisco Block formation and motion, based on regional tectonics, the clear inland delineation of the Jalisco Block by the Tepic-Zacoalco and Colima rifts, and the composition of volcanism in the rifts, was an imminent eastward jump of the East Pacific Rise to the Colima rift [*e.g., Luhr et al., 1985*]. This hypothesis suggests the eventual attachment of the Jalisco Block to the Pacific plate (i.e., northwestward motion with respect to North America), and predicts opening in the Colima rift and primarily right-lateral strike slip along the Tepic-Zacoalco rift. A variant of this hypothesis, based on similarities between volcanism in the Tepic-Zacoalco rift and that of the Gulf of California 12 – 6 Ma, is that recent Tepic-Zacoalco volcanism is a precursor to rifting of the Jalisco Block from North America [*Frey et al., 2007*].

Alternatively, the Tepic-Zacoalco and Colima rifts are explained as passive responses of North America to tearing of the subducting slab, which stresses the continental crust [*e.g., Ferrari, 1995, 2004*]. The Colima rift approximately overlies the sharp change in dip between the Rivera and Cocos slabs [*Pardo and Suarez, 1995*] and, as with the Tepic-Zacoalco rift, overlies a region of low seismic velocities; respectively, these low velocities may be due to differential motion between the subducting slabs [e.g., *Stock, 1993*] and a lateral tear in the Rivera slab [e.g., *Nixon, 1982*]. This hypothesis for Jalisco Block motion predicts opening along both the Colima and Tepic-Zacoalco rifts (i.e., southwestward motion with respect to North America), with the possibility of motion being dominantly trenchward (southward) [*Ferrari et al., 1994; Rosas-Elguera et al., 1996*].

A third hypothesis for Jalisco Block formation and motion (which is potentially compatible with the preceding hypothesis) is that its inland boundaries accommodate little to no motion today, in keeping with geologic evidence for slow rates of opening (average minimums of <1 mm/yr) across the Tepic-Zacoalco and Colima rifts from the late Miocene through the Quaternary [*Rosas-Elguera et al., 1996; Ferrari and Rosas-Elguera, 2000*]. This hypothesis predicts opening of up to a few millimeters per year across the inland Jalisco Block boundaries.

Earthquake Cycle Effects

The shallow portion of the slab interface ruptured in a pair of large earthquakes (M_w = 8.2 and M_w = 7.8) in 1932 [*Singh et al., 1985*], after which no large subduction-related earthquakes ruptured the Rivera plate subduction interface until 1995 (M_w = 8.0) and 2003 (M_W = 7.2) [e.g., *Melbourne et al., 1997; Pacheco et al., 1997; Yagi et al., 2004*]. After the 1995 earthquake, GPS stations within 200 km of the rupture zone exhibited rapidly decaying transient deformation attributable to a combination of afterslip focused along areas of the subduction interface downdip from the rupture zone and viscoelastic flow of the upper mantle due to the elevated stresses from the 1995 earthquake [*Hutton et al., 2001*; *Marquez-Azua et al., 2002; Melbourne et al., 2002*]. Finite

element modeling of the expected steady deformation from frictional coupling of the subduction interface and the transient, viscoelastically-induced deformation of the overriding North America plate shows that these two processes cannot by themselves match deformation recorded between 1993 and 2001 at a continuous GPS station directly onshore from the 1995 rupture zone [*Masterlark et al., 2001; Marquez-Azua et al., 2002*], in accord with the forementioned studies that conclude that fault afterslip contributed significantly to the deformation after the 1995 earthquake. Rapid transient postseismic deformation after the 1995 earthquake concluded by mid-1997, after which station motions were linear or nearly linear until the January 22, 2003 Tecoman M_W = 7.2 earthquake offshore from the study area triggered additional postseismic deformation consisting in part of aseismic fault afterslip [*Schmitt et al., 2007*].

By limiting the present analysis to GPS data collected from 1998 to 2001, we exclude the years when coseismic and postseismic signals (i.e., obvious deviations from strictly linear motion) associated with the 1995 and 2003 earthquakes dominated the station velocities (2002 is excluded because no campaign GPS data were collected that year). When interpreting our data, we assume these four years are representative of ongoing tectonic motion. However, motion of the Jalisco Block may have varied over the last few million years, and interseismic earthquake cycle effects may still contribute significantly to motion of GPS sites during the time interval of our study.

Viscoelastic response of North America to the 1995 event would cause stations in our study to move southwestward toward the earthquake rupture zone, with the largest velocities closest to the epicenter, and similar directionality but decreasing magnitude at stations further inland (yellow vectors in Figure 1c). This effect would produce motion in generally the same direction as predicted by the second hypothesis for block motion, although in that case no strain gradient is expected. Partial coupling of the subduction interface would also result in a strain gradient, again with the largest magnitudes at the coast, but of generally northeastward motion (blue vectors in Figure 1c).

Differences in predicted strain patterns allow us to assess the relative contributions of viscoelastic response, partial coupling on the subduction interface, and tectonic motion. We do not expect other large-scale contributions to the station motion in the Jalisco area. Because GPS stations farther inland in northern Mexico do not move significantly with respect to North America [*Marquez-Azua and DeMets, 2003; 2009*], motion related to the Basin and Range region is not expected to influence our study area.

Data and Methods

Data Collection and Processing

We use ten GPS stations from a Jalisco campaign network, occupied for ~36 hours per station with up to four stations simultaneously operating [*Hutton et al., 2001*], as well as two continuous sites that ran for months at a time (UGEO and MANZ). We select these twelve stations to provide good coverage of the study area, including multiple data points on the Jalisco Block and baselines across the Tepic-Zacoalco and Colima rifts (Figure 1b), so that we can investigate internal deformation as well as motion concentrated in the Jalisco Block boundaries.

Our analysis includes 62 sessions (days) over the four-year time span. Fifteen GPS stations on North America (east of the Mojave desert) are used to define the reference frame relative to ITRF2000 [*Altamimi et al., 2002*]. Final orbits from the Jet Propulsion Laboratory are used for satellite positions.

For all sessions, loosely constrained least-squares solutions of position and velocity components, and their correlation matrices, are obtained for each station using GAMIT [*Herring et al., 1990*]. Using GLOBK [*Dong et al., 1998*], these quasi-observations for each session are processed with constraints on station position and velocity, reference frame motion, and orbital and Earth orientation parameter values, in order to determine station coordinate time series with respect to

North America. Further processing with the Markov process (white noise) in a recursive, time-domain Kalman filter allows us to obtain station velocities for 1998 – 2001. See Appendix I for more detail on the data processing.

GPS Velocity Estimation

Seven GPS stations show small amounts of significant motion with respect to North America (AUTA, AYUT, CEBO, COS2, LIM2, PURI, TAPA; see Appendix II, Table 1), with an overall pattern of southwestward and west-southwestward motion for all ten inland stations (black vectors in Figure 1b). Sites in the Jalisco Block interior (AUTA, AYUT, PURI, TAPA) move most similarly to each other compared with any other group of stations in this study, at 2-4 mm/yr to the southwest with respect to North America (95% confidence level, i.e., (9±6) mm/yr, (8±5) mm/yr, (8±6) mm/yr, and (9±6) mm/yr, respectively). Stations closest to the Guadalajara triple junction (LIM2, COS2) also move ~2 mm/yr with respect to North America (95% confidence level), in a more westward direction than those of the Jalisco Block interior. Since our uncertainties on vertical motion are so large, the contribution to LIM2 and COS2 motion from slip on high-angle normal faults and/or listric normal faults in the area [e.g., *Rosas-Elguera et al., 1997*] cannot be determined. This is also true for the stations on the Michoacan Block (CGUZ, CEBO), both of which are at the edges of the rifts they bound and so may also move in part due to local normal faulting. Five GPS stations (UMON, UGEO, CGUZ, CRIP, MANZ) do not move with respect to North America (95% confidence level), although we note that the coastal stations (CRIP and MANZ) do uniquely move inland. The direction of motion at stations CRIP and MANZ is likely due to interseismic strain accumulation [*Marquez-Azua et al., 2002; Schmitt et al., 2007*]; the relatively large error ellipse on the MANZ station is due to only having two years of data during the 1998 – 2001 interval, and our analyzing that data only on days when at least one campaign station was active.

Velocity Field Analysis Results

We use station TAPA as a reference point for station velocities (Appendix II, Table 2) because it is the station on the Jalisco Block closest to the Guadalajara triple junction. With respect to TAPA, we see no significant motion (lower end of the 95% confidence level) within the Jalisco Block or across the Colima and Tepic-Zacoalco rifts. Directly across the Colima rift from TAPA, the CGUZ station shows at most ~8 mm/yr eastward motion and ~7 mm/yr northward motion with respect to TAPA (upper end of the 95% confidence level), which provides an upper bound on the opening rate of the northern Colima rift during the years 1998 to 2001. Similarly with respect to TAPA, LIM2 limits the opening rate across the Zacoalco half-graben to a maximum of ~5 mm/yr east and ~6 mm/yr north.

We can further limit the range of possible motions by considering velocity constraints on the triple junction, using a flat-earth assumption involving only the stations closest to the triple junction (TAPA, CGUZ, CEBO, UMON, UGEO; see Figure 2). Our velocity diagram has northward velocity on the y-axis and eastward velocity on the x-axis. This diagram is centered on a velocity of zero, which corresponds to station TAPA, which we use as our local reference frame. The resulting velocities are minimum constraints on block motions.

We fix station TAPA, on the Jalisco Block (Figure 2a), and plot the best fit velocity vectors and their 95% confidence limits of the other 4 stations (values from Appendix II, Table 2 using the mathematical calculations of 2D Gaussian distributions [*e.g., Molnar & Stock, 1985*]). We then constrain the possibilities for block velocities further using the assumptions detailed in Appendix III.

For the N-S trending northern Colima rift, this indicates an upper limit on opening of ~8 mm/yr, with a significant component of left-lateral strike-slip possible (green shaded velocity field, Figure 2f); the lower limit of motion rate across the northern Colima rift is nearly 0 mm/yr (lower end of

the 95% confidence level). These velocity constraints allow for ~5 mm/yr of pure extension across the northern Colima rift (i.e., normal to its strike). Within the uncertainties they also permit alternatives such as up to 6 mm/yr of left-lateral motion or oblique sinistral transtension. Across the N56°W trending Tepic-Zacoalco rift, an upper limit of ~8 mm/yr opening between the Jalisco Block and North America is possible, with ~6 mm/yr of pure extension possible. Some amount of either pure left slip or pure right slip is possible (red shaded velocity field, Figure 2e).

These constraints on opening rates across the Tepic-Zacoalco and Colima rifts (in the vicinity of the Guadalajara triple junction) permit more movement of the Jalisco Block with respect to North America than is observed geologically (average minimum values of ~0.1 mm/yr since 5 Ma [*Rosas-Elguera et al., 1996; Ferrari and Rosas-Elguera, 2000; Frey et al., 2007*]), and yet are consistent with the geology within the 95% confidence level of the velocity estimates.

Although the above analyses are based on holding station TAPA fixed, it is important to note that all four of our stations on the Jalisco highlands (TAPA, PURI, AUTA, AYUT) have similar velocities with respect to North America. The significant and coherent motion of these four stations, ~2 mm/yr to the southwest with respect to North America, may be representative of rifting of the Jalisco Block with respect to North America with the caveat that viscoelastic deformation in response to the 1995 earthquake and partial coupling of the subduction interface may also contribute to the motions of these sites.

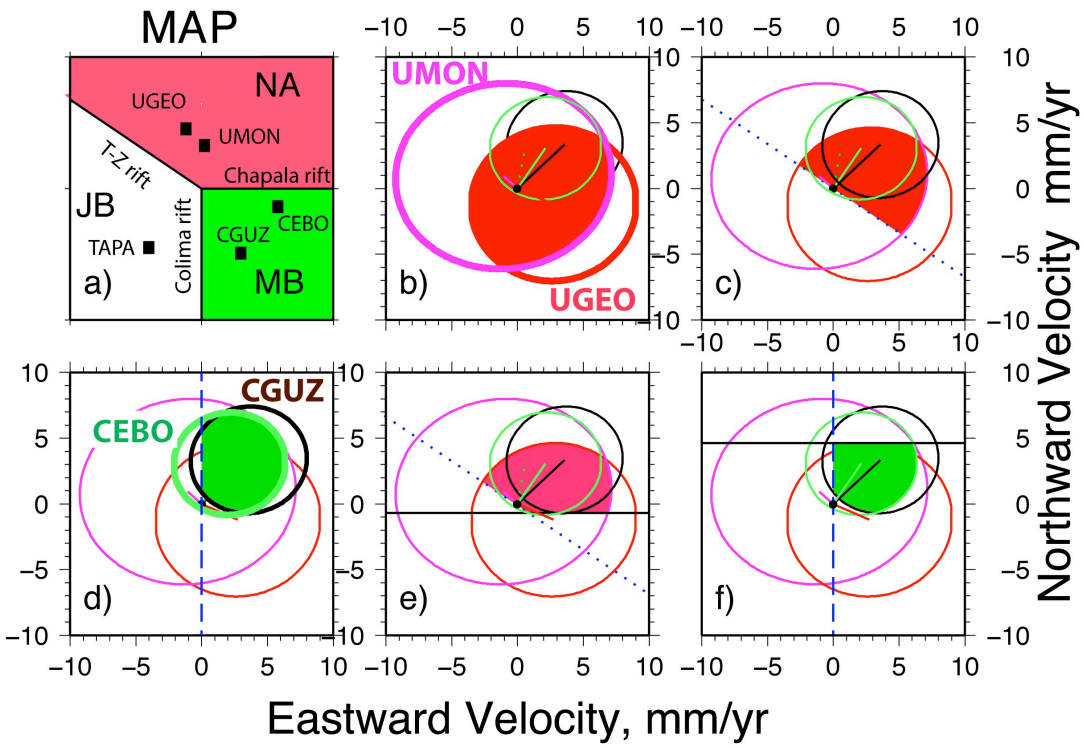

Figure 3.2. Velocity diagram analysis for a simplified Guadalajara triple junction constrains the sense of motion along the inland boundaries of the Jalisco Block (JB). **(a)** Schematic map showing the geometry of the triple junction and the location of the five stations. North America (NA) is in red; the Michoacan Block (MB) in green. Block JB (white) is the fixed block. Ellipses in panels (b) through (f) show the 95% confidence limits of station velocities relative to TAPA, whose velocity lies at the center of the diagram (black dot at coordinates 0,0). East-west velocity is on the horizontal axis; north-south velocity is on the vertical axis. Straight lines extending from the dot (best visible in panels (b) and (c)) indicate the best-fit velocity of each station with respect to TAPA, colored as follows: CEBO=green, CGUZ=black, UMON=pink, UGEO=red. **(b)** Intersection of UMON and UGEO ellipses shaded red to show allowable velocity values for NA motion relative to the JB. **(c)** Allowable velocities of NA relative to TAPA if no compression is occurring across the Tepic-Zacoalco (T-Z) rift. **(d)** Allowable velocities of the MB relative to TAPA if no compression is allowed across the northern Colima rift. **(e)** and **(f)** Allowable velocities of NA and the MB relative to TAPA if no compression is allowed across the Chapala rift. See Appendix III for a more detailed explanation.

To understand the potential contributions from viscoelastic deformation, partial coupling of the subduction interface, and tectonic motion, we look qualitatively at the pattern of station velocities. Within the uncertainties, a distinct strain gradient is absent in the four stations on the Jalisco highlands (in contrast to predictions of both partial plate coupling and viscoelastic deformation), suggesting some contribution from Jalisco Block tectonic motion to the overall station velocities for 1998 – 2001. However, the overall pattern of estimated station velocities compares favorably with the modeled combination of viscoelastic response to the 1995 earthquake and 50% coupling along the subduction interface of previous researchers (yellow and blue arrows, respectively, in Figure 1c) [*Masterlark et al., 2001; Marquez-Azua et al., 2002*].

The strain caused by coupling on the subduction interface consists of shortening, normal to the offshore subduction trench, counter to any extension across the Tepic-Zacoalco and Colima rifts. In contrast, the viscoelastic strain-rate gradient is extensional toward the rupture area of the 1995 earthquake, nearly opposite the sense of the gradient due to coupling, and so adds (temporarily) to any ongoing extension across the Tepic-Zacoalco or Colima rifts. The modeled and observed velocity vectors agree within the 2σ uncertainty ellipses, particularly with respect to the overall pattern of station motion (compare green and black vectors in Figure 1b). While this similarity is suggestive, the relative role of off-fault and fault rheologies is still an open question [*Wang, 2007*], and the closest station to the 1995 rupture zone (PURI) does not fit well into the pattern of station motion predicted by the model of interseismic deformation.

Discussion

Although no previous analyses of GPS data have focused on motion across the Tepic-Zacoalco and Colima rifts, it is encouraging that similar earthquake cycle studies agree with our station velocity results. We find that GPS stations moved only ~2 mm/yr with respect to the North America plate reference frame, when considered at the 95% confidence level (Figure 1b). Hutton *et al.* [*2001*]

analyze campaign and continuous GPS data in the area for 1995 – 1999, and report varying amounts of postseismic motion for 1998 – 1999 with respect to NA, from 0 mm/yr at CRIP, to ~10 mm/yr at TAPA and CEBO, to ~20 mm/yr at AUTA, AYUT, PURI, and UMON, all to the southeast or southwest. Of these stations, they find that only the last four have significant motion with respect to North America (~10 mm/yr at the 2σ level), and then only for the north component. Since this transient postseismic motion is well explained with a rate-and-state friction law model of the 1995 earthquake [*Hutton et al., 2001*], it is an upper bound on annual velocity at these stations, and so is consistent with the significant motion of ~2 mm/yr with respect to North America that we find at stations on the Jalisco highlands for 1998 – 2001 (at the 95% confidence level).

Schmitt *et al.* [*2007*] analyze 1996 – 2003 GPS data in the Jalisco area to model interseismic and postseismic deformation due to the 2003 earthquake. They find that for the 1998 – 2001 time period, CRIP moved northeast with respect to the North America reference frame, and that TAPA, AUTA, AYUT, CGUZ, CEBO, and LIM2 moved southwest, all by ~20 mm or less over the study period, or >7 mm/yr (in agreement with our velocity estimates, within 2σ error ellipses). Schmitt *et al.* [*2007*] do not report position component errors for each year, but do report them for coseismic offsets, so we use the latter for comparison. The 1σ error on coseismic position estimates for TAPA, PURI, LIM2, and UGEO is 2 – 10 times larger than the measurement itself, and similarly the 2σ error for CGUZ, AYUT, and CEBO is larger than measurements [*Schmitt et al., 2007*]. These relatively large errors suggest unresolved, although seemingly systematic, geodetic motion for 1998 – 2001 in the Jalisco area, as observed in our analysis of the data as well.

In both of the above analyses of Jalisco GPS data [*Schmitt et al., 2007; Hutton et al., 2001*], the intention was to model effects of the earthquake cycle on geodetic measurements in the area, and so neither focused on putting a robust constraint on the contribution from tectonic motion. We present a focused analysis of GPS data on and near the Jalisco Block that only covers the interseismic portion of the earthquake cycle, and obtain hard upper limits of 8 mm/yr for opening along both the Tepic-Zacoalco and Colima rifts (5 mm/yr and 6 mm/yr of pure extension,

respectively, near the Guadalajara triple junction). Interestingly, for the northern Colima rift there also may be significant left-lateral strike-slip motion (up to 5 mm/yr of pure left-lateral strike-slip) and in fact some left-lateral strike-slip motion is required for the minimum allowed velocity based on our velocity diagram analysis (Figure 2). These constraints may include Jalisco Block motion with respect to North America, as well as partial coupling of the subduction zone and viscoelastic response of the overriding North America plate (i.e., interseismic deformation).

In terms of the hypotheses for Jalisco Block motion, the data do not support an eastward jump of the East Pacific Rise, because we do not find the motion across the Tepic-Zacoalco rift to be dominantly right-lateral strike-slip. However, although only 1 mm/yr of pure right-lateral strike-slip is allowed in our velocity diagram analysis (Figure 2), the Tepic-Zacoalco rift is comprised of many faults with a range of orientations (N56°W being the overall orientation of the rift), the more E–W oriented of which may have slightly more pure right-lateral strike-slip motion. The second and third hypotheses for Jalisco Block motion, either some opening at both rifts due to tearing of the subducted slab or no current Jalisco Block motion with respect to North America, are both consistent with our upper limit of 8 mm/yr opening across the Tepic-Zacoalco and Colima rifts, and the lower limit of only very slow motion across these boundaries (within the 95% confidence interval). These constraints confirm that relative motion between the Jalisco Block and North America (if present) is small compared to relative rates of motion at nearby plate boundaries [e.g., *Bandy and Pardo, 1994*], and is consistent with Quaternary geology.

With respect to earthquake cycle behavior of subduction megathrusts, we see station velocities following the 1995 earthquake that are largely consistent with modeled interseismic station velocities, suggesting homogenous response of the overriding North America plate and rapid resumption of coupling on the subduction interface. This indication of homogeneous earthquake cycle deformation onshore from the Rivera plate is in contrast to the heterogeneous response to earthquakes beneath Oaxaca to the south [*Correa-Mora et al., 2008*], and suggests the Jalisco area as a promising location for better understanding earthquake cycle behavior.

Acknowledgments

We would like to thank Jeff Genrich and Tom Herring for helpful discussions. Support for this research was provided by National Science Foundation grants EAR-0510395 (J. Stock) and EAR-0510553 (C. DeMets).

Appendix I: Methods

Data are processed using the software packages GAMIT and GLOBK, developed at the Massachusetts Institute of Technology by T. A. Herring and D. Dong [*Herring et al., 1990; Feigl et al., 1993; Zumberge et al., 1997; Dong et al., 1998*]. Inputs into GAMIT are the data files, session specifications (year and day, receiver and antenna types, and antenna heights), and good initial station coordinates. Outputs are the loosely constrained solution files, which are passed to GLOBK for multi-session processing. A least-squares analysis is used to obtain the GAMIT solution files, and a combination of well-defined reference frame and Kalman filter with white noise are used in GLOBK to obtain the station coordinate time series and velocities.

The recursive, time-domain Kalman filter (run eight times) estimates the state of a dynamic system from a series of incomplete and noisy measurements, such as campaign GPS data [*Mao et al., 1999*]; only the previous time step and the current measurement are needed to estimate the current state, with a linear relation used in the calculation, making it computationally efficient [*Herring et al., 1990*]. The Kalman filter uses a multivariate normal distribution for the process noise, which is independent of past process noise for every time step (i.e., the Markov process). In the simplest case, the Markov process allows separate noise levels for the north, east, and vertical components of position (we use 2 mm/yr in the horizontal directions, 5 mm/yr in the vertical direction).

The same *a priori* position and velocity constraints for each station are used in GAMIT and GLOBK, and are obtained from standard ITRF2000 files for the North America reference stations, and from the online Scripps Coordinate Update Tool for the campaign stations. Rotation and translation of three components of position and their rates are permitted when determining the reference frame in GLOBK. We iterate the reference frame solution eight times in order to stabilize the coordinate system, with 75% weighting on the coordinate sigmas of the previous iteration, and a 4-sigma cutoff for sites that are discordant with *a priori* values. Height residuals allowed in the stabilization are limited to 5 mm between the best and median for position (and 5 mm/yr for the related rate), and 3 mm for the rms position (and 3 mm/yr for the related rate).

Earth orientation parameters are tightly constrained in GLOBK by Markov process values of 0.25 mas/day in orientation and 0.1 mas/day in its rate of change. Since final orbits are used, *a priori* GPS satellite orbital parameters are also tightly constrained, with correspondingly tightly constrained random walk variation allowed while processing multiple sessions. Changes to orbital parameters due to random noise are constrained to 10 cm/day in XYZ, 0.01 mm/s/day for the XYZ time derivatives, 1%/day in direct and y-bias nongravitational parameters, 0.1%/day in b-axis bias and once-per-rev parameters, and 1 cm/day for SV antenna offsets.

Appendix II: Results

Table 3.1. Global (North America (NA)) and campaign GPS sites, their velocity components and 1σ errors (relative to North America, as defined by the stations with a *), and the cross-correlation (ρ) between north (N) and east (E) rates (in mm/yr). Uncertainties on vertical rates (H, in mm/yr) are too large to constrain that component of motion. Stations are ordered by longitude.

Long. (deg)	Lat.	E rate (mm/yr)	N rate	E σ	N σ	ρ	H rate	H σ	Site
284.912	38.777	0.06	0.44	1.29	1.14	0.028	-3.48	1.79	CHL1*
284.476	39.160	-0.07	0.61	1.97	1.80	0.042	1.05	4.13	DNRC*
284.430	39.561	-0.12	0.79	1.58	1.43	0.055	-1.17	2.27	RED1*
284.430	39.562	-2.99	-1.41	3.55	3.49	0.004	-3.57	10.83	RED2*
280.157	32.758	-0.04	0.75	1.19	1.14	-0.024	0.32	1.40	CHA1*
278.347	24.582	-0.69	0.59	1.15	1.18	0.031	3.96	1.48	KYW1*
273.910	36.358	1.59	-1.15	1.72	1.68	0.005	-0.25	2.50	HTV1*
265.183	35.367	1.28	-1.71	1.17	1.12	0.012	0.49	1.35	SAL1*
264.598	39.126	-0.02	-0.08	1.18	1.13	-0.005	-1.47	1.46	KAN1*
264.089	41.778	1.66	-1.02	1.62	1.57	-0.012	4.54	2.68	OMH1*

262.244	30.312	-0.24	0.75	1.22	1.16	0.070	-4.07	1.65	AUS5*
257.685	31.874	-0.88	0.09	1.25	1.12	0.098	-1.62	1.72	ODS5*
256.839	20.090	-5.30	-0.85	1.89	1.67	0.023	-2.09	4.02	CEBO
256.675	20.293	-6.79	-0.57	1.89	1.67	0.018	2.71	3.88	COS2
256.650	20.694	-4.66	-5.11	2.97	2.73	0.017	2.52	7.87	UGEO
256.554	19.730	-3.83	-0.57	2.05	1.80	0.031	0.87	4.68	CGUZ
256.547	20.737	-8.48	-2.98	3.99	3.39	0.027	4.38	12.83	UMON
256.472	20.335	-6.67	-2.03	2.02	1.75	0.030	3.99	5.09	LIM2
256.203	19.831	-7.42	-3.91	2.03	1.75	0.030	-4.29	4.50	TAPA
255.985	30.681	-1.94	0.13	1.43	1.37	0.006	0.97	1.73	MDO1
255.702	19.064	7.10	7.43	5.90	4.67	0.030	-8.17	15.94	MANZ
255.671	19.748	-6.62	-5.18	1.97	1.72	0.018	2.05	4.04	AUTA
255.667	19.031	0.19	4.60	1.95	1.71	0.017	62.74	3.67	CRIP
255.626	20.188	-6.19	-4.78	1.94	1.71	0.015	17.50	3.93	AYUT
255.363	19.665	-5.50	-4.28	1.98	1.74	0.016	12.42	4.09	PURI

251.881	34.302	-1.35	-2.36	1.45	1.43	0.019	0.01	1.91	PIE1
249.028	32.224	-1.51	0.48	2.49	2.01	0.162	3.42	4.48	COT1*

Table 3.2. GPS sites in the Jalisco region, their velocity components 1σ errors (calculated relative to North America, as defined in Table 1, and presented relative to TAPA, a campaign site on the Jalisco Block), and the cross-correlation (ρ) between N and E rates (in mm/yr. Uncertainties on vertical rates (H, in mm/yr) are too large to constrain that component of motion. UGEO, CRIP, and MANZ are continuous sites, while all other stations are part of the campaign. Stations are ordered by longitude.

Long. (deg)	Lat.	E rate (mm/yr)	N rate	E σ	N σ	ρ	H rate	H σ	Site
256.203	19.831	0	0	0	0	0	0	0	TAPA
256.839	20.090	2.12	3.06	2.13	1.95	0.028	2.20	5.21	CEBO
256.675	20.293	0.63	3.34	2.13	1.96	0.026	7.00	5.10	COS2
256.650	20.694	2.75	-1.20	3.14	2.92	0.018	6.81	8.56	UGEO
256.554	19.730	3.58	3.35	2.21	2.03	0.031	5.17	5.38	CGUZ
256.547	20.737	-1.06	0.94	4.11	3.53	0.032	8.67	13.18	UMON
256.472	20.335	0.74	1.89	2.23	2.02	0.034	8.28	6.04	LIM2
255.702	19.064	14.52	11.35	5.96	4.76	0.030	-3.87	16.33	MANZ
255.671	19.748	0.80	-1.27	2.16	1.98	0.028	6.34	5.15	AUTA
255.667	19.031	7.61	8.52	2.11	1.95	0.025	67.03	4.78	CRIP
255.626	20.188	1.23	-0.87	2.14	1.97	0.025	21.79	5.05	AYUT

255.363	19.665	1.92	-0.37	2.16	1.99	0.027	16.71	5.18	PURI

Appendix III: Assumptions used in triple junction constraints

We assume a simplified geometry: three blocks (the Jalisco Block (JB), North America (NA), and the Michoacan Block (MB) [e.g., *Johnson and Harrison, 1990*]) meet at a continental triple junction formed by the Tepic-Zacoalco rift, the northern Colima rift, and the Chapala rift. GPS sites UGEO and UMON are on NA; GPS sites CEBO and CGUZ are on the MB; and GPS site TAPA is on block JB. We assume a flat-earth geometry because of the close spacing of these stations (<100 km separation). We use the results from Appendix II, Table 2 to constrain the velocity of NA and the MB relative to the JB, assuming no compression across any of the boundaries, as follows.

1. UGEO and UMON lie on NA, and should move together with respect to TAPA. The velocity of NA thus must lie within the intersection of the 95% confidence limits of the UMON and UGEO velocities relative to TAPA (red region in velocity diagram in Figure 2b). Similarly, velocity of the MB must lie within the intersection of the 95% confidence regions of the CEBO and CGUZ velocities.

2. We assume no compression across the Tepic-Zacoalco rift, which trends N56°W. Therefore the velocity of NA with respect to TAPA must lie northeast of a line with an azimuth of N56°W. This confines the allowable velocities for NA to points within the region shown in red in Figure 2c.

3. We assume no compression in the northern Colima rift, which trends N–S. Thus, the velocities of stations on the MB (CEBO and CGUZ) must lie east of a line trending N–S from the origin. This requires their velocities to lie within the green region shown in Figure 2d.

4. We assume no compression across the E–W trending Chapala rift. This eliminates velocities of NA from Figure 2c that lie south of the southernmost point in the green velocity field in Figure. 2d, yielding the possible velocities of NA relative to block JB, shown in red in Figure 2e. Similarly, we eliminate velocities of stations CGUZ and CEBO from Fig. 2d that lie north of an E–W line that passes through the northernmost point of the allowed velocity field for NA in Figure 2e. The velocity for the MB then is restricted to the green field of Figure 2f.

This yields the following constraints on the velocity triangle at the Guadalajara triple junction. At 95% confidence, the velocity of NA relative to the JB can lie anywhere in the red shaded region of Figure 2e. The velocity of the MB relative to the JB can lie anywhere in the green-shaded region on Figure 2f. However, the combination of velocities (one point from the red field and one point from the green field) must further satisfy two additional constraints. First, the red point cannot lie south of the green one (otherwise there would be compression across the Chapala rift). Second, the points on the velocity triangle must have the same topology as the blocks in map view; i.e., the JB, NA, and the MB must be encountered in clockwise order going around the triangle. A velocity triangle with the JB, NA, and the MB in counterclockwise order would imply that at least one of the boundaries is compressional.

References

Allan, J. F. (1986), Geology of the Northern Colima and Zacoalco Grabens, southwest Mexico: Late Cenozoic rifting in the Mexican Volcanic Belt, *Geol. Soc. of Am. Bull. 97*, 473 – 485.

Allan, J. F., S. A Nelson, J. F. Luhr, I. S. E. Carmichael, M. Wopat, and P. J. Wallace (1991), Pliocene-Holocene Rifting and Associated Volcanism in Southwest Mexico: An Exotic Terrane in the Making, *in* Dauphin, J. P. & Simoneit, B. R. T., eds., The Gulf and Peninsular Province of the Californias: Boulder, Colorado, *AAPG Memoir 47*, 425 – 445.

Altamimi, Z., P. Sillard, and C. Boucher (2002), ITRF2000: A new release of the International Terrestrial Reference Frame for earth science applications*, J. of Geophys. Res., 107*(B10), 2214, doi:10.1029/2001JB000561.

Andrews, V., J. M. Stock, G. Reyes-Dávila and C. Ramírez-Vazquez (2010), Double-difference relocation of the aftershocks of the Tecomán, Colima, Mexico earthquake of 22 January 2003, *PAGEOPH*, doi:10.1007s0024-010-023-0.

Arzate, J. A., R. Alvarez, V. Yutsis, J. Pacheco, and H. Lopez-Loera (2006), Geophysical modeling of Valle de Banderas Graben and its structural relation to Bahia de Banderas, Mexico, *Revista Mexicana de Ciencias Geologicas 23* (2), 184 – 198.

Bandy, W. and M. Pardo (1994), Statistical examination of the existence and relative motion of the Jalisco and Southern Mexico Blocks, *Tectonics 13* (4), 755 – 768.

Bandy, B. L., F. Michaud, J. Bourgois, T. Calmus, J. Dyment, C. A. Mortera-Gutierrez, J. Ortega-Ramirez, B. Pontoise, J.-Y. Royer, B. Sichler, M. Sosson, M. Rebolledo-Vieyra, F. Bigot-Cormier, O. Diaz-Molina, A. D. Hurtado-Artunduaga, G. Pardo-Castro, C. Trouillard-Perrot (2005), Subsidence and strike-slip tectonism of the upper continental slope off Manzanillo, Mexico, *Tectonophysics 398*, 115 – 140.

Becker, J. J. and D. T. Sandwell (2006), SRTM30_PLUS V2.0: Data fusion of SRTM land topography with measured and estimated seafloor topography, 29 July 2006, ftp://edcsgs9.cr.usgs.gov/pub/data/srtm/SRTM30.

Bourgois, J., V. Renard, J. Aubouin, W. Bandy, E. Barrier, T. Calmus, J.-L. Carfantan, J. Guerrero, J. Mammerickx, B. Mercier de Lepinay, F. Michaud, M. Sosson (1988), Active fragmentation of the North American Plate: Offshore boundary of the Jalisco Block off Manzanillo, *C. R. Acad., Sci. Paris 307* (II), 1121 – 1130.

Correa-Mora, F., C. DeMets, E. Cabral-Cano, B. Marquez-Azua, and O. Diaz-Molina (2008), Interplate coupling and transient slip along the subduction interface beneath Oaxaca, Mexico, *Geophys. J. Int. 175*, 269 – 290.

DeMets, C. and D. S. Wilson (1997), Relative motions of the Pacific, Rivera, North American, and Cocos plates since 0.78 Ma, *J. of Geophys. Res. 102* (B2), 2789 – 2896.

DeMets, C. and S. Traylen (2000), Motion of the Rivera plate since 10 Ma relative to the Pacific and North American plates and the mantle, *Tectonophysics 318*, 119 – 159.

Dong, D., T. A. Herring, and R. W. King (1998), Estimating regional deformation from a combination of space and terrestrial geodetic data, *J. of Geodesy 72*, 200 –214.

Feigl, K. L., D. C. Agnew, Y. Bock, D. Dong, A. Donnellan, B. H. Hager, T. A. Herring, D. D. Jackson, T. H. Jordan, R. W. King, S. Larsen, K. M. Larson, M. H. Murray, Z. Shen, and F. H. Webb (1993), Space Geodetic Measurement of Crustal Deformation in Central and Southern California, 1984 – 1992, *J. of Geophys. Res. 98* (B12), 21,677 – 21,712.

Ferrari, L. (1995), Miocene shearing along the northern boundary of the Jalisco block and the opening of the southern Gulf of California, *Geology 23* (8), 751 – 754.

Ferrari, L. (2004), Slab detachment control on mafic volcanic pulse and mantle heterogeneity in central Mexico, *Geology 32* (1), 77 – 80.

Ferrari, L. and J. Rosas-Elguera (2000), Late Miocene to Quaternary extension at the northern boundary of the Jalisco block, western Mexico: The Tepic-Zacoalco rift revised, *in* Delgado-Granados, H., G. Aguirre, and J. M. Stock, eds., Cenozioc Tectonics and Volcanism of Mexico: Boulder, Colorado, *GSA Special Paper 334*, 41 – 63.

Ferrari, L., G. Pasquare, S. Venegas, D. Castillo, and F. Romero (1994), Regional tectonics of western Mexico and its implications for the northern boundary of the Jalisco Block, *Geofisica Internacional 33* (1), 139 – 151.

Frey, H. M., R. A. Lange, C. M. Hall, H. Delgado-Granados, I. S. E. Carmichael (2007), A Pliocene ignimbrite flare-up along the Tepic-Zacoalco rift: Evidence for the initial stages of rifting between the Jalisco block (Mexico) and North America*, GSA Bulletin 119* (1/2), 49 – 64.

Garduño-Monroy, V. H., R. Saucedo-Girón, Z. Jiménez, J. C. Gavilanes-Ruiz, A. Cortés-Cortés, and R. M. Uribe-Cifuentes (1998), La falla Tamazula, Límite suroriental del Bloque Jalisco, y sus relaciones con el complejo volcánico de Colima, México, *Rev. Mex. Cienc. Geol. 15*, 132 – 144.

Grand, S. P., T. Yang, S. Suhardja, D. Wilson, M. G. Speziale, J. Gomez Gonzalez, G. Leon-Soto, J. Ni, and T. Dominguez Reyes (2007), Seismic structure of the Rivera subduction zone – the MARS experiment (abstract), *Eos, Trans., AGU* , T32A-02.

Herring, T. A., J. L. Davis, and I. I. Shapiro (1990), Geodesy by Radio Interferometry: The Application of Kalman Filtering to the Analysis of Very Long Baseline Interferometry Data, *J. of Geophys. Res. 95* (B8), 12,561 – 12,581.

Hutton, W., C. DeMets, O. Sanchez, G. Suarez, and J. Stock (2001), Slip kinematics and dynamics during and after the 1995 October 9 M_w = 8.0 Colima-Jalisco earthquake, Mexico, from GPS geodetic constraints, *Geophys. J. Int. 146*, 637 – 658.

Johnson, C. A. and C. G. A. Harrison (1990), Neotectonics in central Mexico, *Physics of the Earth and Planetary Interiors 64*, 187 – 210.

Khutorskoy, M. D., L. A. Delgado-Argote, R. Fernandez, V. I. Kononov, B. G. Polyak (1994), Tectonics of the offshore Manzanillo and Tecpan basins, Mexican Pacific, from heat flow, bathymetric and seismic data, *Geofis. Int. 33*, 161 – 185.

Kostoglodov, V. and W. Bandy (1995), Seismotectonic constraints on the convergence rate between the Rivera and North American plates, *J. of Geophys. Res*. 100 (B9), 17,977 – 17,989.

Luhr, J. F., S. A. Nelson, J. F. Allan, and I. S. E. Carmichael (1985), Active rifting in southwestern Mexico: Manifestations of an incipient eastward spreading-ridge jump, *Geology 13*, 54 – 57.

Mao, A., C. G. A. Harrison, and T. H. Dixon (1999), Noise in GPS coordinate time series, *J. of Geophys. Res. 104* (B2), 2797 – 2816.

Marquez-Azua, B. M. and C. DeMets (2003), Crustal velocity field of Mexico from continuous GPS measurements, 1993 to June 2001: Implications for the neotectonics of Mexico, *J. of Geophys. Res. 108* (B9), 2450, doi:10.1029/2002/2002JB002241.

Marquez-Azua, B. M. and C. DeMets (2009), Deformation of Mexico from continuous GPS from 1993 to 2008, *Geochem. Geophys. Geosyst. 10,* Q02003, doi:10.1029/2008GC002278.

Marquez-Azua, B. M., C. DeMets, and T. Masterlark (2002), Strong interseismic coupling, fault afterslip, and viscoelastic flow before and after the Oct. 9, 1995 Colima-Jalisco earthquake: Continuous GPS measurements from Colima, Mexico; *Geophysical Research Letters 29* (N.8), 122-1 – 122-4.

Masterlark, T., C. DeMets, H. F. Wang, J. Stock, and O. Sanchez (2001), Homogeneous vs. heterogeneous subduction zone models: Coseismic and postseismic deformation, *Geophysical Review Letters 28*, 4047 – 4050.

Melbourne, T., I. Carmichael, C. DeMets, K. Hudnut, O. Sanchez, J. Stock, G. Suarez, F. Webb (1997), The geodetic signature of the M8.0 Oct. 9, 1995, Jalisco subduction earthquake, *Geophys. Res. Let. 24* (6), 715 – 718.

Melbourne, T., F. Webb, J. Stock, and C. Reigber (2002), Rapid postseismic transients in subduction zones from continuous GPS, *J. Geophys. Res. 107* (B10), 2241, doi:10.1029/20001JB000555.

Molnar, P. and J. M. Stock (1985), A method for bounding uncertainties in combined plate reconstructions, *J. of Geophys. Res. 90* (B14), 13537 – 12544.

Nixon, G. T. (1982), The relationship between Quaternary volcanism in central Mexico and the seismicity and structure of subducted ocean lithosphere, *Geol. Soc. of Am. Bull. 93*, 514 – 523.

Nuñez-Cornú, F. J., R. L. Marta, F. A. Nava-P., G. Reyes-Davila, and C. Suarez-Plascencia (2002), Characteristics of seismicity in the coast and north of Jalisco Block, Mexico, *Phys. of the Earth and Planet. Int. 132*, 141-155.

Pacheco, J. F., S. K. Singh, J. Dominguez, A. Hurtado, L. Quintanar, Z. Jimenez, J. Yamamoto, C. Gutierrez, M. Santoyo, W. Bandy, M. Guzman, V. Kostoglodov (1997), The October 9, 1995 Colima-Jalisco, Mexico earthquake (M_W 8): An aftershock study and a comparison of this earthquake with those of 1932, *Geophys. Res. Let. 24* (17), 2223 – 2226.

Pacheco, J. F., C. A. Mortera-Gutierrez, H. Delgado, S. K. Singh, R. W. Valenzuela, N. M. Shapiro, M. A. Santoyo, A. Hurtado, R. Barron, and E. Gutierrez-Moguel (1999), Tectonic

significance of an earthquake sequence in the Zacoalco half-graben, Jalisco, Mexico, *Journal of South American Earth Sciences 12*, 557 – 565.

Pacheco, J., W. Bandy, G. A. Reyes-Davila, F. J. Nuñez-Cornú, C. A. Ramirez-Vazquez, J. R. Barron (2003), The Colima, Mexico, earthquake (Mw 5.3) of 7 March 2000: Seismic activity along the southern Colima rift, *Bull. Seismol. Soc. Am. 93*, 1458 – 1476.

Pardo, M. and G. Suarez (1995), Shape of the subducted Rivera and Cocos plates in southern Mexico: Seismic and tectonic implications*, J. of Geophys. Res. 100* (B7), 12,357 – 12,373.

Rosas-Elguera, J., L. Ferrari, V. H. Garduño-Monroy, J. Urrutia-Fucugauchi (1996), Continental boundaries of the Jalisco block and their influence in the Pliocene-Quaternary kinematics of western Mexico, *Geology 24* (10), 921 – 924.

Rosas-Elguera, J., L. Ferrari, M. Martinez, J. Urritia-Fucagauchi (1997), Stratigraphy and Tectonics of the Guadalajara Region and Triple-Junction Area, Western Mexico, *International Geology Review 39*, 125 – 140.

Schmitt, S. V., C. DeMets, J. Stock, O. Sanchez, B. Marquez-Azua, and G. Reyes (2007), A geodetic study of the 2003 January 22 Tecomán, Colima, Mexico earthquake, *Geophys. J. Int. 169*, 389 – 406.

Singh, S. K., L. Ponce, S. P. Nishenko (1985), The great Jalisco, Mexico, earthquakes of 1932: Subduction of the Rivera plate, *Bull. Seis. Soc. Am. 75* (5), 1301 – 1313.

Stock, J. M. (1993), Tectónica de placas y la evolución del bloque Jalisco, México, *GEOS, Bol. Mex Geofis. Union 13* (3), 3 – 9.

Suarez, G., V. Garcia-Acosta, and R. Gaulon (1994), Active crustal deformation in the Jalisco block, Mexico: evidence for a great historical earthquake in the 16th century, *Tectonophysics, 234*, 117 – 127.

Suhardja, S., S. Grand, D. Wilson, M. Guzman Speziale, J. Gomez Gonzalez, J. Ni, and T. Dominguez Reyes (2007), Crustal structure beneath Southwestern Mexico (abstract), *Eos, Trans., AGU*, S33A-1052.

Urrutia-Fucugauchi, J. and T. Gonzalez-Moran (2006), Structural pattern at the northwestern sector of the Tepic-Zacoalco rift and tectonic implications for the Jalisco block, western Mexico, *Earth Planets Space 58*, 1303 – 1308.

Wang, K. (2007), Elastic and viscoelastic models of crustal deformation in subduction earthquake cycles, in *The Seismogenic Zone of Subduction Thrust Faults*, eds. T. H. Dixon and J. C. Moore, 540 – 575.

Wang, X., F. Niu, J. Ni, and S. Grand (2008), Crustal and Mantle Structure of the Jalisco Block of western Mexico from Surface Wave Tomography (abstract), *Eos, Trans., AGU*, S23A-1871.

Yagi, Y., Mikumo, T., Pachecho, J., and Reyes, G. (2004), Source Rupture Process of the Tecomán, Colima, Mexico Earthquake of 22 January 2003, Determined by Joint Inversion of Teleseismic Body-Wave and Near-Source Data, *Bull. Seism. Soc. Am. 94*, 1795-1807.

Yang, T., S. P. Grand, D. Wilson, M. Guzman-Speziale, J. M. Gomez-Gonzalez, T. Dominguez-Reyes, and J. Ni (2009), Seismic structure beneath the Rivera subduction zone from finite-frequency seismic tomography, *J. Geophys. Res. 114*, B01302, doi:10.1029/2008JB005830.

Zumberge, J. F., M. B. Heflin, D. C. Jefferson, M. M. Watkins, and F. H. Webb (1997), Precise point positioning for the efficient and robust analysis of GPS data from large networks, *J. of Geophys. Res. 102* (B3), 5005 – 5017.

Chapter 4

USING OVERLAPPING SONOBUOY DATA FROM THE ROSS SEA TO CONSTRUCT A 2D DEEP CRUSTAL VELOCITY MODEL[3]

Sonobuoys provide an alternative to using long streamers while conducting multi-channel seismic (MCS) studies, in order to provide deeper velocity control. In contrast to ocean-bottom seismometers, they are less expensive to acquire and deploy, and return data in real time. We present analysis and modeling techniques for interpreting the sonobuoy data and illustrate the method with ten overlapping sonobuoys collected in the Ross Sea, offshore from Antarctica. We demonstrate the importance of using the MCS data to correct for ocean currents and changes in ship navigation, which is required before using standard methods for obtaining a 1D velocity profile from each sonobuoy. We confirm the accuracy of our 1D velocity models using finite-difference (FD) method modeling and performing depth migration on the data, and demonstrate the usefulness of FD modeling for tying true velocities to the shallow crustal structure imaged using MCS data. Finally, we show how overlapping sonobuoys along an MCS line can be used to construct a 2D velocity model of the crust. The velocity model reveals a thin crust at the boundary between the Adare and Northern Basins, and implies that the crustal structure of the Northern Basin may be more similar to that of the oceanic crust in the Adare Basin, rather than to the stretched continental crust further south in the Ross Sea.

---

[3] This research was conducted in collaboration with R. Clayton (Seismological Laboratory, Caltech), R. Granot (Institute de Physique du Globe de Paris), and J. M. Stock (Seismological Laboratory, Caltech), and will be submitted to *Marine Geophysical Researches* for publication.

Introduction

Using sonobuoys to investigate deep crustal structure

Sonobuoys provide a means of obtaining long offsets for deep velocity analysis, while conducting multi-channel seismic (MCS) studies. They are preferable to using a long streamer in locations with difficult open water conditions, such as in the Ross Sea and Southern Ocean, where research cruises regularly encounter sea ice, icebergs, and intense storms. Ocean-bottom seismometers (OBS) provide another method for collecting active seismic data with large offsets, but are more expensive than sonobuoys and are challenging to recover in the conditions described above. Sonobuoys are also an ideal method for collecting large offset seismic data in other settings where ship navigation is constrained, such as locations with ship traffic and narrow bodies of water like fjords.

We present techniques for interpreting deep crustal structure from overlapping sonobuoy data collected in the northwestern Ross Sea. We first demonstrate the necessity and method for correcting for the effect of current and changes in ship navigation, prior to using standard processing techniques to obtain 1D velocity models from the sonobuoys. Second, we explore the benefits of using finite-difference (FD) method modeling of sonobuoys to tie true velocities to the shallow crustal structure imaged with MCS data. Finally, we apply these methods to a set of ten overlapping sonobuoys in order to construct a 2D velocity model of the deeper crustal structure along one of the MCS lines.

Modeling methods for seismic refraction data

Ray tracing can model seismic travel times in fairly complicated subsurface structure, and a comparison of ray tracing models to seismic refraction data is one way to identify structure in the crust. However, ray tracing has difficulty in predicting the amplitudes and consequently it is often difficult to judge the importance of some of the predicted arrivals. Another computational method that provides similar results is FD modeling of wave propogation through the subsurface. This method can similarly model bent seismic waves, and their reflections and conversions at interfaces, for a complicated subsurface structure. One advantage of using the FD to model seismic refraction data is the ability to model the entire wave front from source to receiver, which allows us to both tie the shallow structure detected with MCS data to particular velocity horizons and determine the deeper crustal velocity structure.

Shipp and Singh [2002] use a 2D elastic finite-difference forward model and an interative full wavefield inversion scheme to best fit their streamer data (with a 12 km offset), solving for velocity structure down to 4 km below the seafloor. This approach is computationally demanding, with residuals from the comparison of data and the model being back propogated for every time step, which is why they are constrained to analysis of relatively shallow crust. Jones et al. [2007] perform a similar analysis on streamer data (with offsets of 15 and 18 km); they additionally derive 1D velocity models from the intercept-time-slowness (τ-p) domain, and downward continue the data in order to create an image of the layers at depth. They are able to image the velocity structure to a depth of 6 km.

In order to conduct a marine seismic refraction experiment with an offset larger than tens of kilometers, Ritzmann et al. [2004] used OBS instruments. They use a ray tracing model to reproduce the data, and find that crustal thickness varies widely, from 32 km for the continental crust of Svalbard to as little as 2 km (excluding the ~2 km of sediment on top of the basement) near the margin between continental and oceanic crust. Mantle velocities are generally >8.0 km/s, but are as low as 7.7 km/s under one ridge, where the mantle is likely serpentinized [*Ritzmann et al.*,

2004]. Also offshore from Svalbard, Geissler and Jokat [2004] used sonobuoy data as 1D velocity profile "pseudo-boreholes" along an MCS line, to obtain deeper crustal structure.

In this chapter, we combine the analysis of sonobuoy data in the τ-p domain with FD modeling of the waveform to derive a sequence of 1D velocity models, which are then interpreted into a 2D deep crustal velocity model.

Seismic data in the Ross Sea

We will illustrate the analysis procedure for sonobuoy data collected in the Adare Trough region of the Ross Sea, offshore from Antarctica. The Adare Trough, a dead mid-ocean spreading ridge, lies in the deep water of the Adare Basin and trends toward the Northern Basin, which is up on the continental shelf (Figure 1). The shallow structure is well imaged by MCS data [*Granot et al.*, 2010]. However, understanding the tectonics in the area requires knowledge of the deep velocity structure (see Chapter 4 for an analysis of all sonobuoy data, and implications for tectonics).

We collected seismic reflection and refraction data during research cruise NBP0701 on board the *R/V Nathaniel B. Palmer*. Sonobuoy data were collected in both basins, with maximum offsets from the ship of 20 – 30 km. Sonobuoys presented here were deployed with a regular spacing of ~15 km in shallow water (Figure 1 inset).

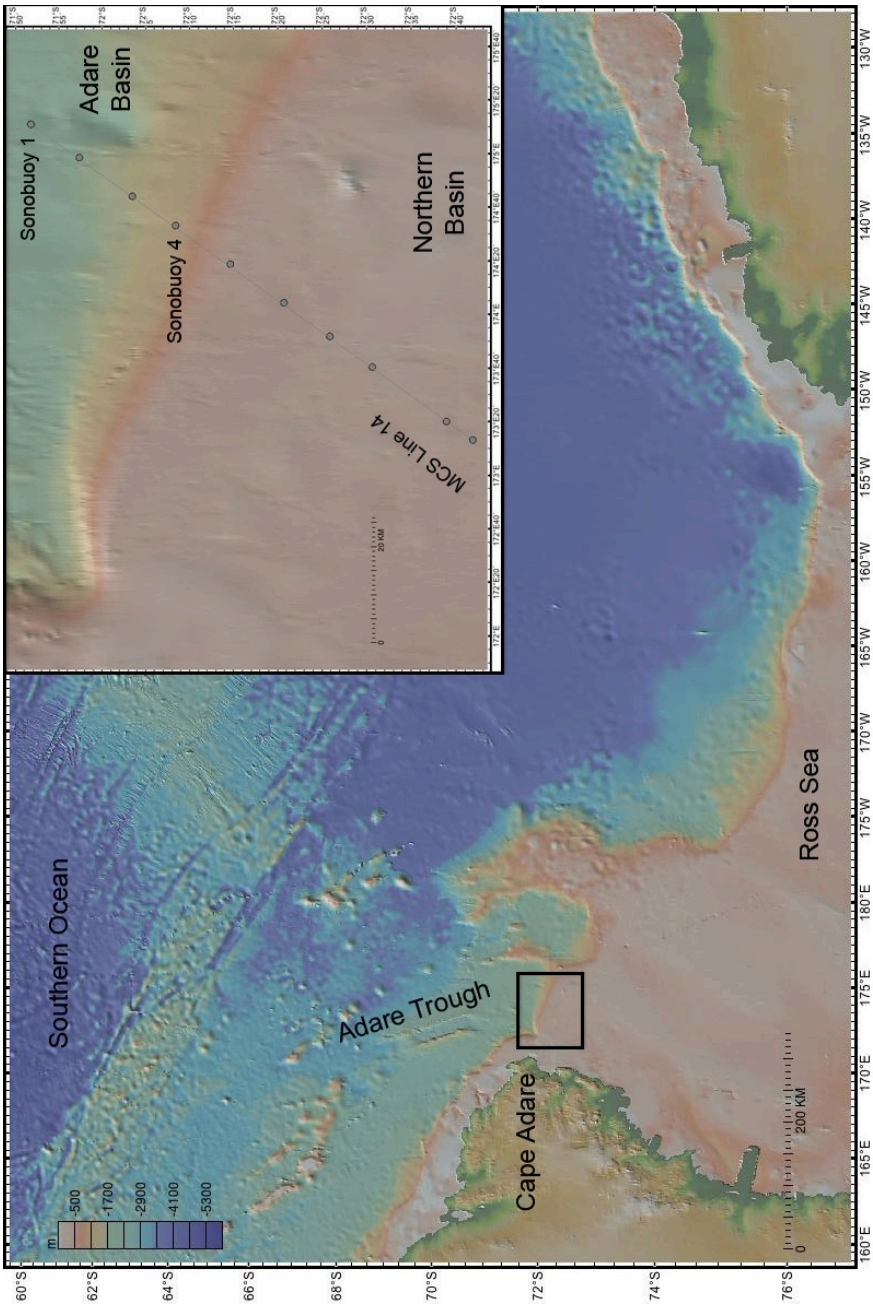

Figure 4.1. We interpret a subset of the active seismic data collected in the northwestern Ross Sea (indicated by the black box) during research cruise NBP0701, shown on top of the regional bathymetry (key in the upper left). As shown in the inset, ten sonobuoys are closely spaced along multi-channel seismic (MCS) Line 14, which runs from deep water in the Adare Basin onto the continental margin in the Northern Basin. This figure was made using GeoMapApp.

Most sonobuoy studies in the western Ross Sea have focused on Victoria Land Basin (Figure 1), and have used linear moveout and ray tracing methods to determine sediment velocity gradients and basement depth [*Cochrane et al.*, 1995; *Cooper et al.*, 1987; *Houtz and Davey*, 1973]. Ocean bottom seismic refraction studies have investigated the deeper crustal structure in the central and southern Ross Sea, using ray tracing and amplitude modeling methods [*Trehu et al.*, 1993; *Trey et al.*, 1999]. Crustal thickness, defined as the depth to velocities of >8000 m/s, is as little as 16 km beneath sedimentary basins underlain by thinned crust and magmatic intrusions, and 21 km beneath intervening basement highs [*Trey et al.*, 1999].

MCS data from NBP0701 contain resolvable primaries up to 2.2 seconds in travel time, in the deep-water conditions of the Adare Basin, revealing variable sediment thickness [*Granot et al.*, 2010]. Migrated MCS data delineate the structure and deformation of the sedimentary units in the Adare and Northern Basin, but cannot tie velocity values to the subsurface layers, and cannot detect crustal structure below the basement rock. FD modeling of the sonobuoy data allows for direct comparison of features in the MCS data with layers in the 1D velocity models.

Methods for sonobuoy analysis and interpretation

Trace spacing adjustment and construction of 1D velocity profiles

MCS data were collected using a 1 km, 48-channel streamer; this short streamer was required due to regular interactions with sea ice. Data presented here were obtained using a 6-element Bolt-gun array with a total capacity of 34.8 liters, with typical source spacing of approximately 40 m. We present data analysis methods, and results, for ten overlapping sonobuoy profiles along MCS Line 14, which ran from the deep water of the Adare Basin up onto the shallow-water shelf of the Northern Basin (see Figure 1).

These sonobuoys were deployed approximately every 15 km, and returned data for 20 – 30 km of offset. While the source moved away from the sonobuoy launch position at a nearly uniform speed and direction, sonobuoy drift after launch (due to ocean currents) and slight variations in ship navigation led to varying shot spacing in the refraction data set. We correct for these effects before analysis, modeling, and interpretation of the data. The sonobuoy data provide information on the deep crustal structure along the MCS line, and direct detection of layer velocities; MCS data are useful in determining the sound speed (seismic velocity) of the water layer and the shallowest of the rock layers.

We show the processing steps needed for accurate interpretation of the sonobuoy data, starting from the raw data for the deep-water Sonobuoy 1 (Figure 2a) and the shallower-water Sonobuoy 4 (Figure 2b). We highlight the low-frequency reflected and refracted energy from the seafloor and within the crust by applying a tapered band-pass filter to the data (set to 5, 15, 35, and 40 Hz). Several key features of the data are obvious in these sonobuoy images: (1) the direct wave, from source to receiver, is the first arrival at small offsets, (2) the reflection from the seafloor comes in after the direct wave for small offsets, and due to its strength as well as noise in the data no reflections from deeper layers are observed (subsequent reflections are seafloor multiples), (3) head waves, refracted energy from layer interfaces at depth, come in as first arrivals for larger offsets.

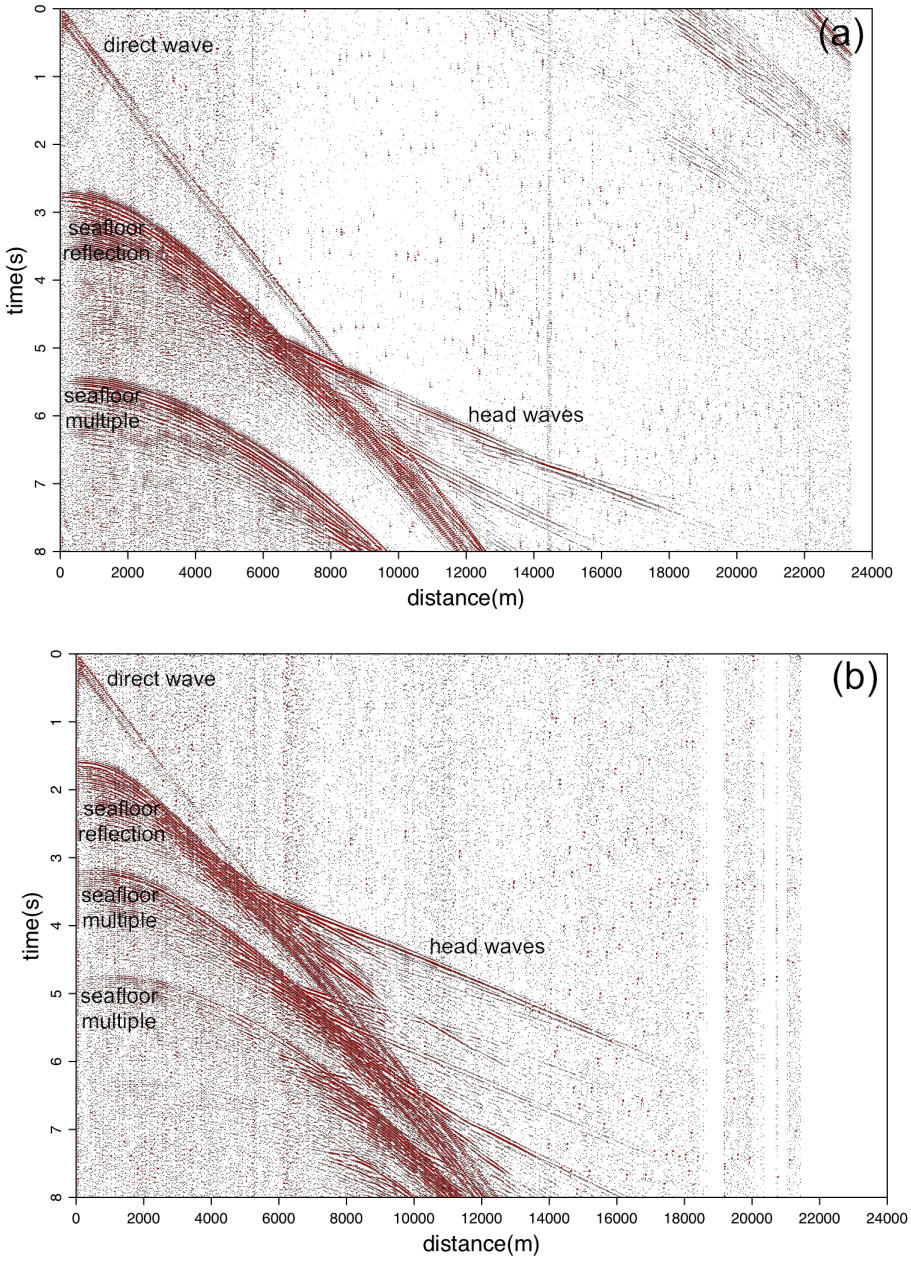

Figure 4.2. Raw data for Sonobuoys 1 (a) and 4 (b) on Line 14 show key features used to determine the 1D velocity profile at these locations. The direct arrival comes in first in time for smaller offsets, while energy from head waves traveling along layer interfaces at depth comes in first for larger offsets; the slopes of these linear features are determined by the interval velocities in the crust. The hyperbolic reflection off the seafloor comes in second for smaller offsets and provides a time constraint used to determine the water layer thickness. Later hyperbolic features are multiples of the seafloor reflection.

We correct sonobuoy shot spacing, so that the direct wave has a slope of 1450 m/s, as determined by applying a linear moveout to the direct wave in the MCS data. This value for the seismic velocity of the water layer is consistent along the MCS line, and is therefore taken as the default value for all sonobuoys; it is also consistent with measurements of sound speed in water taken during the cruise. Data from the one expendable sound velocimeter (XSV) show water velocities within 1441 – 1451 m/s (to 600 m depth), while expendable bathythermographs (XBTs, which measure temperature with depth and use surface measurements of salinity to compute sound velocity) show water velocities of 1444 – 1480 m/s at the northern end of MCS Line 14, and 1446 – 1448 m/s at the southern end of Line 14. Sensor measurements of sound speed in water (accurate to ±0.25 m/s) and values obtained from applying linear moveout to the MCS data for a single shot (accurate to ±50 m/s) agree within uncertainty.

In order to correct the shot spacing, we adjust the distance coordinate of each trace, such that the direct wave is linear and has the correct slope in the distance versus time plot. Making the correction by applying a stretch to each trace in the time dimension, based on the linear feature of the direct wave, would not properly correct features that are not linear, such as the hyperbolic seafloor reflection. The direct wave of Sonobuoy 1 is shown with a linear moveout applied before (Figure 3a, with a direct wave velocity of 1570 m/s) and after (Figure 3b, with a direct wave velocity of 1450 m/s) this correction is made; the adjustment for Sonobuoy 4 makes a similar direct wave velocity adjustment (Figure 3c, d). Other sonobuoys have larger discrepancies between the direct wave velocities before and after the correction (see Table 1). This correction will not be necessary for sonobuoys with reliable GPS; in that case, the sonobuoy location will be at least as well known as that of the MCS streamer.

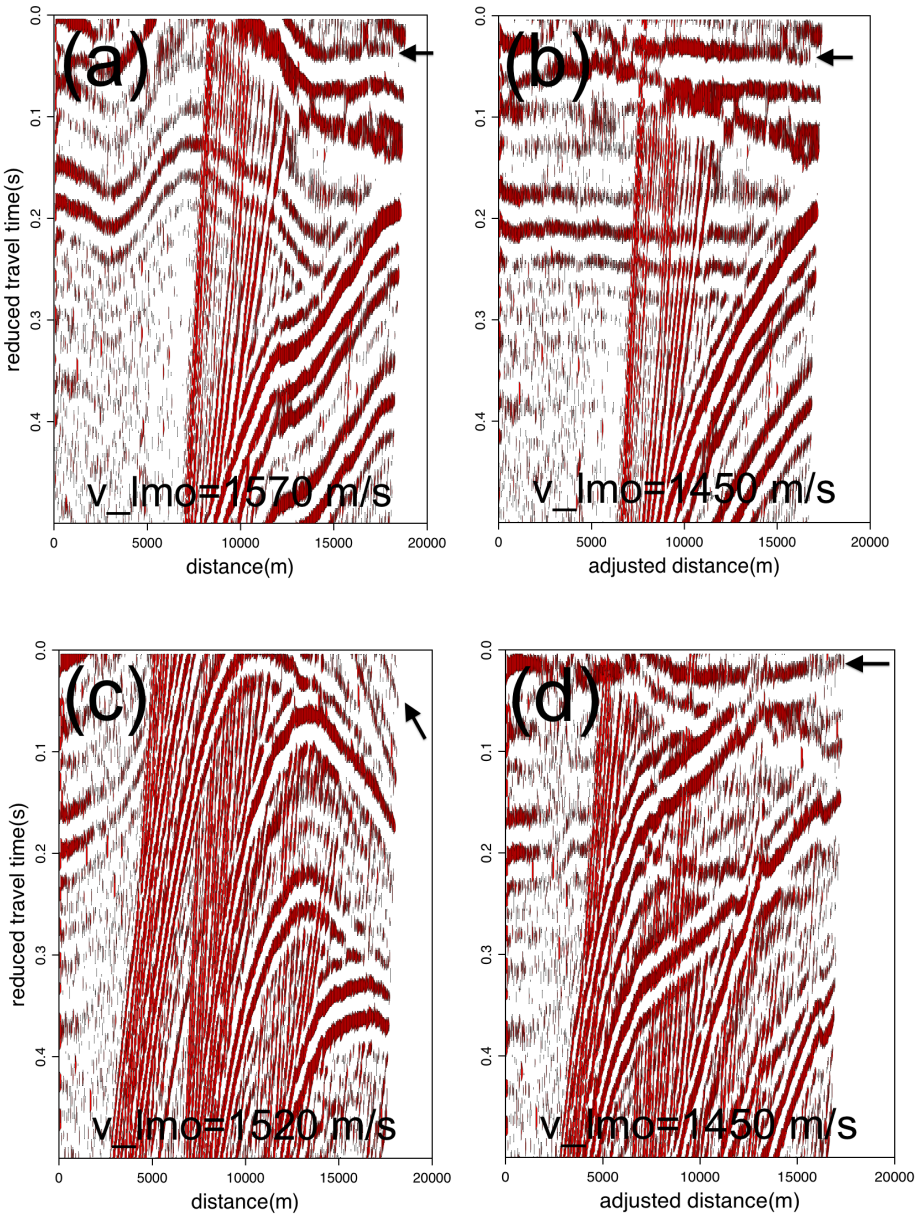

Figure 4.3. We correct the sonobuoy shot spacing to account for ocean currents and changes in ship navigation. A best possible linear moveout (lmo) of 1570 m/s is applied to the direct wave in the raw data for Sonobuoy 1 (a). The distances between shots are corrected (b), based on picks made along the direct wave, producing a linear direct wave with the correct water velocity of 1450 m/s (as determined from multi-channel seismic data). Sonobuoy 4 has a linear moveout of 1520 m/s before the correction (c), and 1450 m/s after (d). See Table 1 for direct wave velocities prior to the correction.

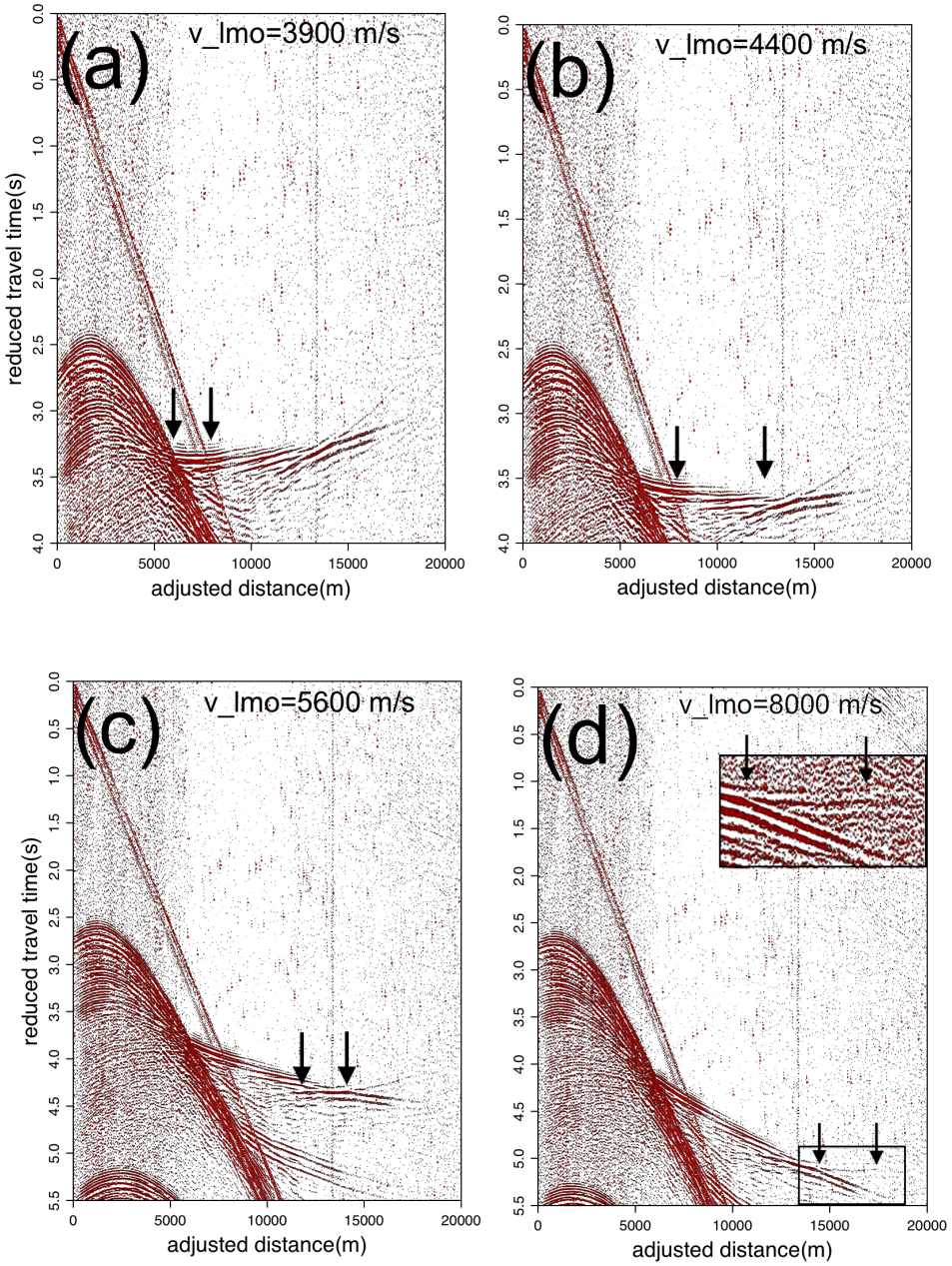

Figure 4.4. Linear moveout (lmo) is applied to the refracted energy in the distance-adjusted version of Sonobuoy 1, to directly measure interval velocities and associated times (τ). We detect layers with velocities of 3900 m/s (a), 4400 m/s (b), 5600 m/s (c), and 8000 m/s (d), with head waves lying within the arrows; the 8000 m/s layer is also shown as an inset. The latter value is the only instance of a velocity that can be interpreted as the Moho. Refracted energy from the seafloor is not observed (an interval velocity of 2200 m/s for the uppermost sediment layer is determined from multi-channel seismic data).

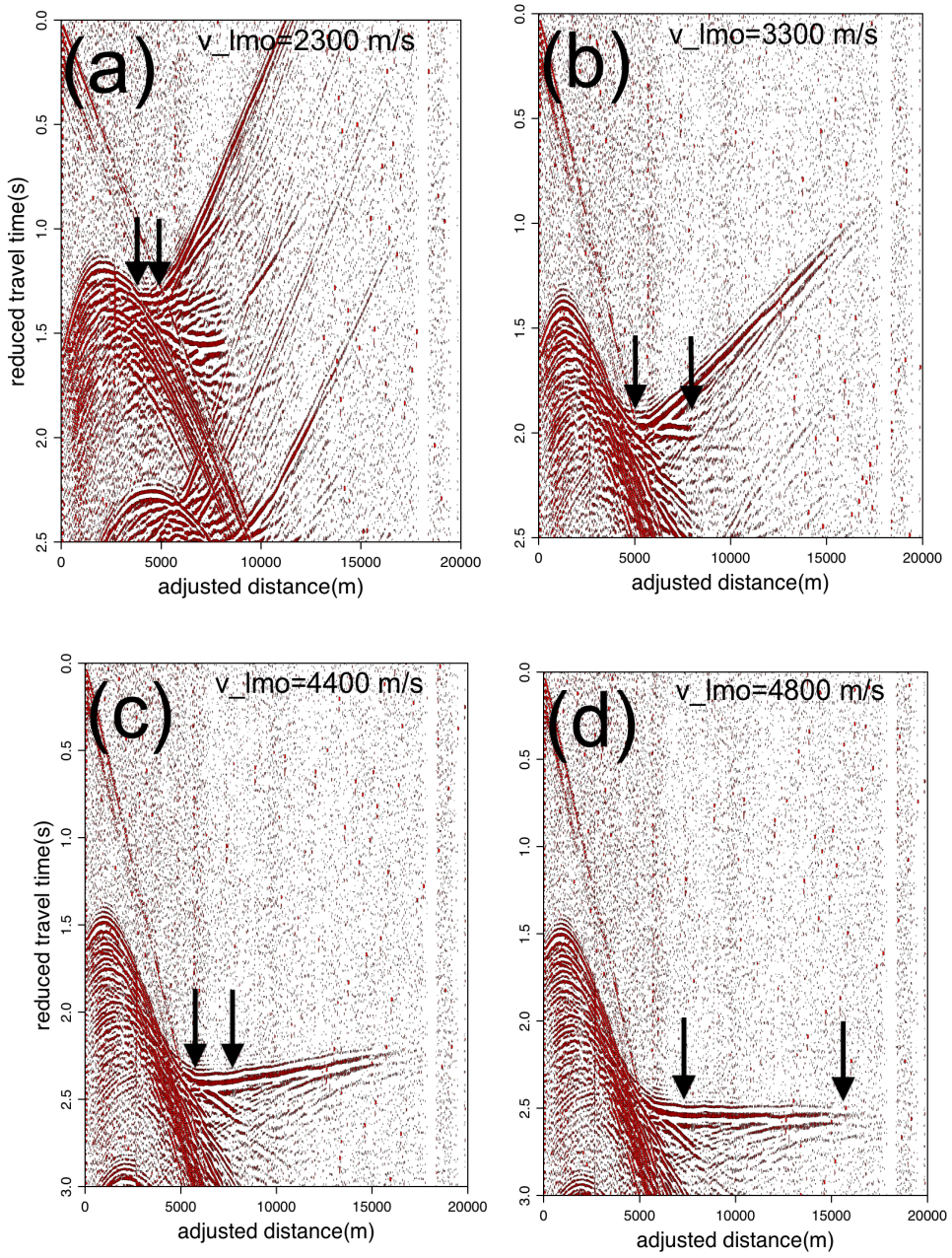

Figure 4.5. Linear moveout (lmo) is applied to the refracted energy in the stretch-corrected version of Sonobuoy 4, directly measuring interval velocities and their associated times. We detect layers with velocities of 2300 m/s (a), 3300 m/s (b), 4400 m/s (c), and 4800 m/s (d), with head waves lying within the arrows. Refracted energy from the seafloor is not observed (an interval velocity of 2000 m/s for the uppermost sediment layer is determined from multi-channel seismic data).

We directly detect layer velocities, and their associated times, by applying linear moveout to head waves in the corrected sonobuoy data. We detect between three and six distinct layers at depth for each sonobuoy with this method, as shown in detail for Sonobuoys 1 and 4 (Figures 4 and 5, respectively). This same approach yielded a consistent velocity of 2000 m/s for the shallowest rock layer in seven out of the ten sonobuoys; in other cases this seafloor head wave is not visible. Even when it is visible, it is usually brief (~10 traces) and so less distinct than most other refractors we measure. For this reason, we confirm this layer velocity by applying a normal moveout to the hyperbolic arrival of the seafloor reflection in the raw MCS data, and use it as the first rock layer velocity for all ten sonobuoys; one exception is Sonobuoy 1, where analysis of MCS data provides a first rock layer velocity of 2200 m/s. Layer velocities for all sonobuoys are listed in Table 2.

The velocities and their associated times are used to calculate the 1D velocity profile for each sonobuoy [e.g., *Fowler*, 1990, p. 119 - 123]. Water depth and first rock layer thickness are calculated using velocities (v) and reflection times (t) from the MCS data (i.e. $h_1 = 0.5(t_1)(v_1)$). Thicknesses of deeper layers are determined using standard seismic refraction analysis:

$$h_i = \frac{v_i}{2\cos(\theta_{i,i+1})}\left[\tau_{i-1} - \sum_{j=1}^{i-1}\frac{2h_j}{v_j}\cos(\theta_{j,i+1})\right],$$

where θ_{ab}=arcsin(v_a/v_b) and τ is the reduced travel time associated with the layer velocity, obtained when linear moveout is applied to the sonobuoy data. See the appendix for further details. A direct image of the τ-p curve can be obtained by a radon transform of the data [*McMechan and Ottolini*, 1980]; an example is shown in Figure 9.

Table 4.1. Direct wave velocities, as determined using a best possible linear moveout fit to the feature, are listed for Sonobuoys 1 – 10 (S1 – S10) on Line 14. The slope of the direct wave is corrected by adjusting the distance between traces, such that the sonobuoy data has the correct water velocity value of 1450 m/s.

	Direct wave velocity before correction (m/s)
S1	1570
S2	1570
S3	1480
S4	1520
S5	1330
S6	1050
S7	1180
S8	1200
S9	1500
S10	1580

Table 4.2. Velocity model values for Sonobuoys 1 – 10 (S1 – S10) on Line 14 (also see Figure 10b), and sonobuoy distance along the line. Sonobuoy 1 lies in the deep water of the Adare Basin, while Sonobuoys 5 – 10 lie in the shallow water of the Northern Basin. Columns contain the depth (*d*, in m) and velocity (*v*, in m/s) for each layer, as derived from the sonobuoy data. Note that the first rock layer velocity for Sonobuoy 1 is 2200 m/s, while the rest have a velocity of 2000 m/s for this layer; this value is obtained by performing a normal moveout on multi-channel seismic data at the sonobuoy location, and is almost always the lower value. Uncertainty on velocity is ±100 m/s, and on depth is ±100 – 400 m (increasing with depth).

	1 (H_2O)	2	3	4	5	6	7	8	Distance along the line (km)
S1: *d*	0	1960	2950	4090	5850	7500			0
v	1450	2200	3900	4400	5600	8000			
S2: *d*	0	1780	2320	2520	2910	3660	5000		13
v	1450	2000	2200	2800	3700	4400	5000		
S3: *d*	0	1510	2130	2620	3060	3680	5130		27
v	1450	2000	2900	3500	4200	4800	5600		
S4: *d*	0	1160	1460	1800	2600	2990			38
v	1450	2000	2300	3300	4400	4800			
S5: *d*	0	520	1200	1680	2440	2930	3690		52
v	1450	2000	2800	3300	4100	4400	4700		
S6: *d*	0	500	1010	1270	1800	2500	3040		66
v	1450	2000	2500	2800	3500	4100	4500		
S7: *d*	0	470	1320	2320	2820				78
v	1450	2000	3000	4300	4500				
S8: *d*	0	440	1030	1390	2420	3040	3560		88
v	1450	2000	2500	3000	4300	4700	4900		
S9: *d*	0	470	1020	1250	2020	2700			107
v	1450	2000	2400	2900	4000	5000			
S10:*d*	0	460	1030	1230	1790	2260	2660	3350	114
v	1450	2000	2500	2900	3500	4300	4500	4900	

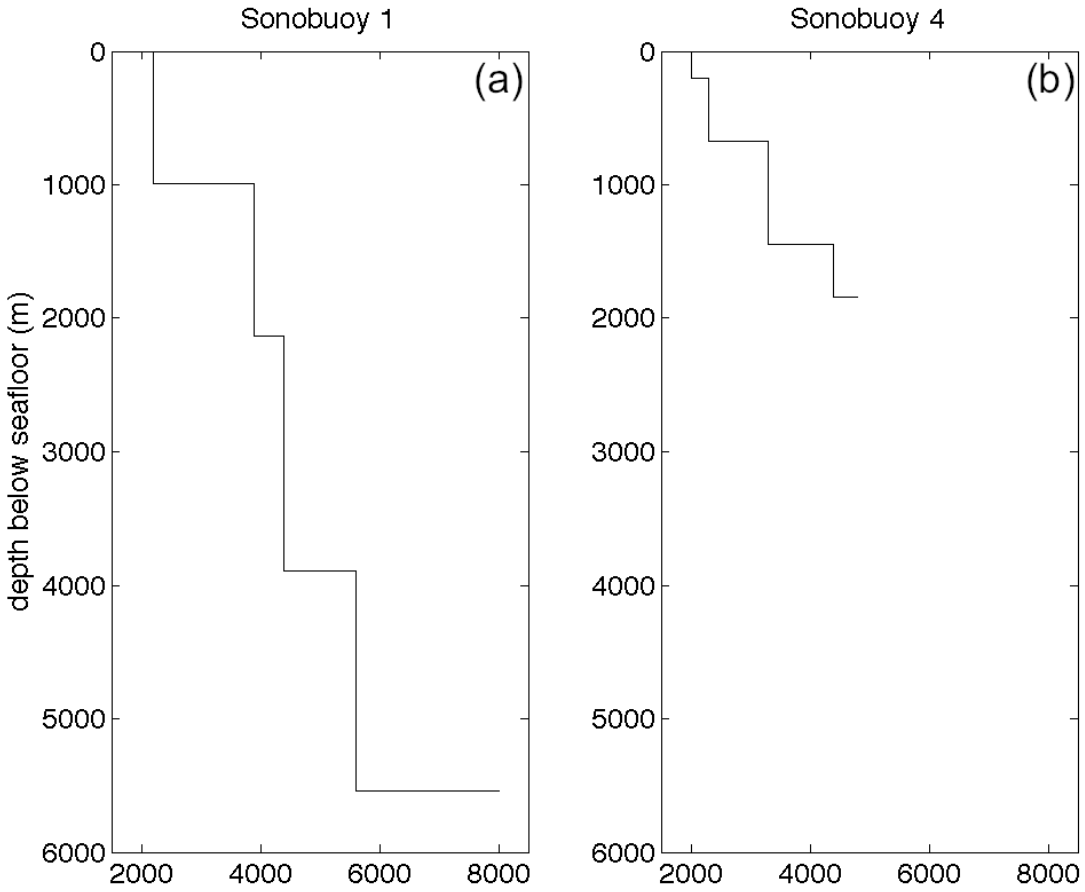

Figure 4.6. Velocity models are constructed for Sonobuoys 1 (a) and 4 (b) using the velocities and associated times obtained through standard linear moveout and normal moveout methods (see text for detail). The velocity of 8000 m/s suggests that the Moho is only 5.5 km below the seafloor beneath Sonobuoy 1. See Table 2 for velocity model details.

Layer thicknesses are summed to determine layer depths, resulting in a 1D velocity profile for the sonobuoy. Velocity profiles for Sonobuoys 1 and 4 are plotted with respect to depth below sea level for ease of comparison (Figure 6), revealing the unusually deep and high-velocity detail in Sonobuoy 1, with a maximum velocity of 8000±100 m/s at 5.5±0.4 km crustal depth. Table 2 lists the details of the velocity models for all ten sonobuoys.

Finite-difference method modeling and depth migration

We confirm the accuracy of our 1D velocity models via finite-difference (FD) method modeling of the sonobuoys, and by imaging the subsurface through depth migration of the data. Our FD model solves the acoustic wave equation in an elastic medium [*Clayton and Engquist*, 1977], using the velocity models calculated above to reproduce the sonobuoy data (Figure 7). The model solutions are 2nd order in time and 8th order in space. The high spatial accuracy is required because of the wide range of velocities in the model (1500 – 8000 m/s). We assume layer densities of 2600 kg/m^3 for velocities of 2000 m/s up to 4000 m/s; 2700 kg/m^3 for velocities of 4000 m/s up to 6000 m/s; and 2800 kg/m^3 for velocities of 6000 m/s and greater; these densities are consistent with sedimentary, basement, and lower crustal rock respectively.

By reproducing the sonobuoy data without noise, we obtain reflection times associated with each head wave. These allow us to tie the shallow structure observed in the stacked and migrated MCS data to particular velocity horizons (Figure 8). We are therefore able to interpret the shallow structure revealed by MCS data in terms of true velocities. We additionally extend the depth to which the crustal velocity structure is delineated, below the acoustic basement that limits MCS penetration.

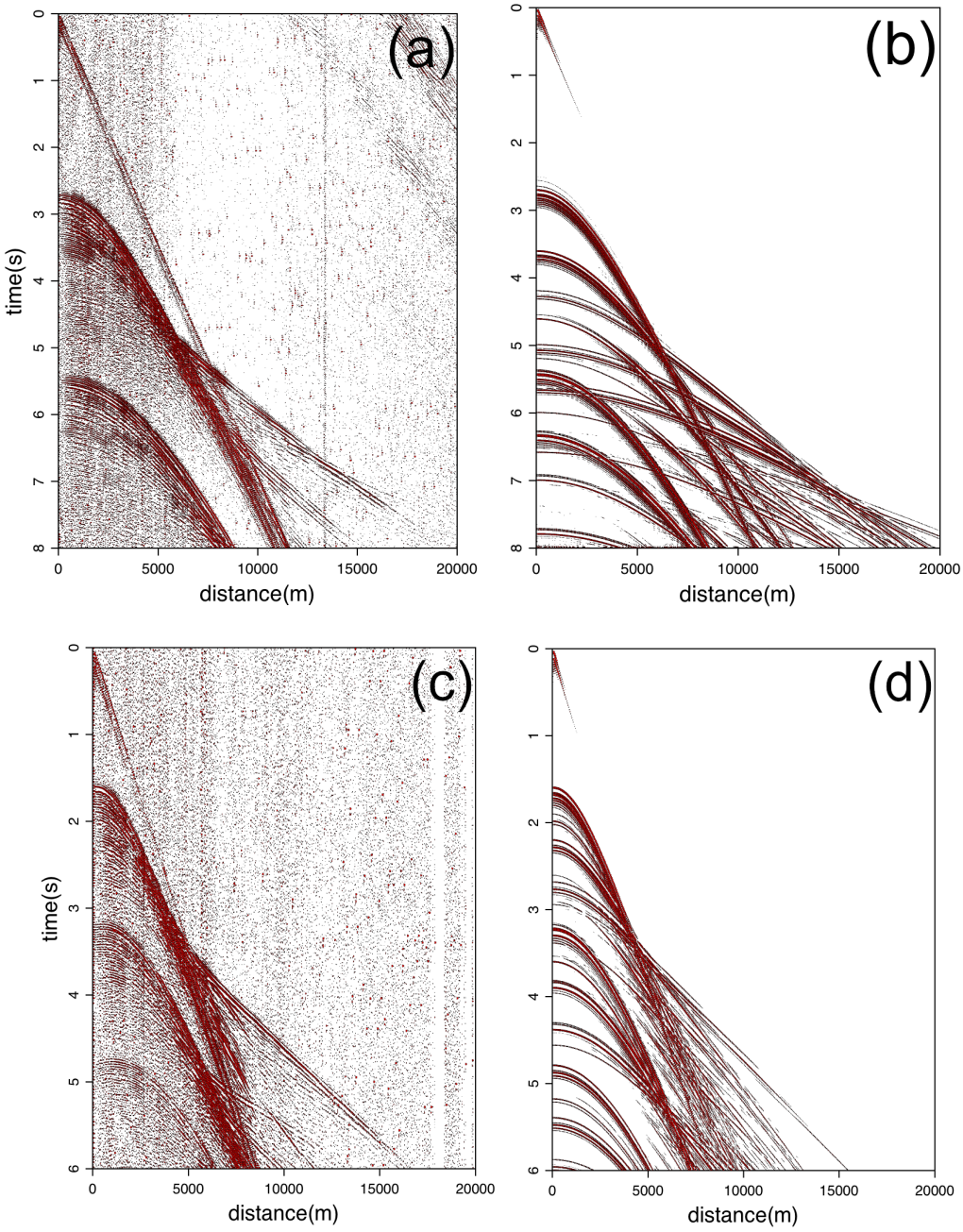

Figure 4.7. Using the velocity model derived from the distance-adjusted data for Sonobuoy 1 (a), we reproduce the key features in the data using a finite difference model (b). The finite difference model allows head wave features to be tied to their associated reflections, which come in after the seafloor reflection and are masked in the data. The corrected data for Sonobuoy 4 (c) and resulting finite difference model (d) highlight the usefulness of modeling in shallow-water locations for the identification of multiples.

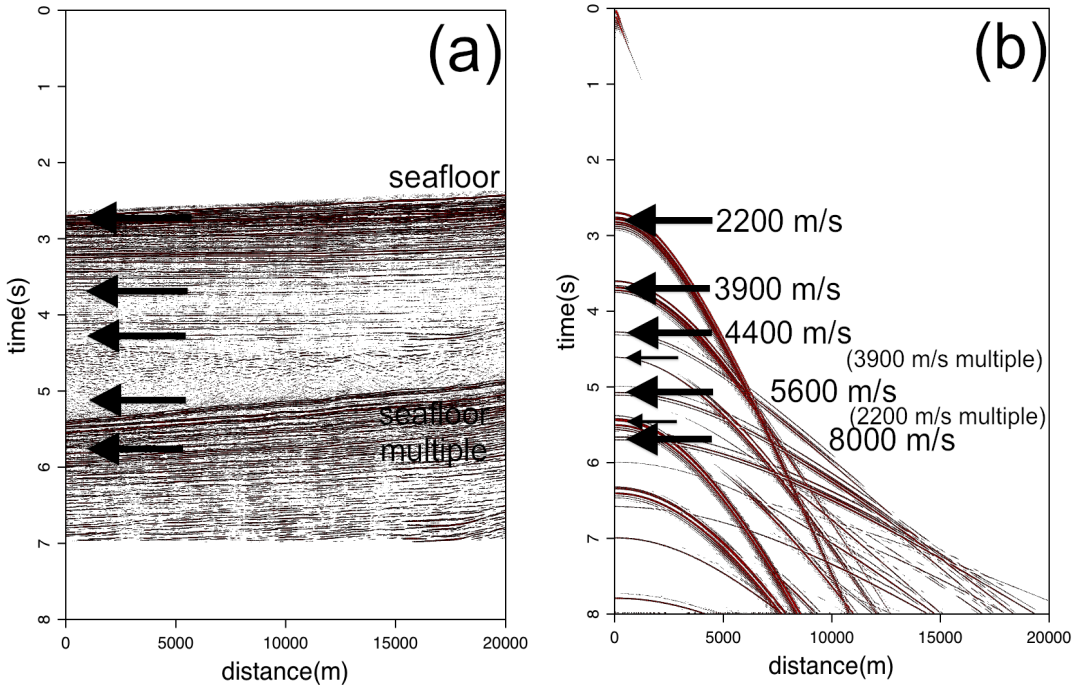

Figure 4.8. Multi-channel seismic (MCS) data from the same location as Sonobuoy 1 (a) can be compared to the finite difference model (b) in order to determine the layer velocities within the reflection data. In the model, reflections from which head waves originate are labeled with large arrows, while multiples are labeled with small arrows. Note that the first layer at depth (3900 m/s) corresponds to sediment layers imaged in the MCS data, the 4400 m/s seems to be the top of the basement rock, 5600 m/s is within the basement rock, and the 8000 m/s layer is deep in the basement rock (below the seafloor multiple). Sonobuoy data also determine layer velocities below the acoustic basement, which is the limit to which reflection data can delineate subsurface structure.

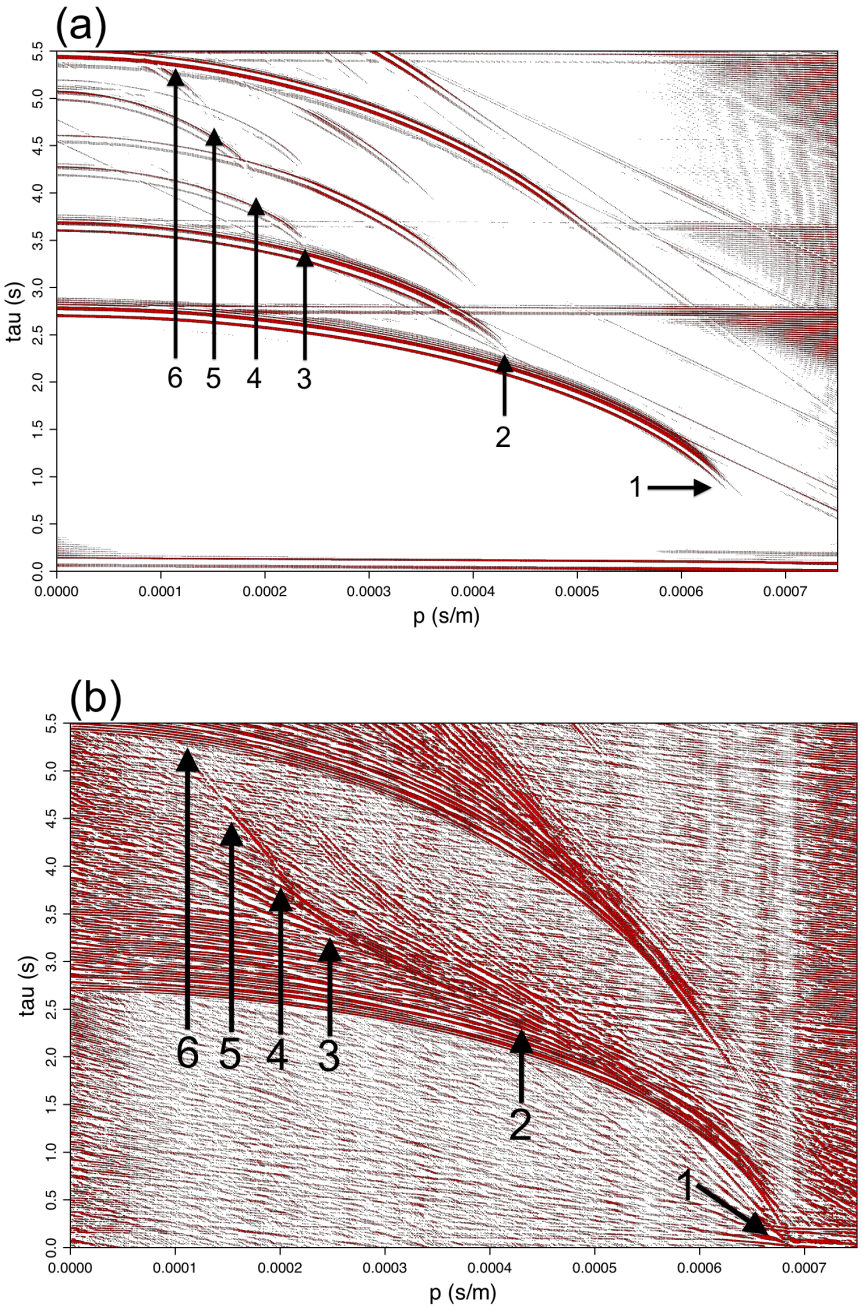

Figure 4.9. Applying a radon transform to the model (a) and data (b) for Sonobuoy 1 reveals the ellipses that image each velocity layer in τ-p space. The cusp at the beginning of each ellipse is defined in terms of the slowness (p) of the layer (or $1/v$, where v is the velocity), where layers 1 – 6 are labeled (1450 m/s, 2200 m/s, 3900 m/s, 4400 m/s, 5600 m/s, and 8000 m/s respectively). Note that cusps of layers 1, 4, and 5 are relatively low amplitude, and that layer 6 is hidden by the multiple of layer 1.

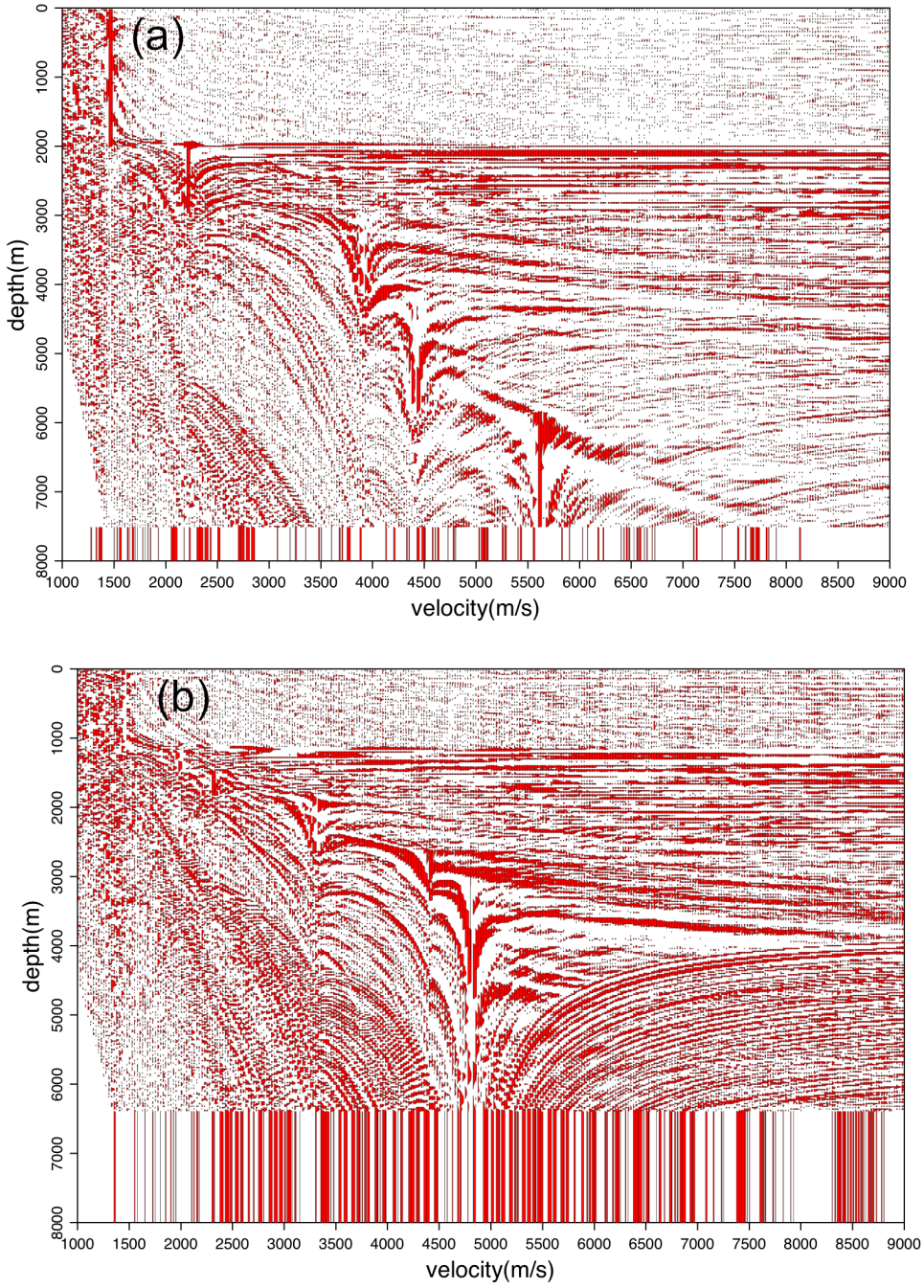

Figure 4.10. Depth migration is applied to the distance-adjusted data for Sonobuoy 1 (a) and Sonobuoy 4 (b), using their respective 1D velocity models. Parallel bedding, as observed in the multi-channel seismic data (e.g. Figure 8a), indicates a good model fit to the data; slight tilting in deeper layers indicates small lateral variations in velocity that cannot be properly modeled with 1D analysis.

We also confirm the accuracy of our 1D velocity models by using them to migrate the sonobuoy data, imaging structure at depth (Figure 10). First a radon transform is applied to the distance-adjusted sonobuoy data [e.g., *Jones*, 1999, p. 74 - 75], which organizes the data in terms of slowness ($1/v$) versus intercept time (τ). That version of the data is then migrated back to the layer interfaces it interacted with at depth, using the finite-difference version of the wave-equation method [e.g., *Jones*, 1999, p. 88], based on the 1D velocity model.

The subsurface image is in terms of velocity versus depth, and for Sonobuoy 1 (Figure 10a) shows flat shallow layers below the water layer, as observed in the stacked and migrated MCS data (Figure 8a); in general, flat interfaces in depth-migrated sonobuoy images indicate use of an accurate velocity profile. Flat shallow interfaces in the migration data for Sonobuoy 4 (Figure 10b) confirm its respective velocity model. Slight tilting in the deeper layers indicates small lateral variations in velocity that cannot be properly modeled with 1D analysis.

Constructing a 2D velocity model

We interpolate velocity values between the 1D velocity models from overlapping sonobuoys, using them as "pseudo-borehole" data, to construct a 2D velocity model along Line 14 (Figure 11). We use a Delaunay triangulation algorithm to perform the interpolation, the vertices being location (depth below seafloor and distance along the line) and velocity. The 1D models include maximum velocities of 4500 – 8000 m/s, to maximum depths of 2.7 – 7.5 km below sea level (i.e., 1.8 – 5.5 km below seafloor; see Table 2 and Figure 11b respectively). Velocities have an uncertainty of ±100 m/s, while depths below the seafloor have uncertainties from ±0.1 – 0.4 km, increasing with depth.

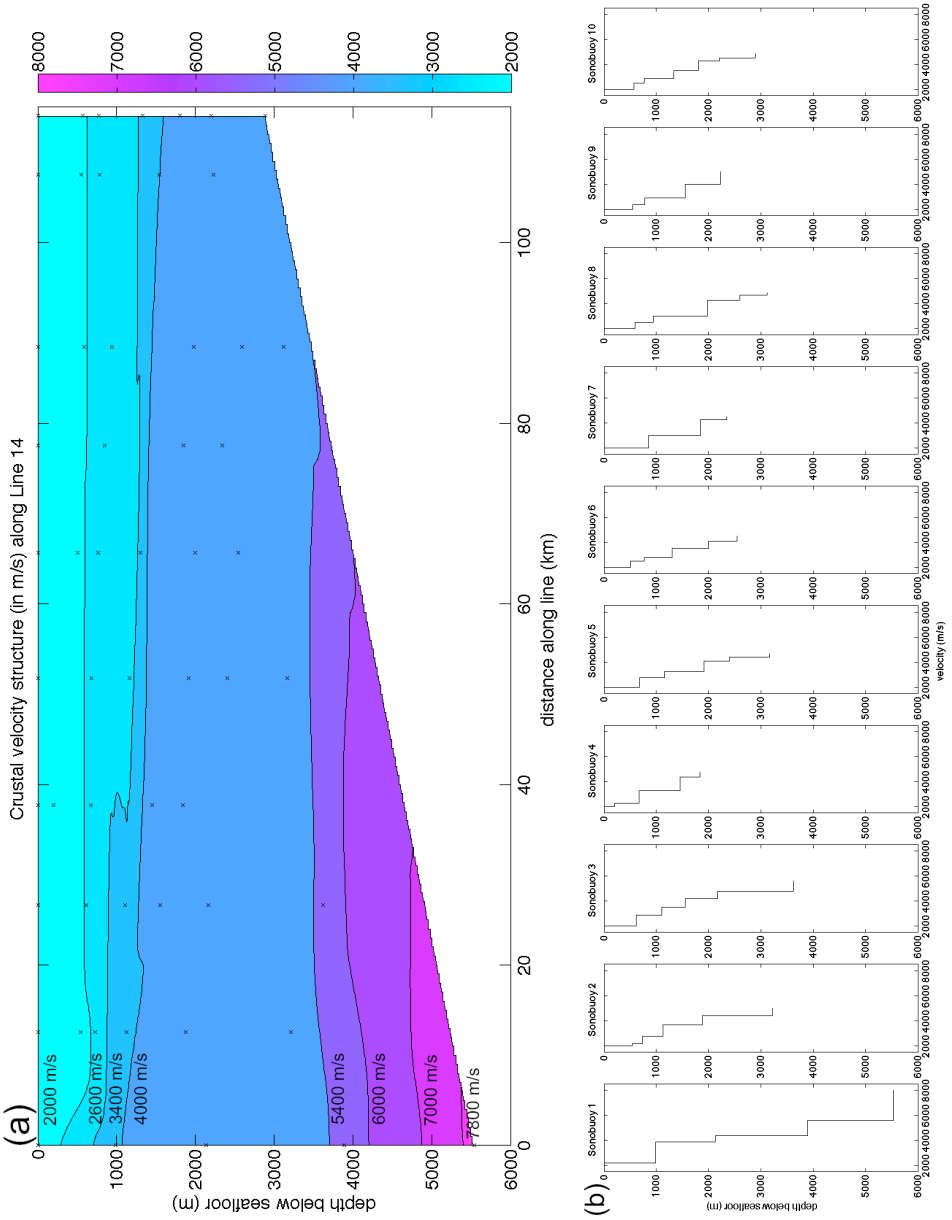

Figure 4.11. The 2D velocity structure along Line 14 is determined to a depth of 5.5 km below the seafloor (a), interpolated from velocity models for ten overlapping sonobuoys (b). Layer interfaces observed in the data are indicated with an "x" (see Table 2 for details); vertical exaggeration of 1:8. Sediment layers (~2000 – 4000 m/s) thicken slightly from the Adare Basin (Sonobuoy 1) to the Northern Basin (Sonobuoys 5 – 10), as expected for moving up a shelf break onto a sediment-filled basin. Interestingly, deeper velocity contours remain approximately flat along the line, whereas if the shelf break were the transition from oceanic to continental crust, we would expect these contours to deflect down under the Northern Basin. Uncertainties on 2D velocity contours are ±200 m/s and ±100 – 500 m (increasing with depth).

Results

We obtain a 2D velocity model to 5.5 km below the seafloor along 115 km of a seismic reflection line, through careful analysis of ten overlapping sonobuoys and interpolation between the 1D velocity profiles they provide. We determine the crustal structure to a greater depth than is possible with the MCS data alone, and provide true velocities for interpretation of the subsurface. We obtain accurate velocities by correcting the sonobuoy data before linear moveout analysis, since changing currents and ship navigation can alter the apparent velocities of head waves coming in from interfaces at depth. Other sonobuoy studies in the Ross Sea have detected sound speeds in water of 1430 – 1540 m/s, and so have not needed to make this distance adjustment before performing data analysis [e.g., *Cochrane et al.*, 1995; *Cooper et al.*, 1987; *Houtz and Davey*, 1973].

We are able to tie our 1D velocity models to layers imaged in the shallow crust using MCS because we use an FD model to reproduce the obvious features in the sonobuoy data, which allows us to determine the reflection time associated with each head wave. These reflection times are directly compared to MCS images of the subsurface, to place true velocity constraints on layer interfaces. This provides a method for determining sediment thickness, whose structure is otherwise interpreted (from MCS data) entirely in time space [*Granot et al.*, 2010].

Due to the experimental design and processing methods we employ, we are able to accurately determine the deep crustal structure in the Adare and Northern Basins. Overlapping sonobuoys allow us to construct a 2D velocity profile of the crust more cheaply than is possible with ocean-bottom seismometers, with the added benefit of real-time return of the data. Since the NBP0701 cruise deployed similarly spaced sonobuoys along other MCS lines in the southern Adare Basin and northern part of the Northern Basin, these methods can be used to construct a pseudo-3D interpretation of the crustal structure in locations where MCS lines cross (see Chapter 4).

Discussion

We show the necessity of adjusting distance between traces for sonobuoy studies, since ocean currents and changing speed and direction of the ship can alter the direct wave slope such that it does not accurately reflect the sound speed in water of 1450 m/s (see Table 1). Prior to the correction, direct wave velocities were as much as 130 m/s higher (Sonobuoy 10) and 400 m/s lower (Sonobuoy 6) than the true sound speed in water. Directly measuring layer velocities at depth by applying a linear moveout to head waves in the uncorrected sonobuoy data will be off from the true velocities of those layers by similar amounts, resulting in errors larger than the measurement uncertainty of ±100 m in most cases (seven out of ten sonobuoys).

In order to use the reflected energy features in the sonobuoy analysis, this error cannot be corrected through a simple stretch in the time dimension, based on the best fit direct wave velocity, since a hyperbolic feature will not retain its proper shape if a linear stretch is applied. In those cases where direct wave velocities differed from the true sound speed in water by more than the uncertainty of the velocity measurement, sonobuoy studies have reported inaccurate layer velocities.

Obtaining sonobuoy FD models that accurately reproduce the main features being analyzed allows for further interpretation of MCS data than is otherwise possible. MCS data image shallow structure in great detail, but cannot directly measure layer velocities at depth. Matching the reflection times from each layer of known velocity in the FD model to the MCS image provides the velocity model details needed for depth migration of MCS data.

Modeling sonobuoys using the FD also has further potential for sonobuoy data analysis, since further refinements in the model can reveal more details about the crustal structure. For instance, models could be altered to include head waves that occasionally come in late as a result of interbed multiples, further refining the 1D velocity model at that sonobuoy location. An elastic version of the model could be used to identify the converted phases in the data; an elastic FD model was run

for Sonobuoys 1 and 4 to confirm that none of the head waves used in this analysis are converted phases.

Using an elastic FD model would also constrain the allowable range of shear wave velocities, based on the amplitude of those phases. Elastic FD models with both $v_s = (1/\sqrt{3})v_p$ and a v_s half that value have converted phases with amplitudes similar to those of the main head wave features of the sonobuoy; these phases are not observed in the data, indicating shear wave velocities are small. Modeling the full range of possible shear wave velocities would help in identifying the deep crustal lithology, below the layers that can be mapped in MCS data over long distances and then tied to borehole results [e.g., *Granot et al.*, 2010]. Modeling of overlapping, and particularly reversed sonobuoys could additionally include lateral variations in layer velocity and layer thickness and a smoothly varying profile with depth, in order to determine whether these secondary effects are observed in the sonobuoy data.

Finally, our analysis is greatly aided by the experiment design. Collecting overlapping sonobuoy data along several MCS lines during research cruise NBP0701 allows us to construct 2D velocity models deep within the crust, to a greatest depth of 5.5 km below the seafloor. This depth is equivalent to 5.0 seconds travel time, far deeper than the maximum depth of 2.2 seconds in travel time imaged by the MCS data [*Granot et al.*, 2010]. We regularly determine layer velocities of 4500 – 5000 m/s, at 2.0 – 3.0 km below the seafloor, and are able to see that the velocity contours fit to these data are at consistent depths along the 115 km of MCS Line 14. Being able to use the depth penetration and ability to directly measure layer velocities that sonobuoys provide in order to construct a 2D velocity model is a particularly useful analytical technique for locations such as the Ross Sea, where sea ice conditions make using a longer MCS streamer infeasible.

Having a deep 2D velocity profile along Line 14 of the NBP0701 MCS data allows us to begin examining the crustal structure along the margin between the Adare and Northern Basins (Figure 11a). Two distinct features stand out. One is the thickness of the crust under Sonobuoy 1, which reveals a maximum velocity of 8000 m/s at 5.5 km below the seafloor, which is interpreted as the

Moho. The other obvious feature is that all velocity contours are approximately flat, indicating that it is not only unlikely for there to be significant local relief on layer interfaces within the crust, but also that the crustal type may be the same on both sides of the shelf break. In Chapter 5 these results are explored within the context of the full dataset and the regional tectonic history, and in comparison to other places in the world with similar tectonics.

Acknowledgements

We would like to thank Captain Mike Watson, the crew, and the Raytheon technical staff on board the *Nathaniel B. Palmer*. This study was supported by National Science Foundation grants OPP04-40959 (S. Cande) and OPP-0440923 and OPP-0944711 (J. Stock and R. Clayton).

Appendix: Determining 1D velocity profiles from MCS and sonobuoy data

We calculate the 1D velocity profile for each sonobuoy using standard refraction seismology techniques [e.g., *Fowler*, 1990, p. 119 - 123], additionally constraining the shallow structure with MCS data. First, the thickness of the water layer h_1 (with v_1 = 1450 m/s) is calculated using the travel time t of the first reflection from the seafloor: $h_1 = (0.5)(t_1)(v_1)$. This water depth is confirmed by comparison to the multibeam bathymetry.

Secondly, the thickness of the shallow rock layer h_2 (i.e., with v_2 = 2000 m/s) is similarly calculated: $h_2 = (0.5)(t_2 - t_1)(v_2)$. The reflection time from the base of this layer (t_2) is determined by solving the equation for determining layer thickness from refraction data, using the first head wave velocity (v_3) and its associated time (τ_1, the reduced travel time of the refracted energy when a linear moveout is applied):

$$\tau_1 = (t_1)(\cos(\theta_{13}) + (t_2 - t_1)(\cos(\theta_{23})), \qquad \text{(A1)}$$

(*term1*) (*term2*)

where θ_{13}=arcsin(v_1/v_3) and θ_{23}=arcsin(v_2/v_3).This allows the reflection and refraction data to be used together, self-consistently, to determine the shallow structure. Deeper layers are calculated from the sonobuoy data as described next.

The thickness of the third layer (h_3) is calculated using the same terms defined above except that v_3 is replaced by v_4 and they are subtracted from the linear moveout time of the layer (τ_2) and multiplied by a prefactor:

$$h_3 = \frac{v_3}{2\cos(\theta_{34})}\left[\tau_2 - term1 - term2\right], \qquad \text{(A2)}$$

where θ_{34}=arcsin(v_3/v_4). Head waves have a travel time corresponding to a ray traveling down to the interface at the critical angle ($i_c = \theta_{i,i+1}$), along the interface at the lower layer velocity (v_{i+1}), and back up to the sonobuoy at the critical angle. The factor of ½ is due to the ray traveling both down and up through the medium, and the factor of $v_i/\cos(i_c)$ is due to the ray traveling at an angle through the layer whose thickness is being calculated.

Finally, layer thicknesses at greater depth (h_i) are similarly calculated, with v_{i+1} substituted for v_3 in *term1* and *term2*:

$$h_i = \frac{v_i}{2\cos(\theta_{i,i+1})}\left[\tau_{i-1} - term1 - term2 - \sum_{j=3}^{i-1}\frac{2h_j}{v_j}\cos(\theta_{j,i+1})\right]. \qquad \text{(A3)}$$

Layer thicknesses are summed to determine layer depths, resulting a 1D velocity profile for the sonobuoy.

References

Clayton, R., and B. Engquist (1977), Absorbing boundary conditions for acoustic and elastic wave equations, *Bulletin of the Seismological Society of America*, *67*(6), 1529.

Cochrane, G. R., L. De Santis, and A. K. Cooper (1995), Seismic velocity expression of glacial sedimentary rocks beneath the Ross Sea from sonobuoy seismic-refraction data, *Geology and Seismic Stratigraphy of the Antarctic Margin, Antarctic Research Series*, *68*, 261-270.

Cooper, A., F. Davey, and G. Cochrane (1987), Structure of extensionally rifted crust beneath the western Ross Sea and Iselin Bank, Antarctica, from sonobuoy seismic data, *The Antarctic Continental Margin: Geology and Geophysics of the Western Ross Se, published by the Circum-Pacific Council of Energy and Mineral Resouces, Earth Science Series, 5B*, 93-117.

Fowler, C. M. R. (1990), *The Solid Earth: An Introduction to Global Geophysics*, Cambridge Univ Press.

Geissler, W. H., and W. Jokat (2004), A geophysical study of the northern Svalbard continental margin, *Geophysical Journal International*, *158*(1), 50-66.

Granot, R., S. Cande, J. Stock, F. Davey, and R. Clayton (2010), Postspreading rifting in the Adare Basin, Antarctica: Regional tectonic consequences, *Geochemistry Geophysics Geosystems*, *11*(8), Q08005.

Houtz, R., and F. Davey (1973), Seismic profiler and sonobuoy measurements in Ross Sea, Antarctica, *Journal of Geophysical Research*, *78*(17), 3448-3468.

Jones, E. J. W. (1999), *Marine Geophysics*, Wiley.

Jones, G. D., P. J. Barton, and S. C. Singh (2007), Velocity images from stacking depth-slowness seismic wavefields, *Geophysical Journal International*, *168*(2), 583-592.

McMechan, G. A., and R. Ottolini (1980), Direct observation of a p-τ curve in a slant stacked wave field, *Bulletin of the Seismological Society of America*, *70*(3), 775.

Ritzmann, O., W. Jokat, W. Czuba, A. Guterch, R. Mjelde, and Y. Nishimura (2004), A deep seismic transect from Hovgärd Ridge to northwestern Svalbard across the continental ocean transition: A sheared margin study, *Geophysical Journal International*, *157*(2), 683-702.

Shipp, R. M., and S. C. Singh (2002), Two dimensional full wavefield inversion of wide aperture marine seismic streamer data, *Geophysical Journal International*, *151*(2), 325-344.

Trehu, A., J. Behrendt, and J. Fritsch (1993), Generalized crustal structure of the Central basin, Ross Sea, Antarctica, *Geol. Jb*, *47*, 291-311.

Trey, H., A. K. Cooper, G. Pellis, B. della Vedova, G. Cochrane, G. Brancolini, and J. Makris (1999), Transect across the West Antarctic rift system in the Ross Sea, Antarctica, *Tectonophysics*, *301*(1-2), 61-74.

Chapter 5

DEEP CRUSTAL STRUCTURE OF THE ADARE AND NORTHERN BASINS, ROSS SEA, ANTARCTICA, FROM SONOBUOY DATA[4]

Extension associated with ultraslow mid-ocean ridge spreading in the Adare Trough, in oceanic crust north of the continental shelf in the Ross Sea, Antarctica, propogated south into the Northern Basin. Whether the Northern Basin took up the full extension or only a portion of it is unknown. Magnetic anomalies on either side of the Northern Basin appear to be continuous with anomalies on either side of the Adare Trough, in the Adare Basin. Using sonobuoys and multi-channel seismic (MCS) data collected during research cruise NBP0701, we provide constraints on crustal structure in the Adare and Northern Basins, including an estimate of crustal thickness at the continental shelf; one sonobuoy detects a velocity of 8000±100 m/s, interpreted to be the Moho, at a depth of 5.5±0.4 km below the seafloor, consistent with gravity-based crustal thickness estimates of 5 – 6 km in the Adare Basin, east of the Adare Trough [*Müller et al.*, 2005], and inconsistent with the gravity-based estimate of ~12 km (plus sediment cover) for the Northern Basin [*Davey and Brancolini*, 1995]. Overlapping sonobuoys along several MCS lines reveal 2D profiles of crustal structure in the Northern Basin, the southeastern Adare Basin, and across the continental shelf. Additional sonobuoys in the Adare Basin reveal the overall trends in crustal structure between the continental shelf and the Adare Trough. With the exception of thickening along the Adare Trough axis, we find that the Adare Basin crustal structure is consistent with that of other ultraslow spreading zones; detection of the Moho by one sonobuoy suggests that this crustal

---

[4] This research was conducted in collaboration with J. M. Stock (Seismological Laboratory, Caltech), R. Clayton (Seismological Laboratory, Caltech), R. Granot (Institute de Physique du Globe de Paris), S. Cande (Scripps Institution of Oceanography), and F. Davey (Institute of Geological and Nuclear Sciences, Lower Hutt, New Zealand), and will be submitted to the *Journal of Geophysical Research* for publication.

structure extends at least that far south as the continental shelf. Crustal structure in the Northern Basin is only determined down to basement rock, and so cannot help to distinguish between hypotheses for its deep crustal structure.

Introduction

Deformation processes through which extensional strain at mid-ocean ridge spreading zones, in relatively thin and dense oceanic crust, is transferred to neighboring continental crust are poorly understood. The breakup of Gondwanaland during Cretaceous time produced the West Antarctic Rift System (WARS) within continental crust [e.g., *Elliot*, 1992], which includes the majority of the crust in the Ross Sea (Figure 1). During mid-Cenozoic time mid-ocean ridge spreading briefly occurred at the Adare Trough, in the northwesternmost Ross Sea. Magnetic anomalies are used to constrain the timing and spreading rate of the Adare Trough [*Cande et al.*, 2000]; at least one of these magnetic anomalies is continuous with a similarly strong and narrow magnetic feature that extends into the neighboring continental shelf of the Northern Basin [*Damaske et al.*, 2007]. Multi-channel seismic [*Brancolini et al.*, 1995], sonobuoy [*Cooper et al.*, 1987; *Houtz and Davey*, 1973], and Deep Sea Drilling Project [*Hayes et al.*, 1975a; b] studies have characterized the shallow crustal structure at a few locations in the vicinity.

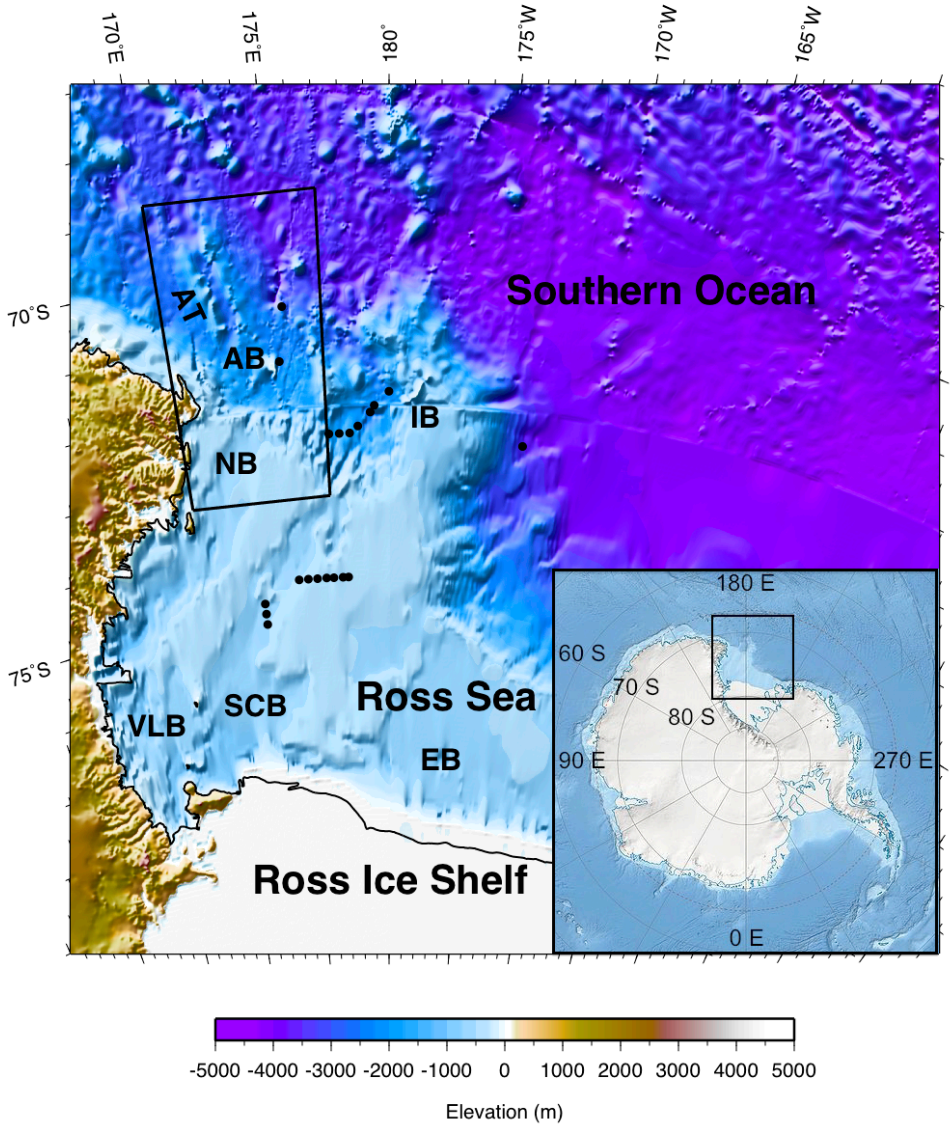

Figure 5.1. Bathymetry of the Ross Sea and Southern Ocean shows a clear delineation of the continental shelf, generally assumed to be the transition between continental and oceanic crust. Inset is the figure location with respect to Antarctica. Our study area lies at one end of the West Antarctic Rift System, in the northwestern-most Ross Sea (black box). Mid-ocean ridge style extension occurred in the Adare Trough (AT, 43 – 26 Ma [*Cande et al*., 2000]), just north of the Northern Basin (NB), one of several sedimentary basins in the Ross Sea (including Victoria Land Basin, (VLB), the Southern Central Basin (SCB), and the Eastern Basin (EB)). To the east of our study area, the continental crust of Iselin Bank juts out into the oceanic crust of the Southern Ocean. We investigate the crustal structure of the Adare and Northern Basins, and the transition between them. Sonobuoys from previous studies (black dots) are discussed in the text. Shuttle Radar Topography Mission data and estimated seafloor bathymetry are ~ 1 km resolution [*Becker and Sandwell*, 2006].

We use refraction seismic data to study both the tectonic history of the area and the more general question of how extensional strain in oceanic crust is transferred to continental crust. While extension in the Adare Basin was concentrated in mid-ocean rifting along the Adare Trough, did extension also affect the neighboring continental margin? How did a narrow zone of extension in oceanic crust transfer into various mechanisms for rifting continental crust? How much and where did the processes of magmatic intrusion and crustal thinning allow for extension in the Northern Basin?

In this paper we present the analysis of sonobuoy data collected during research cruise NBP0701 on board the *R/VIB Nathaniel B. Palmer*, in the Adare and Northern Basins (Figure 2). This is a companion paper to the analysis by Granot et al. [2010] of the multi-channel seismic (MCS) data from the same cruise. The Adare Trough lies in the deep water of the Adare Basin and trends southward toward the Northern Basin, which is on the continental shelf. While the MCS data are useful for determining the velocity of the shallowest rock layer, sonobuoy data allow us to directly measure layer velocities at depth (see Chapter 3). The 71 sonobuoys presented here, deployed along the 19 MCS lines, provide a deeper and more detailed look at the crust around the Adare Trough, and in the Northern Basin, than was possible in prior studies.

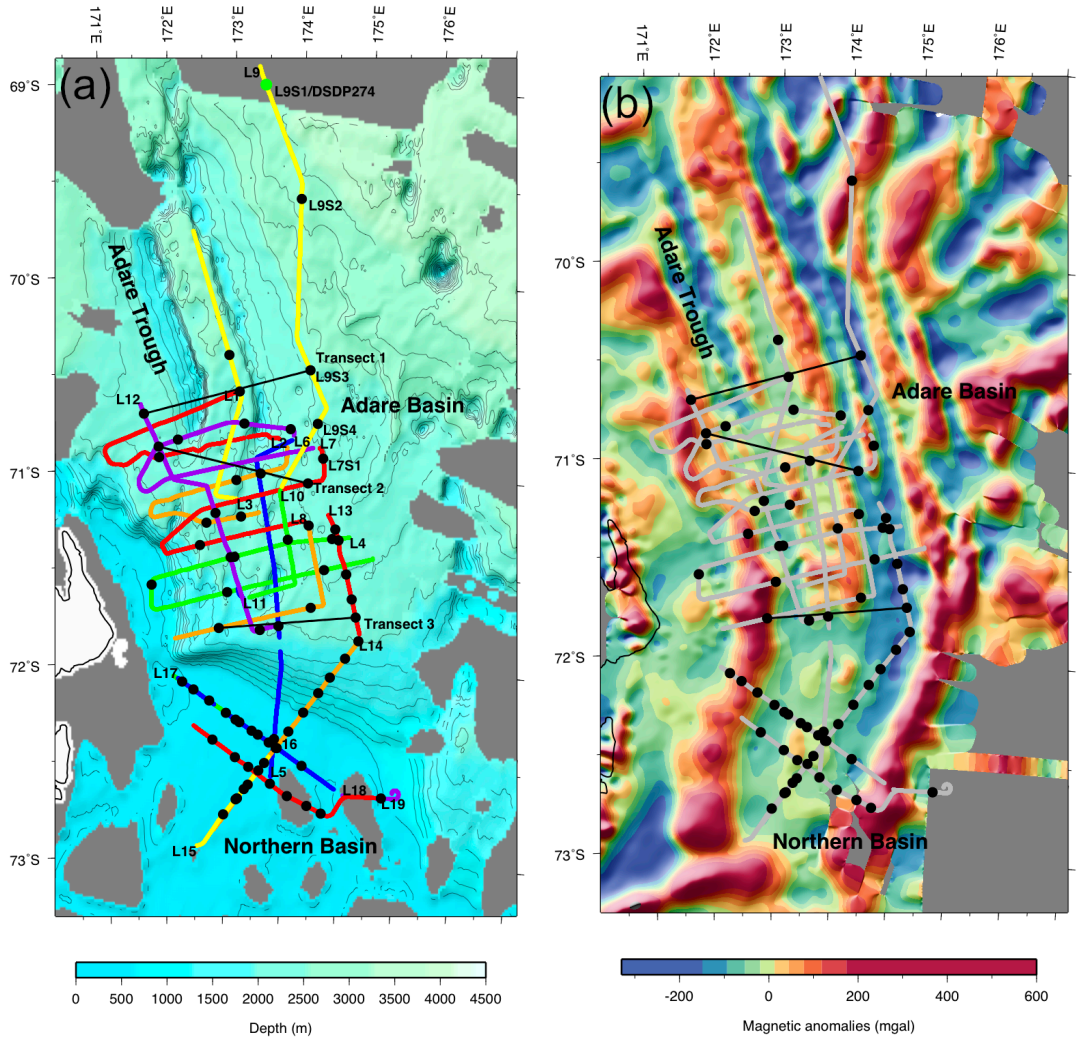

Figure 5.2. We investigate crustal structure in the Adare and Northern Basins using multi-channel seismic (MCS) and sonobuoy data. (a) Locations of MCS lines (colored lines, labeled at the beginning of the line) and sonobuoys (black dots) from research cruise NBP0701 are displayed on top of multibeam bathymetry [NBP0701 Data Report, 2007]. We show crustal velocity structure along transects (black lines) and Lines 13 – 19, and for individually labeled sonobuoys, in the remaining figures. We also show the location of Deep Sea Drilling Project site (DSDP) 274 (green dot, collocated with sonobuoy L9S1). (b) Magnetic anomalies within the Adare Basin appear to be continuous with anomalies along the east and west sides of the Northern Basin, suggesting continuity of crustal structure between the two basins [*Cande and Stock*, 2006]. We show shipboard magnetic [*Cande et al*., 2000; *Cande and Stock*, 2006] and aeromag data [*Damaske et al*., 2007] compiled by Roi Granot, overlain by MCS line, transect, and sonobuoy locations (in gray and black).

Tectonics of the northwestern Ross Sea

During the final stages of breakup of Gondwanaland in mid-Cretaceous time (~100 Ma), the Ross Sea margin of Antarctica rifted from the Campbell Plateau and the South Tasman Rise. The Campbell Plateau bordered the Marie Byrd Land terrain of West Antarctica and most of the Ross Sea continental margin, while the South Tasman Rise was adjacent to the westernmost Ross Sea and Cape Adare, of East Antarctica [*Weaver et al.*, 1994]. At ~90 Ma, the South Tasman Rise was still close to East Antarctica and the Iselin Bank, a protrusion in the Ross Sea continental margin east of Cape Adare [*Gaina et al.*, 1998]. Tectonic reconstructions [*Cande et al.*, 1995] and the crustal structure of the Iselin Bank [*Cooper et al.*, 1987] suggest that it is continental material that may have been part of East Antarctica.

At the same time that Antarctica was separating from the last few other pieces of continental crust that made up Gondwanaland, rifting between East and West Antarctica began. Rifting in the WARS was broadly distributed, with 500 – 1000 km of transtensional motion occurring since mid-Cretaceous time [*Luyendyk et al.*, 1996]. Extension between the South Tasman Rise and the portion of East Antarctica at the northwestern edge of the Ross Sea began ~60 Ma, rifting slowly, while ~500 km of extension between East and West Antarctica occurred 80 – 40 Ma [*Cande et al.*, 2000; *Molnar et al.*, 1975]. Since the WARS is tectonically complex and difficult to study due to the extreme conditions, and because much of the rifting was within continental crust and extremely slow, it remains the least well constrained step in the global plate circuit.

Eocene marine sediments from the eastern Ross Sea during Eocene time (57 – 35 Ma) confirm the above timeline for opening the Ross Sea due to rifting in the WARS [*Truswell and Drewry*, 1984]. North–south trending basins and ridges formed in the Ross Sea region of the WARS during periods of extension in late Cretaceous and early Cenozoic time [*Cooper et al.*, 1987]. In particular, at ~60 Ma the Iselin Bank was adjacent to Cape Adare, whereas by ~27 Ma it had moved to its current position in order to accommodate extension north of the Ross Sea, creating the Northern Basin in the process [*Cande and Stock*, 2004].

Clusters of volcanic knolls in the continental margin offshore Cape Adare and in the Adare Basin indicate volcanism that postdates formation of the oceanic crust of the Adare Basin [*Panter and Castillo*, 2007]. The volcanic knolls are similar in composition to other volcanic features in the western Ross Sea, including the active volcano Mt. Erebus on Ross Island, indicating a regional rather than local source [*Panter and Castillo*, 2007]. A deep tomographic study (>100 km depth) indicates that relatively hot mantle underlies the western Ross Sea [*Sieminski et al.*, 2003].

The western Ross Sea has also experienced distributed tectonic deformation since mid-Cenozoic time, including the subsidence that formed the Victoria Land and Northern Basins [*Cooper and Davey*, 1985]. Extension was concentrated in the Adare Trough during some of this time, which was an axis of seafloor spreading from 43 – 26 Ma [*Cande et al.*, 2000]. Recent minor extensional episodes at ~24 Ma, ~17 Ma, and ongoing today have disrupted the sediments that were deposited on top of the Adare Basin after its formation [*Granot et al.*, 2010]. Features in magnetic, gravity, and MCS data are not offset across the boundary between the Adare and Northern Basins, indicating that these basins are structurally continuous [*Cande and Stock*, 2006; *Damaske et al.*, 2007], despite the abrupt transition from shallow to deep water that suggests that this boundary is the northwesternmost extent of the continental margin in the Ross Sea.

Multi-channel seismic data in the Adare and Northern Basins

MCS data collected during research cruise NBP0701 were processed and analyzed for structure and deformation in the sedimentary layers of the subsurface; primaries were resolvable up to 2.2 seconds of travel time, to the acoustic basement [*Granot et al.*, 2010]. While several sediment horizons can be continuously traced throughout the region, sediment thickness varies widely depending on the basement topography. Thicknesses generally range from 0 seconds in travel time along the ridges that define the Adare Trough, to 2.0 seconds at one point within the trough, and reach their thickest (2.2 seconds) in the Northern Basin and the margin slope [*Granot et al.*, 2010].

Previous seismic refraction studies in the Ross Sea

Seismic refraction data collected in the Ross Sea provide clues to the deep crustal structure of the basins and ridges that make up its seafloor. Most sonobuoy studies in the western Ross Sea focused on Victoria Land Basin, and used linear moveout and ray tracing methods to determine velocity gradients through sediment [e.g., *Cochrane et al.*, 1995; *Cooper et al.*, 1987; *Houtz and Davey*, 1973]. Ocean bottom seismic refraction studies investigated the deeper crustal structure in the central and southern Ross Sea, using ray tracing and amplitude modeling methods [*Trehu et al.*, 1993; *Trey et al.*, 1999].

Sonobuoys deployed in northern Victoria Land Basin, in shallow water just south of our study area (three at ~75.0° – 76.0° S and ~173.0° E, and seven at ~74.5° S and ~175.0° – 178.0° E), detected maximum sediment velocities >4.0 km/s and basement velocities of 5.0 – 5.8 km/s, and assumed basement depths of 1.0 – 1.6 km subseafloor [*Houtz and Davey*, 1973]. Sonobuoys in deep water along the continental shelf between the Northern Basin and the Iselin Bank, just east of our study area (six in an arc from ~72.4° S and ~177.1° E to ~71.8° S and ~180.0° E), revealed maximum sediment velocities up to 4.3 km/s, assumed basement velocities up to 4.7 km/s, and basement depths of up to 3.0 km subseafloor [*Houtz and Davey*, 1973]. However, a similar study indicated that many velocities >4.9 km/s are in fact layered sedimentary units and not igneous-metamorphic basement [*Cooper et al.*, 1987], so it is not clear that the depths reported above are in fact the basement depths at those locations.

Additional sonobuoys deployed over the Iselin Bank and in the deep water to its east and west indicate that Iselin Bank is continental crust, with oceanic crust of thickness ~10 km to the east (at ~72.5° S and ~ 173.5° W, where a velocity of ~8.0 km/s is interpreted as the top of the mantle [*Cooper et al.*, 1987]). To the west, just east of our study area (at ~72.0° S and 179.3° E), a velocity of 5.2 km/s was detected at 4.3 km sub-seafloor depth, and similar velocities were

detected at 2.8 and 1.8 km subseafloor depth in the Adare Basin (at ~71.3° S and ~175.0° E, and ~70.5° S and ~175.3° E, respectively; [*Cooper et al.*, 1987]).

In the southern Ross Sea, again mostly focused in the Victoria Land Basin, sonobuoys revealed a range of velocity gradients similar to those found in sediment further north [*Cochrane et al.*, 1995]; Ross Sea sedimentary velocities are systematically higher than those of sediments at a similar depth in the Gulf of Alaska [e.g., *Bruns and Carlson*, 1987] and the Gulf of Mexico [e.g., *Gardner et al.*, 1974]. This is interpreted as the result of compaction of Ross Sea sediments due to past loading by a grounded ice sheet [*Cochrane et al.*, 1995]. Similarly high sediment layer velocities at shallow depths in the northern Svalbard margin are also attributed to ice loading [*Geissler and Jokat*, 2004].

Lines of ocean bottom seismometers across the Central Basin indicated that the crustal thickness in the region, defined as depth to material with a velocity of >8.0 km/s, is ~19 km [*Trehu et al.*, 1993]. Within the Central Basin, the crust was interpreted to be a preexisting basement layer that has been thinned to ~5 km, an underlying layer of ~7 km of magmatic intrusions, and a top ~7 km layer of sedimentary rock. On either side of the basin, the crustal thickness implies continental material that has been thinned to approximately half that of East Antarctica [*Trehu et al.*, 1993]. A line of ocean bottom seismometers across the southern Ross Sea, from the Victoria Land Basin well into the Eastern Basin, revealed variable crustal structure [*Trey et al.*, 1999]. The sedimentary basins (Victoria Land, Central, and Eastern Basins) are underlain by highly extended crust and mantle as shallow as 16 km subseafloor; beneath the intervening basement highs, crust thickens slightly to 21 – 24 km.

Sonobuoy analysis methods

MCS data were recorded with a 1 km, 48-channel streamer. Most shots used a 6-gun G/I source array with a total capacity of 20.6 liters (Lines 1 – 12). For the seismic lines on and near the continental shelf, we used a 6-element Bolt-gun array with a total capacity 34.8 liters (Lines 13 – 19). The typical source spacing was approximately 40 m. Most sonobuoys transmitted data until they were 20 – 30 km from the ship. Sonobuoys were deployed occasionally in deep water, and with a regular spacing of ~15 km in shallow water (see Figure 2). We use MCS data to constrain the velocity of the shallowest rock layer, and sonobuoy data to reveal velocity profiles deep into the crust. We confirm our 1D velocity models for each sonobuoy through finite difference method modeling and depth migration of the sonobuoy data. Overlapping sonobuoys are used to construct 2D velocity models. Details of data analysis, modeling, and 2D velocity model interpolation are provided in Chapter 4.

Results of 1D and 2D velocity models

Deep structure in the Adare Basin

MCS Lines 1 – 13 provide good coverage of the Adare Basin; 36 deep-water and two shallow-water (on the continental shelf) sonobuoys deployed along these lines reveal the deep structure of the crust from the southern end of the Adare Trough to the continental shelf at the north end of the Northern Basin. These sonobuoys are generally spaced further apart from each other (>30 km) than the offsets from the ship to which they recorded data (20 – 30 km), and so provide 1D velocity models of Adare Basin structure at 36 distinct points.

Sonobuoys in the Adare Basin record head waves from layers at maximum depths of 0.5 – 5.4 km into the crust; 28 of the 36 penetrate >2.0 km. These sonobuoys reveal variable-thickness sedimentary layers (in agreement with MCS data [*Granot et al.*, 2010]) on top of basement rock, in

four cases with maximum interval velocities of 7000 – 7400 m/s at 3.0 – 5.4 km below the seafloor. In another 15 sonobuoys, maximum interval velocities of 6000 – 7000 m/s are observed at similar depths (see Table 1). Velocities are uncertain to ±100 m/s and depths are uncertain up to ±0.4 km (increasing with depth).

Since these sonobuoys are not closely spaced, they do not provide true 2D velocity models along transects through the Adare Basin. However, for aid in visualizing the trends in 1D velocity models, we do provide three 2D velocity models along transects through the northern, middle, and southern Adare Basin, and a comparison of 1D velocity models along the trend of Line 9, which ran along the eastern side of the Adare Trough. Sonobuoys used to interpolate these transect 2D velocity models are widely and irregularly spaced (23 – 60 km apart), and collected along different azimuths (between the ship and receiver), but effectively illustrate trends in crustal structure throughout the Adare Basin.

The northernmost of these 2D velocity models, Transect 1, is bounded by Line 12, Sonobuoy 1 (L12S1, at 171.6° E, 70.7° S) to Line 9, Sonobuoy 3 (L9S3, at 174.2° E, 70.5° S), and crosses the southern Adare Trough roughly perpendicular to its axis (see Figure 2 for transect location). Velocity contours along Transect 1 deepen in the middle (Figure 3a), where L3S2 (Figure 3c) detects the crustal structure within the Adare Trough. The three sonobuoy velocity models used to construct this 2D velocity model all reveal simple three-layer structures, with maximum velocities of 6500 m/s, 5000 m/s, and 5400 m/s (L12S2, L3S2, and L9S3 respectively; Figures 3b – 3d). Note that the smallest of the maximum velocities along this transect is detected at the greatest depth below the seafloor.

The mid-latitude 2D velocity model along Transect 2 is bounded by L12S2 (at 171.9° E, 70.9° S) and L7S2 (at 174.2° E, 71.7° S), and also crosses the Adare Trough roughly perpendicular to its axis. However, the Adare Trough changes azimuth at this latitude, putting Transect 2 at an angle to Transect 1 (see Figure 2). In this case, one sonobuoy (L12S2) lies to the west of the trough and the

remaining two (L2S1 and L7S2) lie to its east. This 2D velocity model shows lower velocity contours, up to 4000 m/s (likely consolidated sediment), lying deeper beneath the west side of the Adare Basin than they do on the east side (Figure 4a). However, higher velocity contours, up to 6000 m/s (likely basement rock), remain approximately flat along Transect 2. At the two ends of this transect, L12S2 (Figure 4b) and L7S2 (Figure 4d) reveal maximum layer velocities of 6500 m/s and 7400 m/s respectively. The latter value is the highest layer velocity detected in the Adare Basin, and is typical of lower oceanic crust.

The southernmost of these 2D velocity models, Transect 3, is bounded by L8S3 (at 172.9° E, 71.8° S) and L13S6 (at 175.1° E, 71.7° S), and runs along the base of the continental shelf separating the Adare and Northern Basins (see Figure 2). The highest velocity contours (5000 – 5600 m/s) dip down slightly to the west along this transect, while lower-velocity contours deepen in the middle (Figure 5a). The two sonobuoys along this transect that lie closest to the continental shelf (L8S3 and L12S6; Figures 5b and 5c) detect the deepest layers with velocities <6000 m/s (5700 m/s and 5300 m/s, at depths of 4.1 km and 4.3 km below the seafloor, respectively) observed in the Adare Basin.

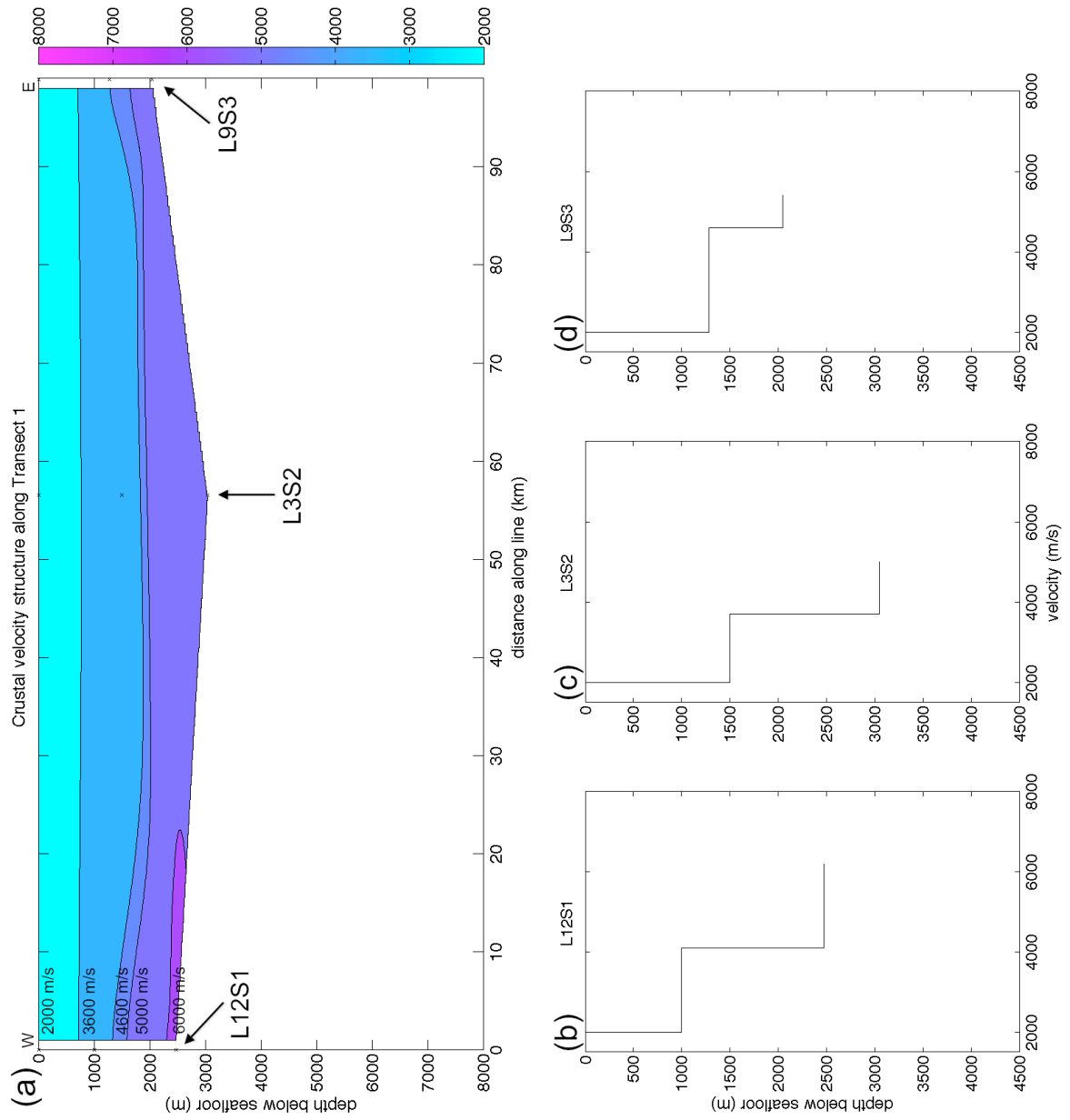

Figure 5.3. 2D velocity model along Transect 1 (a), which crosses the Adare Trough, with velocity contours based on interpolation between three 1D velocity models. Depths of individual layers directly detected in the sonobuoy data ("x") indicate the positions of the three sonobuoys. The velocity model is accurate for ±5 km along the line at each sonobuoy, and is primarily constructed to display trends in Adare Basin deep crustal structure; velocities are uncertain to ±100 m/s, depths up to ±0.4 km (increasing with depth). Note the downward deflection of the velocity contours under the Adare Trough (center sonobuoy) in comparison to their positions on the flanks. 1D velocity models are arranged in order of their position in the 2D model (b – d).

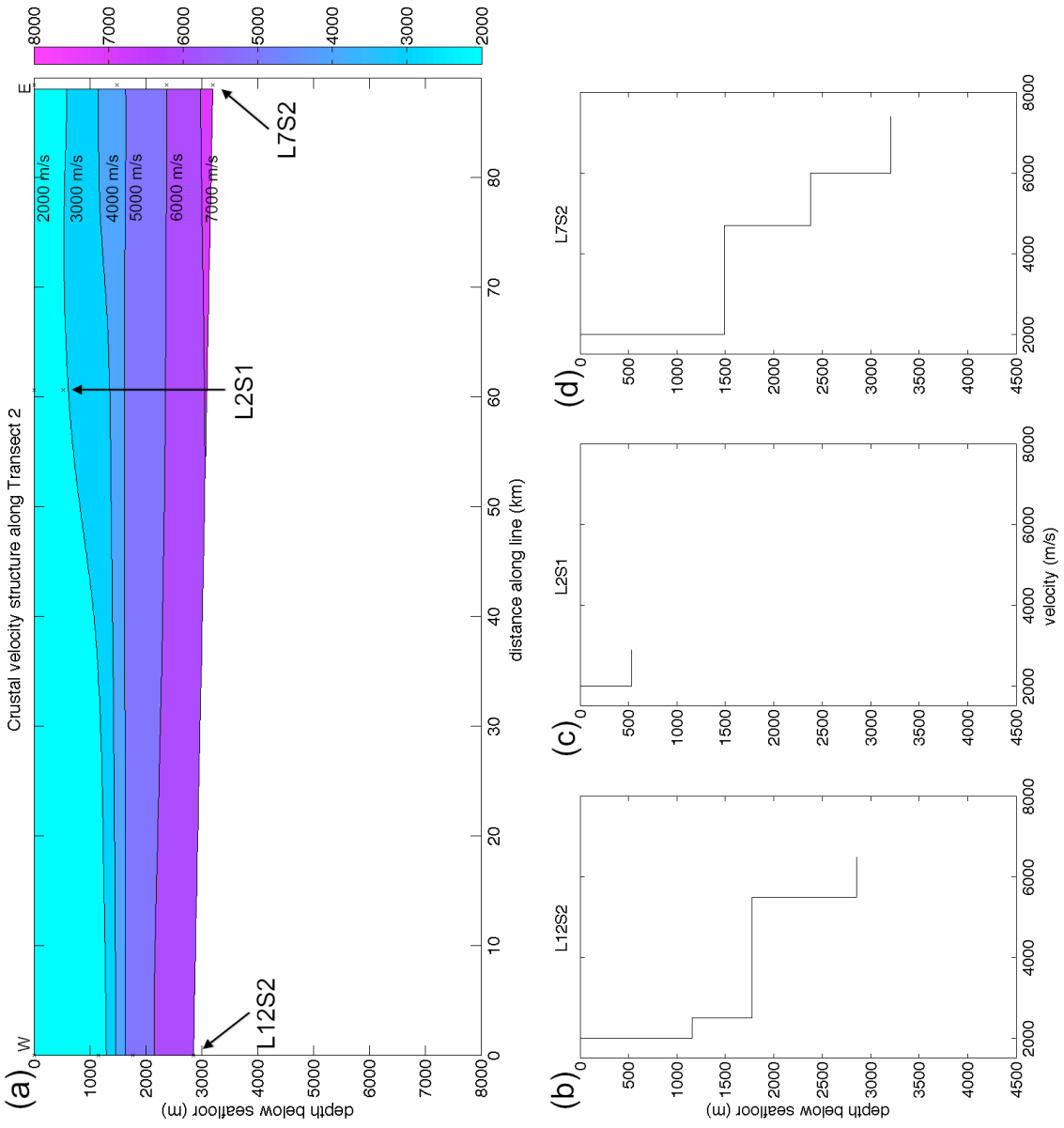

Figure 5.4. 2D velocity model along Transect 2 (a), south of Transect 1 in the Adare Basin, shows velocity contours based on interpolation between three 1D velocity models. Depths of individual layers directly detected in the sonobuoy data ("x") indicate the positions of the three sonobuoys. The 2D velocity model is accurate for ±5 km along the line at each sonobuoy, and is primarily constructed to display trends in Adare Basin deep crustal structure; velocities are uncertain to ±100 m/s, depths up to ±0.4 km (increasing with depth). Note the changing depths of the shallow velocity contours (2000 m/s and 3000 m/s), and the flat underlying contours. 1D velocity models are arranged in order of their position in the 2D model (b – d); L7S2 (d) is one of three sonobuoys to detect a head wave velocity >7000 m/s in the Adare Basin, consistent with lower oceanic crust.

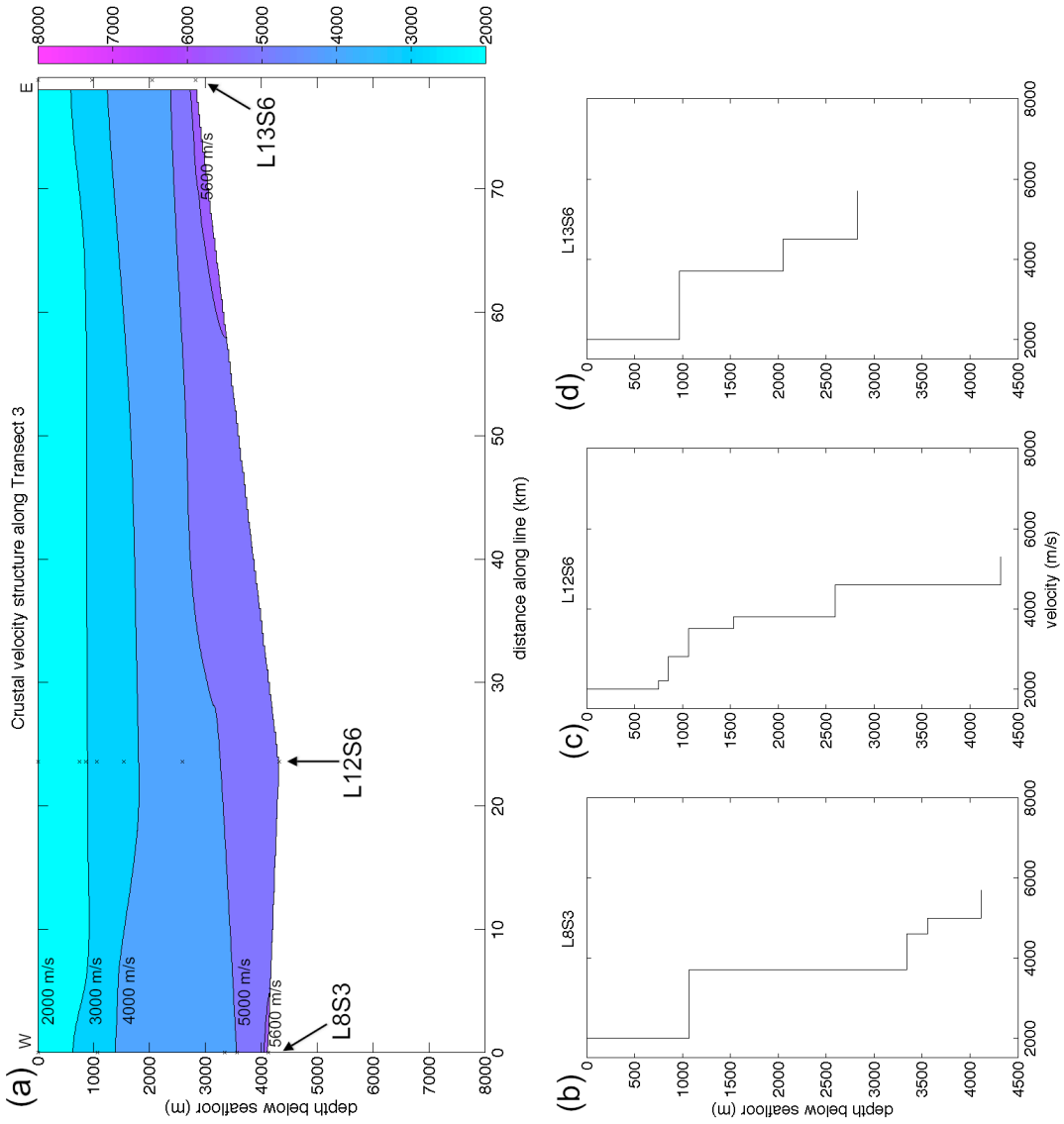

Figure 5.5. 2D velocity model along Transect 3 (a), along the continental shelf in the southern Adare Basin, shows velocity contours based on interpolation between three 1D velocity models. Depths of individual layers directly detected in the sonobuoy data ("x") indicate the positions of the three sonobuoys. The 2D velocity model is accurate for ±5 km along the line at each sonobuoy, and is primarily constructed to display trends in Adare Basin deep crustal structure; velocities are uncertain to ±100 m/s, depths up to ±0.4 km (increasing with depth). Note that the shallow velocity contours (2000 – 4000 m/s) are relatively flat, while the 5000 m/s contour dips down to the west and the 5600 m/s contour is deflected down in the middle. 1D velocity models are arranged in order of their position in the 2D model (b – d); sonobuoys L8S3 (b) and L12S6 (c) detect the deepest layers with velocities <6000 m/s in the Adare Basin, and correspond to the southern-most boundaries of thick sediments and shallow deformation associated with the Adare Trough.

Sonobuoys along the trend of MCS Line 9, including the four on that line as well as L7S1, span the length of the Adare Trough, from DSDP site 274 at its northern end (with which L9S1 is collocated) to the change in azimuth at its southern end (see Figure 2). From north to south, these sonobuoys have maximum layer velocities of 6800 m/s, 5900 m/s, 5400 m/s, 6000 m/s, and 7000 m/s (L9S1, L9S2, L9S3, L9S4, and L7S1 respectively), with relatively shallow depths for these layers of 0.7 km, 1.3 km, 2.0 km, 1.4 km, and 3.1 km below the seafloor (see Figures 6a – e). Sonobuoys on Line 9 detect fairly simple structure, with only two to three layers, as do sonobuoys along Transect 1. In contrast, sonobuoy L7S1 detects five layers, typical of sonobuoys south of Transect 1 in the Adare Basin that detect layer velocities >5000 m/s (of these 24 sonobuoys, 21 detect four to seven layers).

Within the Adare Basin, overlapping sonobuoys were only collected along MCS Line 13, while approaching the continental shelf of the Northern Basin from the north (from L13S2, at 174.7° E, 71.3° S, to L13S6, at 175.1° E, 71.7° S). An actual 2D velocity model (Figure 7a) constructed from these five sonobuoys (Figures 7b – f) reveals a crustal structure that is consistent with the eastern ends of Transects 2 and 3. The 2D velocity model for Line 13 indicates that the southern Adare Basin has flat velocity contours, within depth uncertainties of up to ±0.4 km for the deepest contours. Below the seafloor, which is the top of the rock layer with 2000 m/s velocity, contours of 3000 m/s, 4200 m/s, 4900 m/s, 5700 m/s, and 6000 m/s lie at depths of ~0.6 km, ~1.8 km, ~2.3 km, ~3.1 km, and ~3.3 km respectively. The southernmost sonobuoy on MCS Line 13 lies just northwest of the first sonobuoy on MCS Line 14, which crosses the continental shelf.

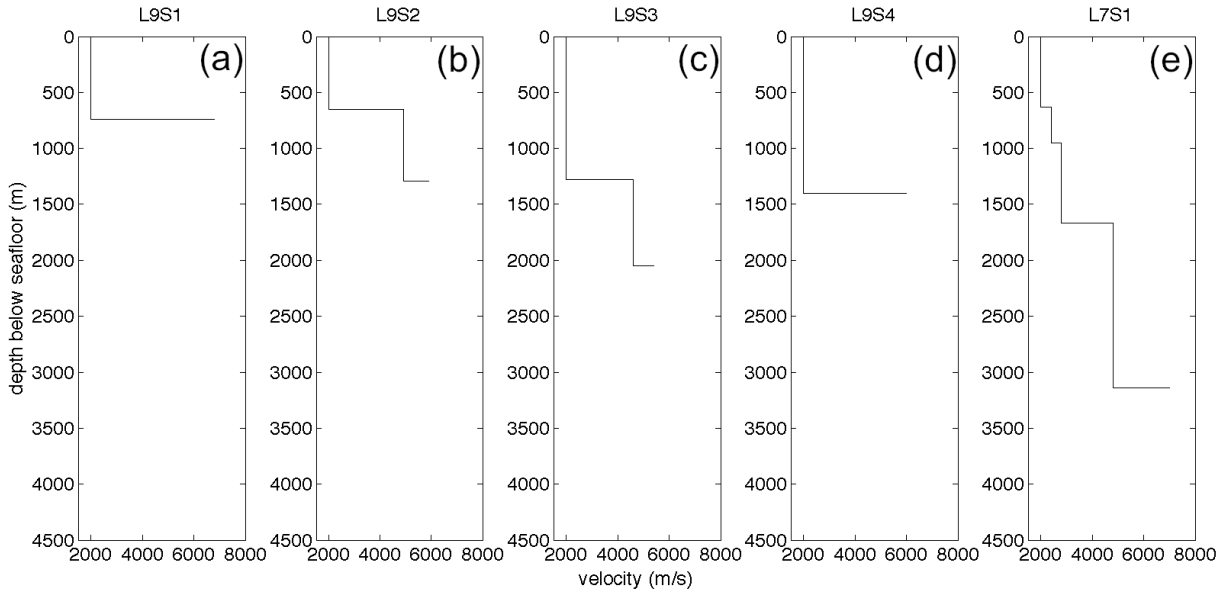

Figure 5.6. From north to south (a – e), sonobuoys along the east flank of the Adare Trough have maximum layer velocities of 6800 m/s, 5900 m/s, 5400 m/s, 6000 m/s, and 7000 m/s (respectively), the first four at relatively shallow depths compared to all sonobuoys in the Adare Basin. All five are consistent with a gravity-based crustal thickness east of the Adare Trough of 5 – 6 km [*Müller et al*., 2005]. Sonobuoy L7S1 (e) shows one of three detections of a layer with velocity >7000 m/s in the Adare Basin, consistent with lower oceanic crust.

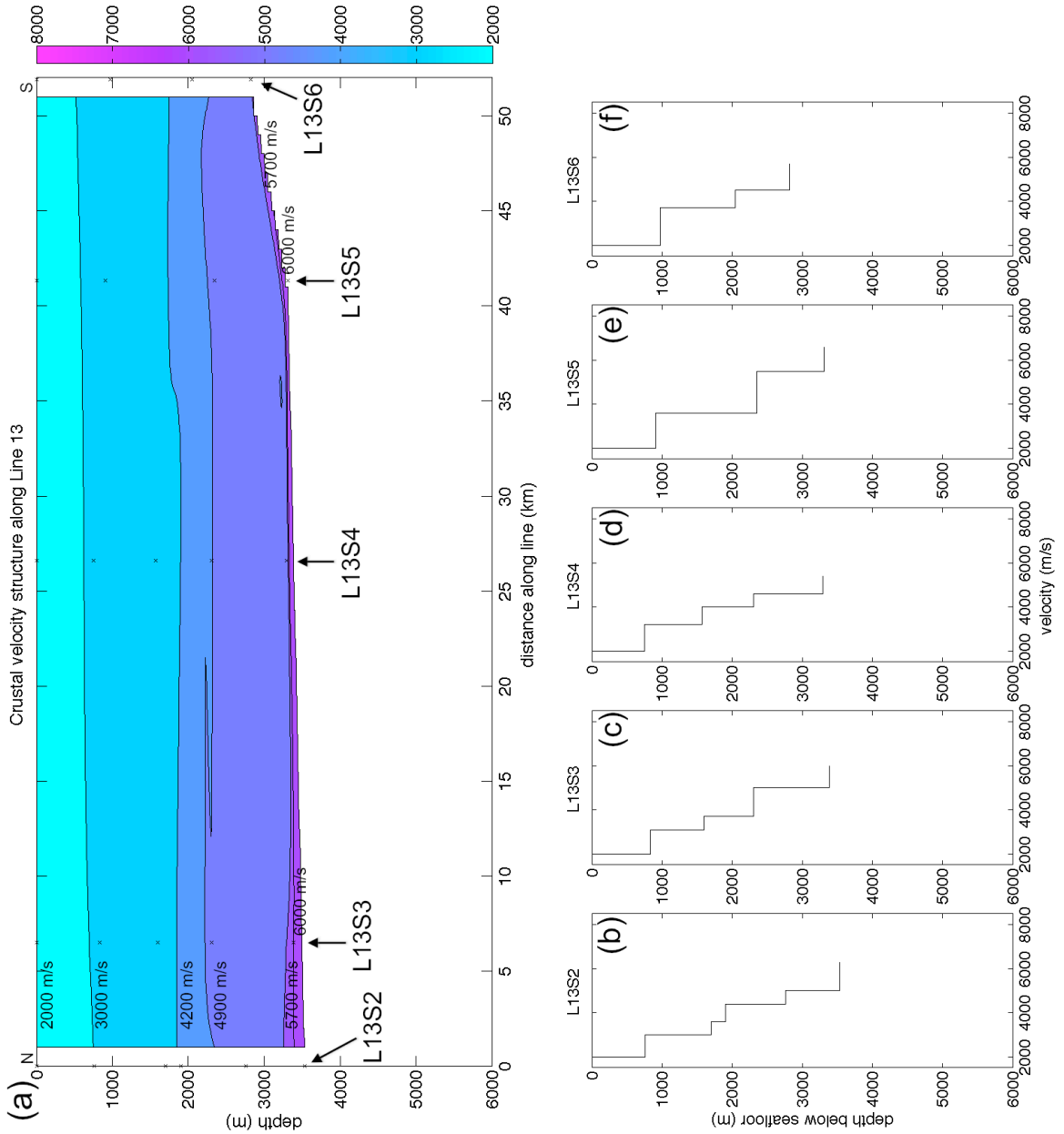

Figure 5.7. A 2D velocity model along Line 13 (a), approximately north–south in the southern Adare Basin, shows velocity contours based on interpolation between five overlapping 1D velocity models. Depths of individual layers directly detected in the sonobuoy data ("x") indicate the positions of the sonobuoys; velocities are uncertain to ±100 m/s, depths up to ±0.4 km (increasing with depth). Note that velocity contours are flat, and reveal a crustal structure consistent with the eastern ends of Transects 2 and 3 (Figures 4 and 5), and with the gravity-based crustal thickness estimate of 5 – 6 km to the north [*Müller et al*., 2005]. 1D velocity models are arranged in order of their position in the 2D model (b – f).

Deep structure across the continental shelf and in the Northern Basin

The deep crustal structure of the continental shelf and the Northern Basin are explored in detail, since overlapping sonobuoys along MCS Lines 14 – 19 (see Figure 2) allow for construction of three more 2D velocity models. Line 14 strikes northeast to southwest, approximately perpendicular to the trend of the continental shelf between the Adare and Northern Basins that it crosses over, while Line 15 doubles back on the half of Line 14 that is up on the continental shelf. Line 17 similarly doubles back on Line 16, crossing Lines 14 and 15 at a right angle, up on the shelf of the Northern Basin. Line 19 runs parallel to Lines 16 and 17, and crosses Lines 14 and 15 another ~20 km further southwest in the Northern Basin.

The 2D velocity model that crosses the continental shelf, constructed from fourteen sonobuoys along Lines 14 and 15, shows remarkably flat velocity contours, within depth uncertainties (Figure 8a), similar to the 2D velocity model along Line 13. Depths of deeper velocity contours (up to ~5000 m/s) agree between the two models (within uncertainty), but the 6000 m/s velocity contour is ~4.0 km below the seafloor along Lines 14 and 15, ~0.7 km deeper than the same contour along Line 13 (i.e.. a greater difference than the uncertainty of ±0.4 km). The only potential detection of the Moho in this study lies at the beginning of Line 14 (L14S1, at 175.2° E, 71.9° S; Figure 8b), where a velocity of 8000±100 m/s is observed at a depth of 5.5±0.4 km below the seafloor.

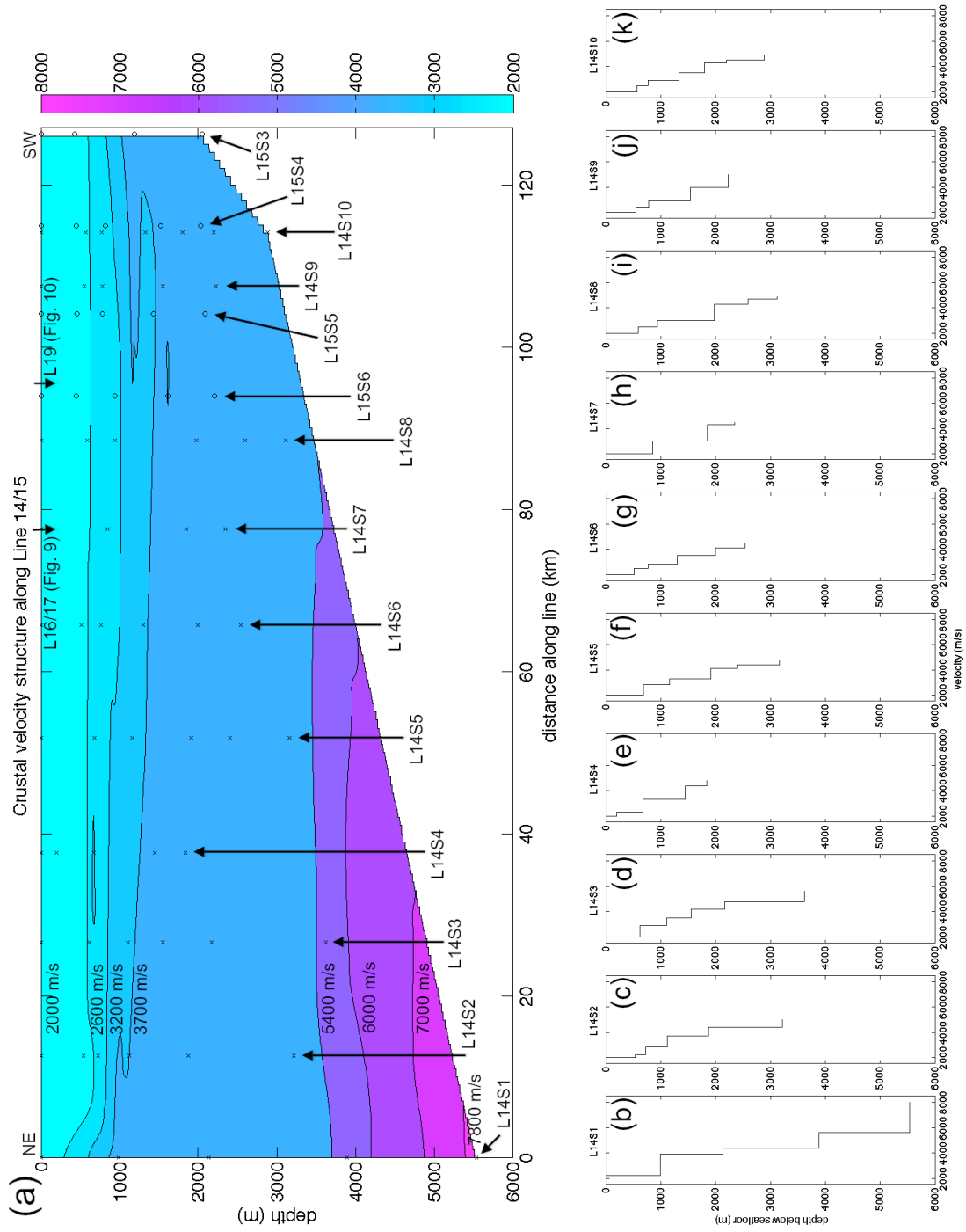

Figure 5.8a – k. See caption on the following page.

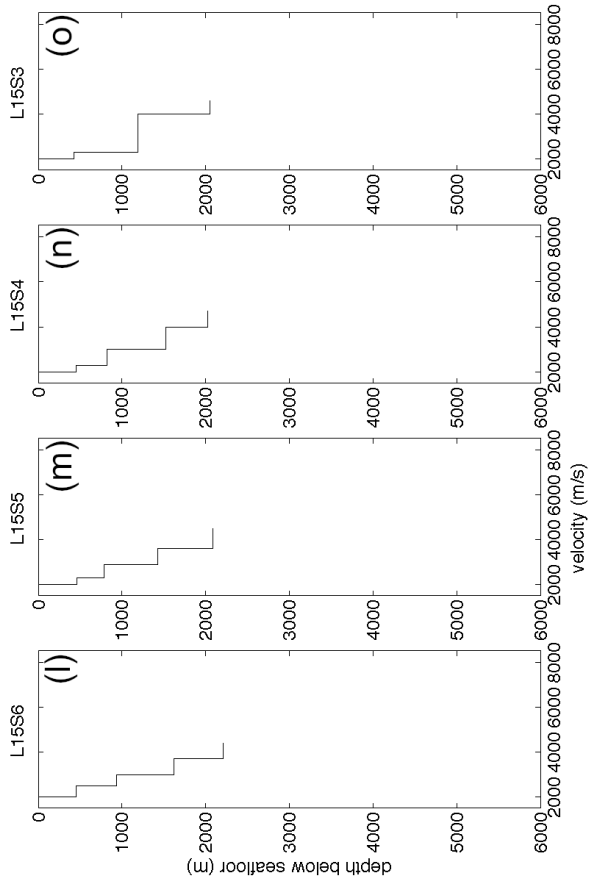

Figure 5.8. A 2D velocity model along Lines 14 and 15 (a), crossing the continental shelf from the Adare Basin to Northern Basin, shows velocity contours based on interpolation between fourteen overlapping 1D velocity models. Depths of individual layers directly detected in the sonobuoy data ("x" for Line 14, "o" for Line 15) indicate the positions of the sonobuoys; velocities are uncertain to ±100 m/s, depths up to ±0.4 km (increasing with depth). Note that velocity contours are flat, and reveal a crustal structure consistent with the southern end of Line 13 (Figure 8), as defined by head wave detections beneath the continental shelf (to ~45 km along the line), suggesting deep structural continuity between the two basins. While maximum velocities of up to 5000 m/s are detected in the Northern Basin, a head wave with 8000 m/s is detected at 5.5 km below the seafloor at the shelf break (L14S1); this is consistent with the gravity-based crustal thickness estimate of 5 – 6 km east of the Adare Trough [*Müller et al*., 2005], suggesting the oceanic crust of the Adare Basin extends south to at least 71.9° S. 1D velocity models are arranged in order of their position in the 2D model, in separate rows for Lines 14 (b – k) and 15 (l – o).

Of the other sonobuoys along Lines 14 and 15 (Figures 8c – o), only four more detect layers >3.0 km below the seafloor, with the deepest being 3.6 km (L14S3; Figure 8d). Maximum layer velocities along Lines 14 and 15 are generally 4400 – 5000 m/s, with L14S1 (8000 m/s) and L14S3 (5600 m/s) being the only exceptions. Consequently, while the higher velocity contours (>5400 m/s) in the 2D velocity model for Lines 14 and 15 are constrained by multiple head wave detections along the scarp of the continental shelf (L14S1 – L14S3), they are not well constrained under the Northern Basin.

Eleven sonobuoys on Lines 16 and 17, and seven on Line 19, further reveal the crustal structure in the Northern Basin; these 2D velocity models cross the model constructed from Lines 14 and 15 in the Northern Basin (see Figure 8a for crossing points), where the highest maximum velocity measured in a sonobuoy is 5000 m/s, at 2.3 km below the seafloor (L14S9; Figure 8j). The 2D velocity model based on Lines 16 and 17 (Figure 9a) shows deep velocity contours that are approximately flat (3800 m/s and 4400 m/s, at ~1.8 km and ~2.2 km below the seafloor respectively), and a shallow velocity contour that sags in the middle of the line (2300 m/s, which ranges from 0 km to ~0.5 km below the seafloor). The northwesternmost end of this velocity model is constrained by a relatively high velocity at the seafloor of 2800 m/s and relatively low velocity for a depth of 1.4 km (of 3000 m/s, see L17S2 in Figure 9b), which acts to deflect velocity contours away from their otherwise relatively smooth lateral horizons, as defined by the remaining sonobuoys (Figures 9c – l).

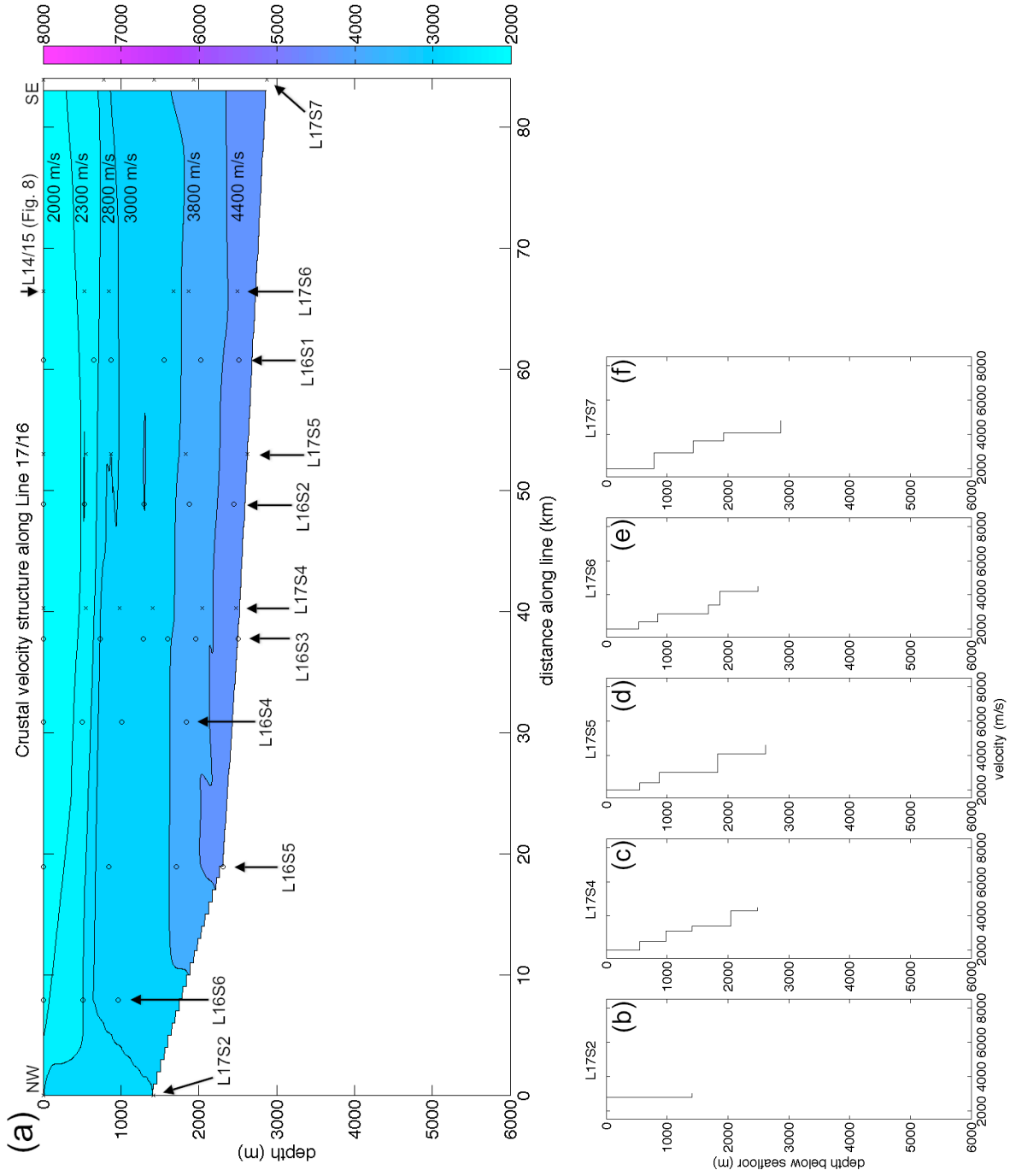

Figure 5.9a – f. See caption on the following page.

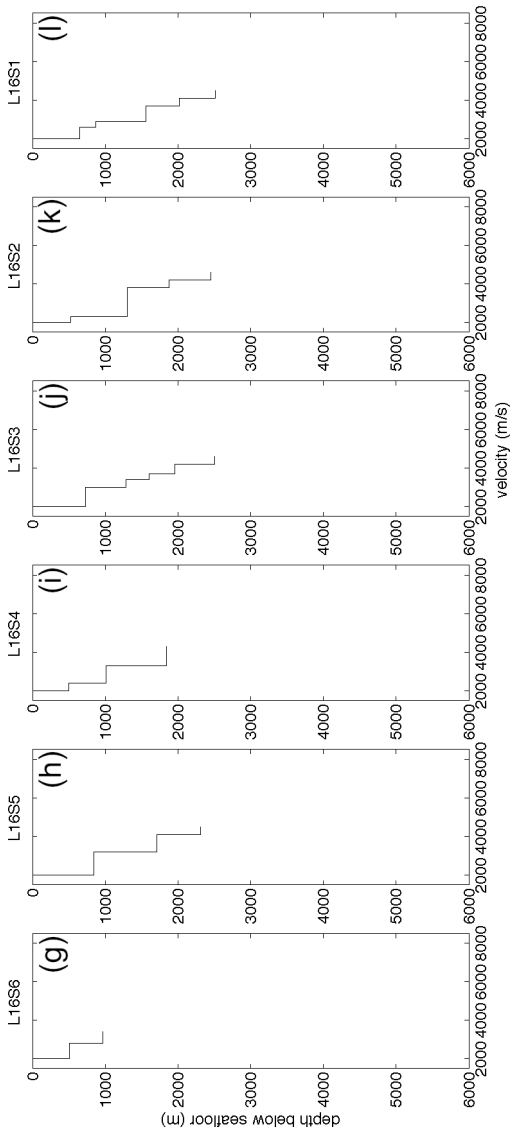

Figure 5.9. A 2D velocity model along Lines 16 and 17 (a), in the Northern Basin, shows velocity contours based on interpolation between eleven overlapping 1D velocity models. Depths of individual layers directly detected in the sonobuoy data ("x" for Line 17, "o" for Line 16) indicate the positions of the sonobuoys; velocities are uncertain to ±100 m/s, depths up to ±0.4 km (increasing with depth). Note that velocity contours are generally flat, and reveal a crustal structure consistent with Lines 14 and 15 (Figure 8) where they cross. One deviation from flat contour lines is the downward deflection of the 2300 m/s contour in the middle of the line. The other is at the northwestern-most end of the line, where sonobuoy L17S2 (b) detects a nearly constant velocity of ~2900 m/s from the seafloor to a depth of 1.4 km; this location coincides with the magnetic anomaly that runs along the west side of the Northern Basin (see Figure 2b). 1D velocity models are arranged in order of their position in the 2D model, in separate rows for Lines 17 (b – f) and 16 (g – l).

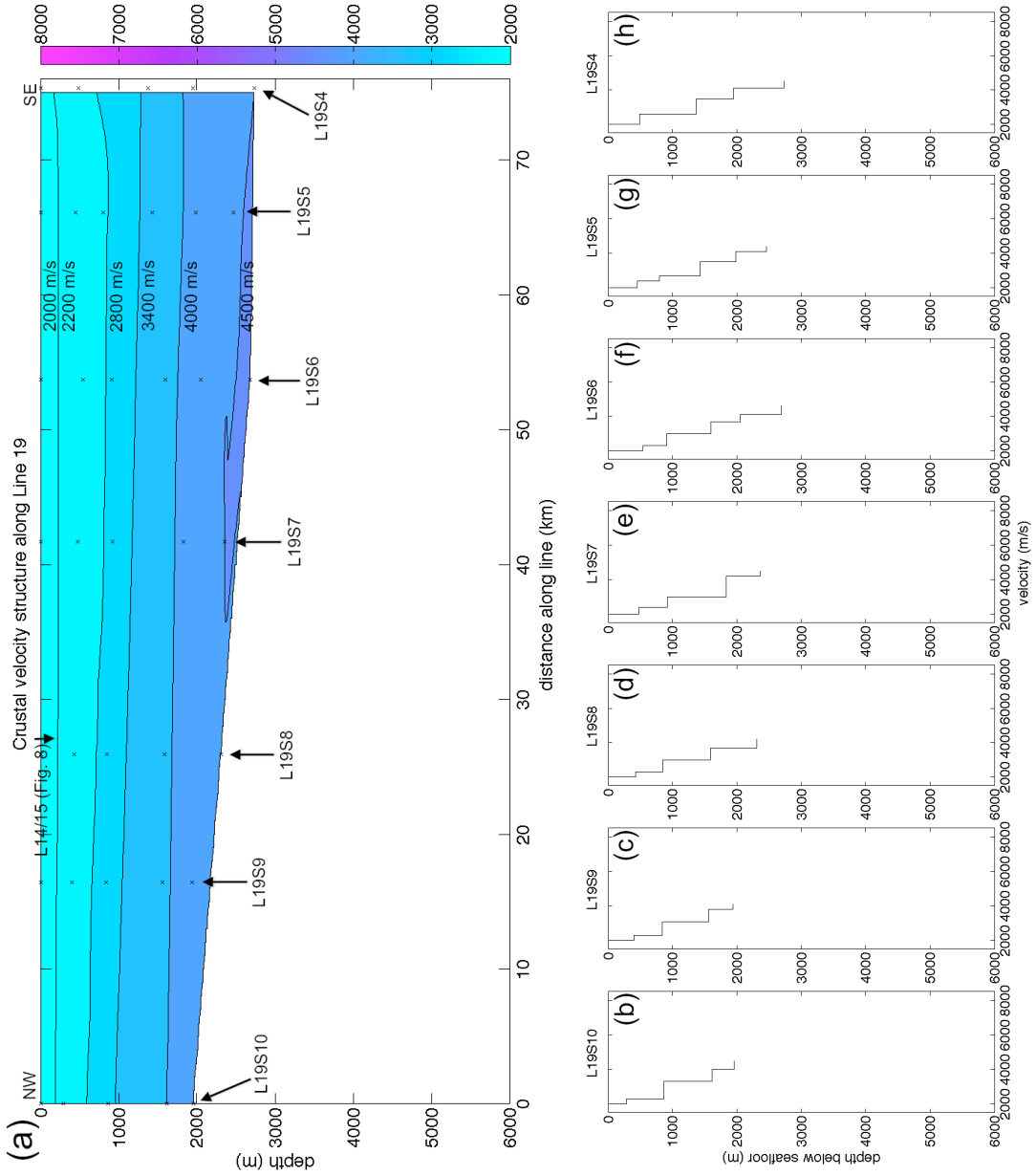

Figure 5.10. A 2D velocity model along Line 19 (a), ~20 km southwest of Lines 16 and 17 in the Northern Basin, shows velocity contours based on interpolation between seven overlapping 1D velocity models. Depths of individual layers directly detected in the sonobuoy data ("x") indicate the positions of the sonobuoys; velocities are uncertain to ±100 m/s, depths up to ±0.4 km (increasing with depth). Note that velocity contours are flat, and reveal a crustal structure consistent with that of Lines 16 and 17 (Figure 9) where they overlap, and Lines 14 and 15 (Figure 8) where they cross. 1D velocity models are arranged in order of their position in the 2D model (b – h).

The velocity contours in the 2D velocity model along Line 19 (Figure 10a) are flat, depicting horizons with velocities up to 4500 m/s (at ~2.5 km below the seafloor). These contours are in agreement with the model derived from Lines 16 and 17, for the portions of each that line up (see Figures 9a and 10a), and both are in good agreement with their crossing points on the model derived from Lines 14 and 15. Individual sonobuoys along Line 19 have highest maximum velocities of 4100 – 4600 m/s at >3.0 km below the seafloor (Figures 10b – h), similar to most sonobuoys in the Northern Basin (see Table 1).

Discussion

Adare Basin

Sonobuoy L12S1 on the west end of Transect 1 (Figure 3b) and the four along Line 9 (Figures 6a – d) demonstrate the overall character on both sides of the Adare Trough of simple crustal structure (i.e., few layers) and shallow high-velocity layers. In comparison, south of the trough the deep crustal structure is more complex (i.e., sonobuoys detect more layers), with deeper high-velocity layers (e.g., Figures 4b, 4d, 5b – d; also see Table 1). This suggests thinner and less tectonically deformed crust along the flanks of the trough than in the portion of the Adare Basin between the trough and the Northern Basin.

Overlapping sonobuoys along Line 13 (Figure 7) display this trend in the crustal structure of the southern Adare Basin; starting ~50 km north of the continental shelf remains, layers in the crust are detected to similar maximum depths (2.7 – 3.5 km below the seafloor), highest maximum velocities indicative of intrusive rock (5400 – 6600 m/s), and with four to six layers detected by each sonobuoy. These high velocities suggest basement rock and perhaps lower oceanic crust (i.e., gabbro, typically 6000 – 7000 m/s [e.g. *Jones*, 1999, p. 64]) at relatively shallow depths below the

seafloor. Similar layer velocities at even shallower depths on either side of the Adare Trough (1.3 – 2.3 km) suggest a similar oceanic crustal structure in the northern Adare Basin, but with less sediment than at its southern end. Overall, Line 13 reveals flat velocity contours, further suggesting that the deep north–south structure on the east side of the Adare Basin consists of laterally continuous layers, with little to no deformation.

However, Transects 1 – 3 reveal variation in deep crustal structure throughout the basin. Basement rock is deeper under the axis of the trough than on its flanks, as evidenced by the downward deflection of the 4600 m/s contour in the middle of Transect 1 (Figure 3). This transect is not within the isopach contours of sediment thickness as determined in the Adare Basin using NPB0701 MCS data, but the trend of greater sediment thickness within the trough than on its flanks holds true south of Transect 1 (see Figure 13c in Granot et al. [2010]).

Further south, Transect 2 reveals structural asymmetry. The low-velocity crust (2000 – 4000 m/s) is thicker west of the Adare Trough than on its eastern side, with the lowest-velocity layers (2000 – 3000 m/s) significantly thicker to the west. These results are consistent with sediment thicknesses determined from MCS data [*Granot et al.*, 2010], at the locations of the sonobuoys used to construct Transect 2. The velocity contour of 6000 m/s at ~2.3 km below the seafloor also shows that high crustal velocities are relatively shallow on either side of the southernmost extent of the Adare Trough, where it changes azimuth.

At the southernmost extent of the Adare Basin, along the base of the continental shelf, Transect 3 suggests thicker crust to the west than to the east, with crust thicker overall than along the northern two transects. The middle sonobuoy (L12S6) detects a layer velocity of 5300 m/s at 4.3 km below the seafloor, while sonobuoys on either end of the transect detect a slightly higher velocity at slightly shallower depths (5700 m/s, at 4.1 km to the west and 2.8 km to the east). Transect 3 suggests a thicker crust along the shelf break than north around the Adare Trough, as well as east–west variation in crustal thickness along the edge of the shelf.

Having variable depths for velocities >5500 m/s, as well as velocities of 7000 – 7400 m/s in three locations, and at fairly shallow depths (in sonobuoys L2S2, L7S1, and L7S2; see Figures 6e and 4d for the latter two), suggests variation in crustal thickness throughout the Adare Basin. The detections of 7000+ m/s velocities suggests that this crust is oceanic, as expected from the great water depth. However, crustal thickness in the Adare Basin cannot be determined using this data, since the Moho is not directly detected. Variable crustal thickness would also be consistent with variable sediment thickness in the Adare Basin, particularly due to basement highs along the scarps that border the Adare Trough [*Granot et al.*, 2010].

Structure across the continental shelf

Two distinct features stand out in the crustal structure across the margin between the Adare and Northern Basins (Figure 8a). One is the thickness of the crust under L14S1, which reveals a maximum velocity of 8000 m/s, a velocity that is routinely interpreted as the Moho. The other obvious feature is the overall flat trend of velocity contours along Lines 14 and 15.

Measuring a velocity of 8000±100 m/s at 5.5±0.4 km below the seafloor implies a thin crust at this location, for a minimum of 10 km along the trend of L14S1. If we assume this velocity is in fact 7900 m/s, its lower bound within uncertainty, and calculate the dip on that interface that would result in an apparent velocity of 8000 m/s, we get the fairly large value of 9°. In order for this to be the case, it would imply an interface that is still planar for several kilometers, in order to return the coherent linear head wave observed in the data, but oriented at a significant tilt upward toward the Northern Basin. It is possible that there is an interface in the lower crust (with a velocity of 7900 m/s) with such relief on the local scale, but this would still imply unusually thin crust, since a velocity of 7900 m/s is generally observed only in the deepest portion of the oceanic crust [e.g., *Jones*, 1999, p. 289]. If the true maximum velocity detected with sonobuoy L14S1 is 7900 m/s, it

is also possible that the interface is in fact the Moho, but with serpentinized mantle such as is observed in the Svalbard continental margin [*Ritzmann et al.*, 2004].

The resulting topography in the lower crust would be surprising in the context of the local bathymetry. The sharp relief at this shelf break suggests a lateral transition from oceanic to continental crust, which is usually confirmed at depth when velocity contours are observed to deflect downward under the thicker continental crust. The hypothetical dip of 9° would not only be in the opposite sense as expected for a transition from oceanic to continental crust, but would be in contrast to the general trend of velocity contours observed along Lines 14 and 15, which are indistinguishable from flat horizons.

Although no previous studies of crustal thickness along this portion of the Ross Sea continental shelf exist, some estimates of crustal thickness have been made within each basin, using gravity data to determine Moho depth. Models of mantle Bouguer anomalies in the Adare Basin indicate crustal thicknesses of 10.5 km to 9 km along the Adare Trough axis, from its north (~69.8° S) to south (~70.6° S), and 6 km to 5 km at similar latitudes to the east of the trough [*Müller et al.*, 2005]. Müller et al. [2005] conclude that the crust is anomalously thick in the vicinity of the Adare Trough, implying that the crustal thickness to its east (5 – 6 km) is typical of the Adare Basin. This estimate of crustal thickness is consistent with our calculated value at L14S1 of 5.5 km, indicating that the crust at this sonobuoy location is similar in structure to the oceanic crust of the Adare Basin.

Crystalline crust thickness contours within the portion of the Ross Sea assumed to be continental crust were estimated using gravity and seismic data, to respectively determine Moho and basement depths; in the Northern Basin, ~12 km of crystalline crust is estimated to underlie sediment [*Davey and Brancolini*, 1995]. Davey and Brancolini [1995] interpret the deep Northern Basin structure as stretched continental crust, assuming it was originally 30 – 40 km thick and stretched by >100%. This estimate of crustal thickness is much greater than our estimate of 5.5 km at the base of the

continental shelf (particularly since our estimate includes sedimentary and crystalline rock), and may indicate that a transition in crustal type from the Adare Basin to Northern Basin occurs south of L14S1.

On the other hand, this study suggests a continuity of crustal type across the continental shelf, since we see no deflection of velocity contours downward under the Northern Basin (Figure 8a), as expected at the transition between oceanic and continental crust. Continuity between Adare and Northern Basin crust is also suggested by two thick, linear magnetic anomalies along the sides of the Northern Basin, which appear to be extensions of anomalies 16 – 18 as they are oriented on either side of the Adare Trough [*Cande and Stock*, 2006; *Damaske et al.*, 2007]; Cande and Stock [2006] suggest that these anomalies may be the result of massive intrusions that helped accommodate extension in the Northern Basin. It is also possible that the crystalline crust of the Northern Basin is either oceanic crust, or a region of transitional crust as inferred between oceanic and continental crust in the Gulf of California [*Oskin et al.*, 2001].

Northern Basin

This study indicates that the Northern Basin is filled with approximately horizontal sediment horizons (Figure 8 – 10), consistent with MCS data [*Brancolini et al.*, 1995; *Granot et al.*, 2010], potentially to a depth of >3 km, if maximum velocities of 4100 – 5000 m/s can be attributed to relatively high-velocity sediment (consistent with interpretation of similar velocities, and basement depths of up to 3.0 km, to the south and east of our study [*Cooper et al.*, 1987; *Houtz and Davey*, 1973]). This is similar to the top 3 km of crustal structure imaged in the western portion of Transect 3, at the base of the continental shelf (Figure 5). Velocity contours in the Northern Basin suggest an only slightly thicker low-velocity portion of the crust than is imaged along Line 13, where a velocity contour of 4900 m/s is at a consistent depth of ~2.2 km below the seafloor (Figure 7).

Two exceptions to the generally flat velocity contours observed in the Northern Basin are a slight down-warping of the 2300 m/s contour along the axis of the basin and close to the continental shelf (see Figure 9a), and a nearly constant crustal velocity of ~2900 m/s for the entire 1.4 km crustal depth imaged by sonobuoy L17S2 (Figure 9b). While the magnetic anomaly along the west side of the Northern Basin (see Figure 2b) does lie approximately under sonobuoys L17S2 and L16S6 (Figure 9g), only L17S2 detects such a different crustal structure from the rest of the sonobuoys in the Northern Basin. However, sonobuoy L16S6 is similar to L17S2 in that it also detects layer interfaces to an anomalously shallow depth (1.0 km below the seafloor) compared to the rest of the sonobuoys in the Northern Basin. These shallow penetration depths may indicate disrupted crust below this depth, as would likely occur during massive intrusions.

Comparison to similar crust around the world

Ultraslow spreading zones such as the Adare Trough (~12 mm/yr full-spreading rate [*Cande et al.*, 2000]) are typically associated with thin oceanic crust. The traditional view of oceanic crustal structure was determined from studies of ophiolite suites on land and marine seismic data, both of which indicated subhorizonal layering beneath the sediment–basement contact of basaltic pillow lavas (v_p ~5000 m/s), sheeted dikes, gabbro (v_p ~7000 m/s), and peridotite mantle (v_p ~8000 m/s), with mean oceanic crust (composed of basalt and gabbro) being ~7 km thick [e.g., *Christensen*, 1978]. In situ studies of these layers reveal that the oceanic crust has much greater complexity and variability [*Karson*, 1998; *Dick et al.*, 2003]. Fault scarps on the seafloor indicate devations from mean oceanic crustal structure on the scale of tens of meters to tens of kilometers, particularly along slow spreading ridges and in magma-poor locations, where stretching and thinning of the lithosphere often results in crust <7 km thick and the presence of oceanic core complexes (exposed along low-angle detachment faults, where rock units missing, and contacts between units that are neither horizontal or continuous) [*Karson*, 1998].

Peridotites are found along ultra-slow (≤12 mm/yr) spreading ridges [*Dick et al*., 2003], indicating that even mantle rock can be exhumed in these situations. Modeling of the detachment faulting process and resulting crustal thickness at spreading ridges, based on differing amounts of tectonic and magmatic crustal formation in both the upper (basalt) and lower (gabbro) oceanic crust [*Olive et al*., 2010], indicates that our measured crustal thickness of 5.5 km at the continental margin (2.1 km sediment and 3.4 km basement rock) is consistent with the formation of an oceanic core complex along a detachment fault at a slow-spreading ridge, in the case where half of the extension is accommodated through crustal thinning and half through magmatism. The high velocities we measure at shallow depths along the eastern side of the Adare Trough (6000 – 7400 m/s, at 1 – 3 km below the seafloor) are also consistent with scenarios of oceanic core complex formation as modeled by Olive et al. [2010].

The crust around the arctic Gakkel Ridge (6 – 13 mm/yr full-spreading rate) reduces to thicknesses of 1.9 – 3.3 km along the ridge [*Jokat et al.*, 2003], while thicknesses of 2.5 – 5.4 km [*Minshull et al.*, 2006; *Müller et al.*, 2000] are observed along the Southwest Indian Ridge (11 – 18 mm/yr [*Chu and Gordon*, 1999]). Since gravity-derived thicknesses east of the Adare Trough (5 – 6 km) are similar to those along the Southwest Indian Ridge, the crustal thickness along the trough axis (9 – 10.5 km) suggests that some process that occurred late in the spreading history of the Adare Basin considerably thickened the crust along-axis [*Müller et al.*, 2005].

MCS data from NBP0701 show faulting in the shallow crust from ~17 Ma that follows the trend of the Adare Trough axis south to the continental shelf [*Granot et al.*, 2010]. The edges of the deformed zone approximately correspond to sonobuoys L8S2 and L12S6 (on Transect 3, see Figure 5), which suggest a thicker sedimentary package than other sonobuoys in the Adare Basin; the zone of deformation from ~17 Ma roughly coincides with the thickest Adare Basin sediments imaged with the MCS data [*Granot et al.*, 2010]. It may be that the general trend of thicker crust under the axis of the Adare Trough and thinner crust in the flanking portions of the Adare Basin [*Müller et al.*, 2005] holds as far south as the continental shelf.

This overall trend is consistent with the crustal structure detected by sonobuoys along Lines 9 and 13 (Figures 6 and 7), as well as sonobuoys L7S1 and L7S2 (Figures 6e and 4d), where high crustal velocities (up to 7400 m/s) are detected at relatively shallow depths in the crust. It is also consistent with a crustal thickness of 5.5 km observed in the sonobuoy L14S1 data (Figure 8), which lies at the base of the continental shelf along the same north–south trend. If this trend in crustal structure of thick along the trough axis and thin along the trough flanks holds for the entire Adare Basin, it suggests that most of the Adare Basin crust is thin relative to mean oceanic crust, consistent with oceanic core complexes observed and modeled at ultra-slow spreading ridges.

The structure we observe in the Northern Basin (Figures 8 – 10) is more challenging to interpret, since we only observe a range of velocities indicative of sediment (2000 – 5000 m/s), with velocities of 4000 – 5000 m/s at a maximum depth of ~3 km. While the deep, high velocity contours (5400 – 7800 m/s) observed across the continental shelf (Figure 8) are flat and suggest a continuation of deep crustal structure from the Adare Basin into the Northern Basin, we are not able to confirm this same structure in sonobuoys within the Northern Basin.

Instead, the Northern Basin crust may be composed primarily of stretched continental crust, as observed in basins and continental margins in other parts of the world. Continental margins and basins in the North Atlantic exhibit several features typical of magma-starved continental extension, including thinning by up to a factor of 10 in basins, tapering of crustal thickness in margins, and exhumation and serpentinization of continental mantle [e.g., *Whitmarsh et al*., 2001; *O'Reilly et al*., 1996; *Osmundsen and Ebbing*, 2008]. Wide-angle seismic data along and across the Rockall Trough, a basin northwest of Ireland, reveals 5 – 7 km thick crust under the trough that is the result of differential stretching of the 20 – 30 km thick crust under the Ireland margin, where the upper crust has been stretched by a factor of 8 – 10 and the lower crust by a factor of 2 – 3 [*O'Reilly et al*., 1996]. Below the Moho is a 3 – 10 km thick layer of serpentinized peridotite; hydrated mantle is found at continental margins as well, underlying even thinner crust in the

Iberian margin (tapering from ~7 km to <400 m [*Whitmarsh et al.*, 2001]) and the Møre and Vøring basins in the mid-Norway margin (2 – 12 km [*Osmundsen et al*., 2008]).

Crustal thickness in the Northern Basin is estimated from gravity data to be ~12 km thick [*Davey and Brancolini*, 1995]. This value is consistent with its tectonic setting, at the edge of the continental shelf of the Ross Sea. If the Northern Basin crust is indeed ~12 km thick (~15 km including sediment), it is similar to total crustal thicknesses (including sediment) of 16 – 19 km in southern Ross Sea basins [*Trehu et al*., 1993; *Trey et al*., 1999], and likely of similar origin (stretched continental crust). If the Northern Basin is in fact thinner (i.e., more similar to our measured value of 5.5 km at the continental margin, 3.4 km of which is basement rock), it may be continental crust that has been severely thinned, and of a similar tectonic origin to the continental margins in the North Atlantic discussed above. This could have been due to being pinned to extension in the Adare Basin, which may have been accompanied by massive intrusions, particularly under magnetic anomalies along the east and west edges of the basin [*Cande and Stock*, 2006]. Such transitional crust is also observed in a similar tectonic setting in the Gulf of California [*Oskin et al.*, 2001]. Support for the presence of magmatic activity as well comes from the anomalously shallow penetration depth of the two sonobuoys that lie on top of the western magnetic anomaly (L16S6 and L17S2, see Figure 9), which suggest disruption of the generally flat velocity contours interpolated from all other sonobuoys in the Northern Basin.

Conclusions

Sonobuoy data in the Adare Basin suggest particularly thin oceanic crust along the east side of the Adare Trough, consistent with estimates of 5 – 6 km thickness based on gravity data [*Müller et al.*, 2005]. Sonobuoys also suggest slightly thicker crust within the Adare Trough and at the base of the continental shelf, in particular at the south end of the thicker sediments and shallow deformation that are both associated with the Adare Trough [*Granot et al.*, 2010]. This is again consistent with

gravity-based estimates [*Müller et al.*, 2005]. Detection of a head wave velocity of 8000 m/s, interpreted to be the Moho at 5.5±0.4 km below the seafloor, by a sonobuoy at the continental shelf (L14S1), suggests that typical Adare Basin crustal thicknesses of 5 – 6 km may extent as far south as the continenal shelf.

Overlapping sonobuoys across the continental shelf reveal deep velocity structure with flat contours, suggesting that the deep crustal structure of the Northern Basin may be similar to, and perhaps even continuous with, that of the Adare Basin. However, sonobuoys within the Northern Basin do not detect head wave velocities >5000 m/s, and so mainly illustrate the flat velocity contours of the sedimentary rock filling the basin. The northwesternmost sonobuoys in the Northern Basin are anomalous in terms of how shallowly they penetrate the crust, which may be due to disruption of sediments by massive intrusions. These results for the Northern Basin deep crustal structure are consistent with the idea of a transitional crustal type [*Cande and Stock*, 2006], but cannot rule out the possibility that the deep Northern Basin crust is simply stretched continental crust, similar to other basins in the Ross Sea.

By using the results of this study to constrain crustal velocity structure, analysis of shipboard gravity and multibeam bathymetry collected during research cruise NBP0701 may better constrain crustal thickness throughout the Adare and Northern Basins. In order to directly image the Moho in this area, it may be necessary to use an ocean-bottom seismic experiment, which would provide greater penetration into the crust.

Table 5.1. Velocity model values and locations for sonobuoys deployed during research cruise NBP0701 (see Figure 2 for mapped locations). Sonobuoys are labeled according to multi-channel seismic line (L1 – L19) and sonobuoy number along each line; although 89 sonobuoys were deployed, only the 71 listed have the large offsets and good quality data needed for detection of deeper crustal structure. Columns contain the depth (*d*, in m) and velocity (*v*, in m/s) for each layer, as derived from the sonobuoy data. A 6-gun G/I source array was used along lines 1 – 12, and a 6-element Bolt-fun array was used along lines 13 – 19 (see text for details). Uncertainty on velocity is ±100 m/s, and on depth is ±100 – 400 m (increasing with depth).

	1 (H_20)	2	3	4	5	6	7	8	Lon/ Lat
L1S3: *d*	0	2260	3040	3380	3600	4130	4590		171.879
v	1450	2000	2100	2300	4500	5200	5500		-70.936
L2S1: *d*	0	2150	2680						173.492
v	1450	2000	2900						-71.014
L2S2: *d*	0	2320	2920	3790	5330				173.034
v	1450	2000	2300	4400	7200				-71.058
L2S4: *d*	0	2210	2960						172.745
v	1450	2000	3000						-71.268
L2S5: *d*	0	2050	2830	4030					173.193
v	1450	2000	3700	4100					-71.239
L3S2: *d*	0	2320	3820	5370					173.136
v	1450	2000	3700	5000					-70.592
L3S3: *d*	0	2470	3770	4730					172.966
v	1450	2000	3100	4800					-70.405
L4S2: *d*	0	2180	3080	3740	4450	5460	6610		174.670
v	1450	2000	3200	4300	4900	6000	6900		-71.340
L4S3: *d*	0	1920	2870	3990	4920				173.098
v	1450	2000	3200	4500	5200				-71.448
L4S4: *d*	0	400	560	850					171.753
v	1450	2000	4500	5600					-71.595
L4S5: *d*	0	1830	2910	4090					172.990
v	1450	2000	2500	6000					-71.632
L4S6: *d*	0	2180	2980	3650	4380	5370			174.561
v	1450	2000	3100	4100	4600	6100			-71.503
L5S2: *d*	0	510	810	1370	1970	2640			173.832
v	1450	2000	2300	2900	3600	4400			-72.386
L5S3: *d*	0	1970	2850	3300	4600	5290	6460		173.847
v	1450	2000	3200	3600	4200	5200	6700		-71.801
L6S1: *d*	0	2150	3290						173.947
v	1450	2000	5100						-70.780
L6S2: *d*	0	2390	3590						173.219
v	1450	2000	3000						-70.758
L6S3: *d*	0	2140	3090	3740	4480				172.175
v	1450	2000	3100	4500	5400				-70.845
L7S1: *d*	0	2300	2930	3250	3960	5440			174.474
v	1450	2000	2400	2800	4800	7000			-70.928
L7S2: *d*	0	2180	3670	4560	5390				174.249
v	1450	2000	4700	6000	7400				-71.059

L7S3: *d*	0	1910	2880	4470	4740	5610			172.536
v	1450	2000	3300	4600	5300	6000			-71.390
L8S1: *d*	0	2140	2890	3570	4570	5230			174.283
v	1450	2000	2100	4300	5400	5900			-71.276
L8S2: *d*	0	2050	3020	3600	4190				174.369
v	1450	2000	3500	3800	4600				-71.700
L8S3: *d*	0	1760	2830	5110	5320	5880			172.862
v	1450	2000	3700	4600	5000	5700			-71.817
L9S1: *d*	0	3230	3974						173.436
v	1450	2000	6800						-69.003
L9S2: *d*	0	3010	3660	4300					174.000
v	1450	2000	4900	5900					-69.589
L9S3: *d*	0	2050	3330	4090					174.223
v	1450	2000	4600	5400					-70.473
L9S4: *d*	0	2320	3720						174.370
v	1450	2000	6000						-70.749
L10S1: *d*	0	2070	3110	3200	3850				173.957
v	1450	2000	2200	2500	3700				-71.353
L12S1: *d*	0	2250	3250	4720					171.644
v	1450	2000	4100	6200					-70.711
L12S2: *d*	0	2200	3360	3980	5060				171.872
v	1450	2000	2500	5500	6500				-70.881
L12S4: *d*	0	2170	2980	3820	5630				172.780
v	1450	2000	3100	4800	6700				-71.223
L12S5: *d*	0	1910	2780	3300	4130	6830			173.037
v	1450	2000	3000	3300	5000	6400			-71.450
L12S6: *d*	0	1920	2670	2780	2980	3460	4510	6240	173.541
v	1450	2000	2200	2800	3500	3800	4600	5300	-71.824
L13S2: *d*	0	2200	2960	3900	4110	4960	5740		174.714
v	1450	2000	3000	3600	4400	5000	6300		-71.291
L13S3: *d*	0	2150	2980	3750	4460	5540			174.776
v	1450	2000	3100	3700	5000	6000			-71.346
L13S4: *d*	0	2210	2960	3780	4520	5510			174.926
v	1450	2000	3200	4000	4600	5400			-71.520
L13S5: *d*	0	2100	3010	4450	5410				175.037
v	1450	2000	3600	5500	6600				-71.648
L13S6: *d*	0	2050	3020	4100	4880				175.115
v	1450	2000	3700	4500	5700				-71.740
L14S1: *d*	0	1960	2950	4090	5850	7500			175.182
v	1450	2200	3900	4400	5600	8000			-71.862
L14S2: *d*	0	1780	2320	2520	2910	3660	5000		174.975
v	1450	2000	2200	2800	3700	4400	5000		-71.956
L14S3: *d*	0	1510	2130	2620	3060	3680	5130		174.735
v	1450	2000	2900	3500	4200	4800	5600		-72.057
L14S4: *d*	0	1160	1460	1800	2600	2990			174.553
v	1450	2000	2300	3300	4400	4800			-72.140
L14S5: *d*	0	520	1200	1680	2440	2930	3690		174.313
v	1450	2000	2800	3300	4100	4400	4700		-72.243

L14S6: *d*	0	500	1010	1270	1800	2500	3040		174.072
v	1450	2000	2500	2800	3500	4100	4500		-72.345
L14S7: *d*	0	470	1320	2320	2820				173.863
v	1450	2000	3000	4300	4500				-72.431
L14S8: *d*	0	440	1030	1390	2420	3040	3560		173.672
v	1450	2000	2500	3000	4300	4700	4900		-72.510
L14S9: *d*	0	470	1020	1250	2020	2700			173.333
v	1450	2000	2400	2900	4000	5000			-72.648
L14S10:*d*	0	460	1030	1230	1790	2260	2660	3350	173.219
v	1450	2000	2500	2900	3500	4300	4500	4900	-72.697
L15S3: *d*	0	490	920	1680	2540				172.983
v	1450	2000	2300	4000	4600				-72.781
L15S4: *d*	0	470	920	1290	2000	2500			173.197
v	1450	2000	2300	3000	4000	4700			-72.702
L15S5: *d*	0	460	920	1250	1900	2550			173.402
v	1450	2000	2300	2900	3600	4500			-72.624
L15S6: *d*	0	470	920	1410	2090	2680			173.577
v	1450	2000	2500	3000	3700	4400			-72.550
L16S1: *d*	0	470	1120	1350	2030	2490	2980		173.742
v	1450	2000	2600	2900	3700	4100	4500		-72.404
L16S2: *d*	0	410	940	1710	2280	2860			173.446
v	1450	2000	2300	3800	4200	4600			-72.345
L16S3: *d*	0	490	1220	1770	2090	2440	2990		173.169
v	1450	2000	3000	3400	3700	4200	4600		-72.290
L16S4: *d*	0	510	1010	1520	2350				173.002
v	1450	2000	2400	3300	4300				-72.255
L16S5: *d*	0	480	1320	2190	2790				172.714
v	1450	2000	3200	4100	4500				-72.194
L16S6: *d*	0	430	940	1390					172.450
v	1450	2000	2800	3400					-72.137
L17S2: *d*	0	360	1770						172.258
v	1450	2800	3000						-72.097
L17S4: *d*	0	470	1020	1460	1880	2520	2950		173.233
v	1450	2000	2500	3100	3400	4300	4500		-72.303
L17S5: *d*	0	470	1020	1340	2300	3090			173.551
v	1450	2000	2400	3000	4100	4600			-72.365
L17S6: *d*	0	490	1020	1330	2160	2350	2980		173.883
v	1450	2000	2400	2900	3400	4200	4500		-72.432
L17S7: *d*	0	450	1230	1880	2380	3320			174.317
v	1450	2000	2900	3600	4100	4800			-72.519
L19S1: *d*	0	550	890	1360	1650	2200			175.714
v	1450	2000	2500	2700	3200	4100			-72.667
L19S4: *d*	0	370	860	1740	2320	3100			174.681
v	1450	2000	2600	3500	4100	4500			-72.761
L19S5: *d*	0	400	850	1200	1830	2380	2860		174.427
v	1450	2000	2400	2700	3500	4100	4400		-72.725
L19S6: *d*	0	410	950	1320	2000	2460	3090		174.084
v	1450	2000	2300	3000	3700	4100	4600		-72.678

L19S7: *d*	0	450	930	1370	2280	2810			173.783
v	1450	2000	2400	3000	4200	4500			-72.617
L19S8: *d*	0	490	920	1330	2070	2800			173.402
v	1450	2000	2300	3000	3700	4200			-72.533
L19S9: *d*	0	510	910	1350	2070	2450			173.171
v	1450	2000	2300	3100	3800	4100			-72.484
L19S10:*d*	0	520	810	1390	2130	2470			172.779
v	1450	2000	2300	3300	4000	4500			-72.395

Acknowledgements

We would like to thank Captain Mike Watson, the crew, and the Raytheon technical staff on board the *Nathaniel B. Palmer*. This study was supported by National Science Foundation grants OPP04-40959 (S. Cande) and OPP-0440923 and OPP-0944711 (J. Stock and R. Clayton).

References

Becker, J., and D. Sandwell (2006), SRTM30_PLUS: SRTM30, coastal & ridge multibeam, estimated topography, *Electronic journal,* http://topex.ucsd.edu/WWW_html/srtm30_plus.html.

Brancolini, G., A. K. Cooper, and F. Coren (1995), Seismic facies and glacial history in the western Ross Sea (Antarctica), *Antarctic Research Series*, *68*, 209-233.

Bruns, T., and P. Carlson (1987), Geology and petroleum potential of the southeast Alaska continental margin, *Geology and Petroleum Potential of the Continental Margin of Western North America and Adjacent Ocean Basins-Beaufort Sea to Baja California, Earth Science Series*, Houston, TX, 269.

Cande, S. C., and J. M. Stock (2004), Cenozoic reconstruction of the Australia-New Zealand-South Pacific sector of Antarctica, edited by N. F. Exon, J. K. Kennett and M. J. Malone, pp. 5-18, AGU, Washington, D.C.

Cande, S. C., and J. M. Stock (2006), Constraints on the timing of extension in the Northern Basin, Ross Sea, 9th International Symp. on Antarctic Earth Sci. Proceedings.

Cande, S. C., C. A. Raymond, J. Stock, and W. F. Haxby (1995), Geophysics of the Pitman Fracture Zone and Pacific-Antarctic plate motions during the Cenozoic, *Science*, *270*(5238), 947.

Cande, S. C., J. M. Stock, R. D. Müller, and T. Ishihara (2000), Cenozoic motion between east and west Antarctica, *Nature*, *404*(6774), 145-150.

Chu, D., and R. G. Gordon (1999), Evidence for motion between Nubia and Somalia along the Southwest Indian Ridge, *Nature*, *398*(6722), 64-67.

Christensen, R. B. (1978), Ophiolites, seismic velocities and oceanic crustal structure, *Tectonophysics, 47*, 131-157.

Cochrane, G. R., L. De Santis, and A. K. Cooper (1995), Seismic velocity expression of glacial sedimentary rocks beneath the Ross Sea from sonobuoy seismic-refraction data, *Geology and Seismic Stratigraphy of the Antarctic Margin, Antarctic Research Series*, *68*, 261-270.

Cooper, A. K., and F. J. Davey (1985), Episodic rifting of Phanerozoic rocks in the Victoria land Basin, western Ross Sea, Antarctica, *Science*, *229*(4718), 1085.

Cooper, A. K., F. J. Davey, and G. R. Cochrane (1987), Structure of extensionally rifted crust beneath the western Ross Sea and Iselin Bank, Antarctica, from sonobuoy seismic data, *The Antarctic Continental Margin: Geology and Geophysics of the Western Ross Sea, published by the Circum-Pacific Council of Energy and Mineral Resouces, Earth Science Series,* Houston, TX., 93-117.

Damaske, D., A. L. Laufer, F. Goldmann, H.-D. Moller, and F. Lisker (2007), Magnetic anomalies northeast of Cape Adare, northern Victoria Land (Antarctica), and their relation to onshore structures, 10th International Symp. on Antarctic Earth Sci. Proceedings.

Davey, F., and G. Brancolini (1995), The late Mesozoic and Cenozoic structural setting of the Ross Sea region, *Geology and Seismic Stratigraphy of the Antarctic Margin*, 167-182.

Dick, H. J. B., J. Lin, H. Schouten (2003), An ultraslow-spreading class of ocean ridge, *Nature, 426*(6965), 405-412.

Elliot, D. H. (1992), Jurassic magmatism and tectonism associated with Gondwanaland break-up: An Antarctic perspective, *Geological Society, London, Special Publications*, *68*(1), 165.

Gaina, C., D. R. M¸ller, J. Y. Royer, J. Stock, J. Hardebeck, and P. Symonds (1998), The tectonic history of the Tasman Sea: A puzzle with 13 pieces, *Journal of Geophysical Research*, *103*(B6), 12,413-12,433.

Gardner, G., L. Gardner, and A. Gregory (1974), Formation velocity and densityóthe diagnostic basics for stratigraphic traps, *Geophysics*, *39*, 770.

Geissler, W. H., and W. Jokat (2004), A geophysical study of the northern Svalbard continental margin, *Geophysical Journal International*, *158*(1), 50-66.

Granot, R., S. Cande, J. Stock, F. Davey, and R. Clayton (2010), Postspreading rifting in the Adare Basin, Antarctica: Regional tectonic consequences, *Geochemistry Geophysics Geosystems*, *11*(8), Q08005.

Hayes, D. E., et al. (1975a), Site 274, *Initial Rep. Deep Sea Drilling Proj., 28*, 369-433, doi: 10.2973/dsdp.proc.28.110.1975.

Hayes, D. E., et al. (1975b), Site 273, *Initial Rep. Deep Sea Drilling Proj., 28*, 335-367, doi: 10.2973/dsdp.proc.28.109.1975.

Houtz, R., and F. Davey (1973), Seismic profiler and sonobuoy measurements in Ross Sea, Antarctica, *Journal of Geophysical Research*, *78*(17), 3448-3468.

Jokat, W., O. Ritzmann, M. Schmidt-Aursch, S. Drachev, S. Gauger, and J. Snow (2003), Geophysical evidence for reduced melt production on the Arctic ultraslow Gakkel mid-ocean ridge, *Nature*, *423*(6943), 962-965.

Jones, E. J. W. (1999), *Marine Geophysics*, Wiley.

Karson, J. A. (1998), Internal structure of oceanic lithosphere: A perspective from tectonic windows, *Faulting and Magnatism at Mid-Ocean Ridges*, ed. R. Buck, 177-218.

Luyendyk, B., S. Cisowski, C. Smith, S. Richard, and D. Kimbrough (1996), Paleomagnetic study of the northern Ford Ranges, western Marie Byrd Land, West Antarctica: Motion between West and East Antarctica, *Tectonics*, *15*(1), 122-141.

Minshull, T. A., M. R. Müller, and R. S. White (2006), Crustal structure of the Southwest Indian Ridge at 66°E: seismic constraints, *Geophysical Journal International*, *166*(1), 135-147.

Molnar, P., T. Atwater, J. Mammerickx, and S. M. Smith (1975), Magnetic anomalies, bathymetry and the tectonic evolution of the South Pacific since the Late Cretaceous, *Geophysical Journal of the Royal Astronomical Society*, *40*(3), 383-420.

Müller, M., T. Minshull, and R. White (2000), Crustal structure of the Southwest Indian Ridge at the Atlantis II fracture zone, *Journal of Geophysical Research*, *105*(B11), 25809-25825,25828.

Müller, R. D., S. C. Cande, J. M. Stock, and W. R. Keller (2005), Crustal structure and rift flank uplift of the Adare Trough, Antarctica, *Geochemistry Geophysics Geosystems*, *6*(11).

NBP0701 Data Report (2007), prepared by J. Ayers, http://www.marine-geo.org/tools/search/data/field/NBPalmer/NBP0701/docs/NBP0701Report.htm.

Olive, J. A., M. D. Behn, B. E. Tuckolke (2010), The structure of oceanic core complexes controlled by the depth distribution of magma emplacement, *Nature Geoscience, 3*(7), 491-495.

Oskin, M., J. Stock, and A. MartÌn-Barajas (2001), Rapid localization of Pacific-North America plate motion in the Gulf of California, *Geology*, *29*(5), 459.

Osmundsen, P. T., and J. Ebbing (2008), Styles of extension offshore mid-Norway and implications for mechanisms of crustal thinning at passive margins, *Tectonics, 27*(6), TC6016.

Panter, K. S., and P. Castillo (2007), Petrogenesis and source of lavas from seamounts in the Adare Basin, Western Ross Sea: Implications for the origin of Cenozoic magmatism in Antarcitca, paper presented at 10th International Symposium on Antarctic Earth Sciences.

Ritzmann, O., W. Jokat, W. Czuba, A. Guterch, R. Mjelde, and Y. Nishimura (2004), A deep seismic transect from Hovgärd Ridge to northwestern Svalbard across the continental ocean transition: A sheared margin study, *Geophysical Journal International*, *157*(2), 683-702.

Sieminski, A., E. Debayle, and J.-J. Lévêque (2003), Seismic evidence for deep low-velocity anomalies in the transition zone beneath West Antarctica, *Earth and Planetary Science Letters*, *216*(4), 645-661.

Trehu, A., J. Behrendt, and J. Fritsch (1993), Generalized crustal structure of the Central basin, Ross Sea, Antarctica, *Geol. Jb*, *47*, 291-311.

Trey, H., A. K. Cooper, G. Pellis, B. della Vedova, G. Cochrane, G. Brancolini, and J. Makris (1999), Transect across the West Antarctic rift system in the Ross Sea, Antarctica, *Tectonophysics*, *301*(1-2), 61-74.

Truswell, E. M., and D. J. Drewry (1984), Distribution and provenance of recycled palynomorphs in surficial sediments of the Ross Sea, Antarctica, *Marine geology*, *59*(1-4), 187-214.

Weaver, S., B. Storey, R. Pankhurst, S. Mukasa, V. DiVenere, and J. Bradshaw (1994), Antarctica-New Zealand rifting and Marie Byrd Land lithospheric magmatism linked to ridge subduction and mantle plume activity, *Geology*, *22*(9), 811.

Whitmarsh, R. B., G. Manatschal, T. A. Minshull (2001), Evolution of magma-poor continental margins from rifting to seafloor spreading, *Nature, 413*, 150-154.